Hydrodynamics of polarized crowds : experiments and theory

Nicolas Bain

Numéro National de Thèse : 2018LYSEN078

THÈSE de DOCTORAT DE L'UNIVERSITÉ DE LYON
opérée par
l'École Normale Supérieure de Lyon

École Doctorale N°52
École Doctorale de Physique et Astrophysique de Lyon (PHAST)

Spécialité de doctorat : Physique

Soutenue publiquement le 16/11/2018, par :

Nicolas Bain

Hydrodynamics of polarized crowds : experiments and theory

Étude hydrodynamique des foules polarisées : expériences et théorie

---

Devant la commission d'examen composée de :

Barrat, Jean-Louis	Professeur	LIPHY	Examinateur
Bartolo, Denis	Professeur	ENS de Lyon	Directeur de thèse
Biance, Anne-Laure	Chargée de recherche au CNRS	ILM	Examinatrice
Démery, Vincent	Maître de conférences	ESPCI	Rapporteur
Giardina, Irene	Professeure	Sapienza University	Rapporteure
Théraulaz, Guy	Directeur de recherche au CNRS	CRCA	Examinateur

Acknowledgements

What a journey. This PhD started as an exploratory project to capture the large-scale motion of human crowds wherever it was possible. During the first year, this guideline brought me from the concert hall across the street to the City Hall across the river, and from the City Hall across the river to a hotel hall across the Atlantic ocean. There, I obtained the images of the 2016 Bank of America Chicago Marathon which kept me busy for the rest of my PhD. Throughout this mission, I benefitted from the help of several people and without them none of this would have been possible. T. Theodory, M. Kinzig and C. Garcia from the Halle Tony Garnier across the street. E. Magne and T. Courtot from the Marie de Lyon across the river as well as C. Bertinatti from Amaury Sport Organisation. And D. Reithoffer from the Seagull Institute across the ocean. I would like to thank you all for helping me film numerous crowds.

At home, I would like to thank my advisor Denis Bartolo. Thank you for your time, your patience, and your trust. Thank you for supporting me when necessary and pushing me when needed. Thank you for the more than valuable scientific discussions and the less than endless keynote corrections. I chose to work in your group not only for the project itself, but also because I wanted to have an incredible advisor. And you proved me right, thank you also for that.

More generally, thank you to all the members of the so-called Bartolo team. Alex, my co-PhD for three years. It feels like we grew up together. Joost, my coding father and outstanding office mate. I'm sure you would do great in a paper company. Thank you also to the dinosaurs Céleste, and David, and to the rising stars Delphine, Marine, Lucile, Amélie and Marcello! I would like to also thank the rest of the Laboratoire de Physique, and especially Thierry for managing to keep it such an enjoyable place to work, and Nadine and Laurence for helping me book the expensive hotels my cameras needed!

I also want to thank all the friends who surrounded me during this time in Lyon. The climbing gang Claire, Colin, Laurent and Pascale. It was so nice to keep the Boston spirit going with you all. Chloé, Christophe and Gabriel who were the first friends I met here in Lyon, followed by Baptiste the super-runner and Jérémy the super-climber. And of course thank you to the old-time crew Antoine, Aubert, Bertrand, Romain and all the others. Your deep and long-lasting frienships mean a lot to me.

A special thank you goes to my family, especially my parents for their continuous support. But also to my brothers Jérémy and Mathieu, to my Mamie for having me explain what I was doing every Christmas, my uncle and aunt Philippe and Christine for helping me change my winter tires, and to all my cousins in France and in the US for the laughs and the good times.

Last but not least, I would like to say the deepest thank you to Coralie for sharing my life this past year.

Table of contents

Introduction

After losing a fortune by misinvesting in the 1720 South Sea Bubble, Isaac Newton wrote the following words: "I can calculate the motion of heavenly bodies, but not the madness of people" [69, 88]. Three hundred years later, we have sent robots to Mars and detected gravitational waves but predicting human collective behavior is still an arduous task. The complex interactions between individuals can lead to unforeseen collective outcomes, not only in financial markets but also in the physical motion of human crowds, which modelling is essential for communities as diverse as risk management, event planning, or even the motion picture industry. For the past two decades, mathematicians, ethologists and physicists have come to grips with this issue, trying to construct predictive models of crowd dynamics. The main challenge in understanding the dynamics of human crowds lies in the difficulty to obtain quality experimental data. In this Chapter, we give a broad and unavoidably biaised overview of four major lines of research in the domain of pedestrian dynamics. Two of them are experimental approaches. They consist in measuring pedestrian motion, either in a natural or in a controlled environment. The two others are theoretical. They consist in modelling pedestrian behavior, either at the individual or at the collective level. For each of these four research axis we will illustrate key results by discussing the corresponding articles. We summarize the key results at the beginning of each section.

1 Field measurements

An intuitive way to acquire experimental crowd dynamics data is to film pedestrians in their natural environment. Such field measurements can be conducted in a street, a train station, a concert hall, or any location where one can set a camera.

1.1 Low density measurements, non-local interactions

Summary of this section: The experimental observations of Karamouzas et al. [51] show that pedestrian binary interactions in dilute environments are non local. More precisely, instead of being short ranged they depend on a complex combinaison of relative distance and velocity: the anticipated time to collision.

At low densities, where individual tracking is possible, the trajectories of the pedestrians can provide insight into their walking dynamics [53] and pair interactions [51]. For instance, Karamouzas et al. [51] conducted a quantitative anaylsis on six datasets, from four different papers. Four datasets

correspond to individuals interacting in the street (Fig. 1a) and two to model experiments of pedestrians going through a bottleneck (model experiments will be detailed later on in this Chapter). They analysed the pair correlation function $g(r)$ in each dataset and noted that the structural correlations vary with the relative approach speed between individuals (Fig. 1b). In other words, the interactions between individuals do not depend on the relative distance r only but also on relative velocity. This is not surprising: two individuals walking side by side have no reason to avoid each other, and two individuals walking towards each other should change their trajectory in anticipation to avoid colliding (Fig. 1a). In contrast, they found that the probability to find two individuals about to collide in a time τ, $g(\tau)$, was independent of the relative approach speed (Fig. 1b). Consequently, they assumed that the interaction rules between individuals were only functions of the anticipatory time to collision τ, which is a nonlinear combinaison of relative distance and velocity.

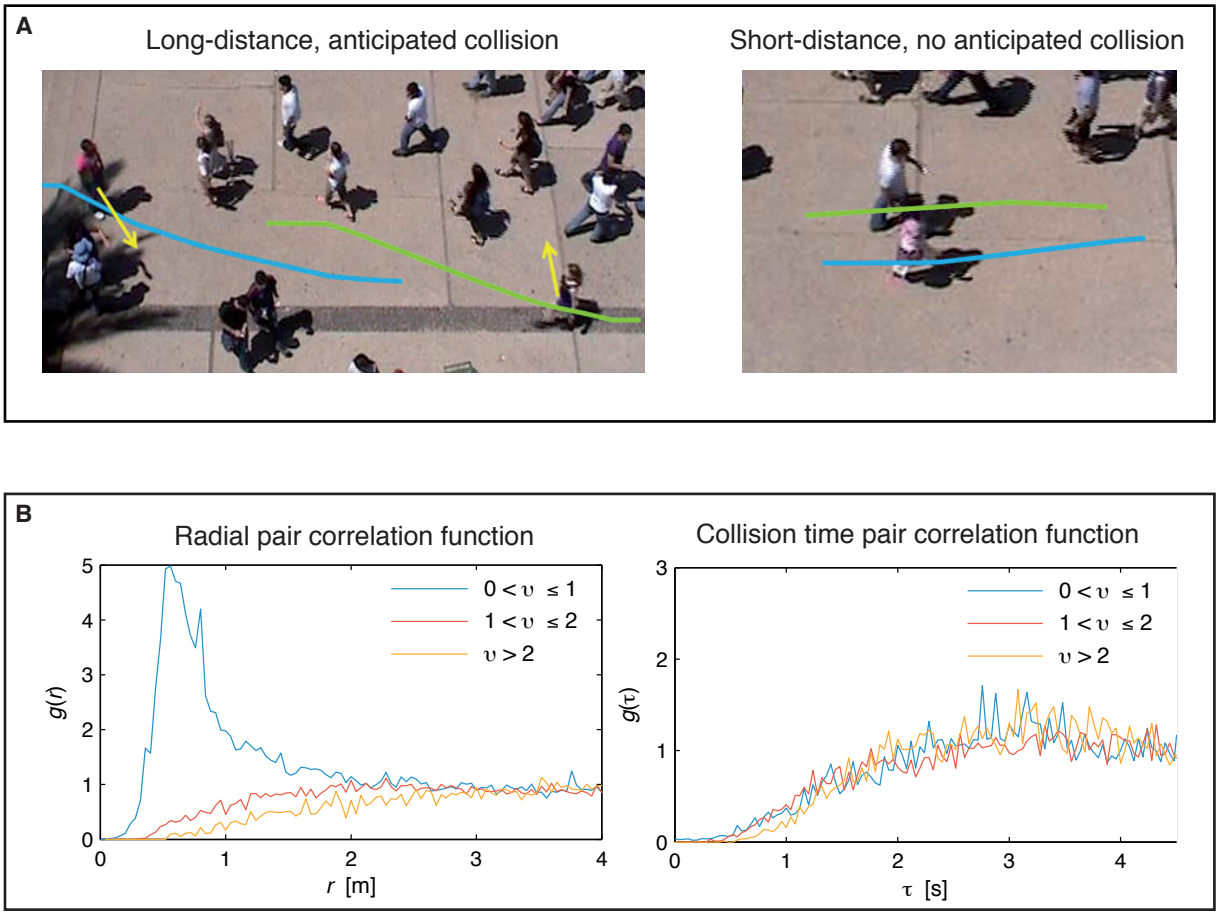

Figure 1 | Interactions among pedestrians are non-local (all adapted from [51]). (A) Image from a field measurement at low density. Pedestrians that are projecting a collision change their trajectory in advance (left), but pedestrians that walk side by side don't (right). (B) Pair correlation function (left) and probability do find two pedestrians about to collide in a time τ (right) at different approach speeds.

1.2 High density measurements, a rich phenomenology

Summary of this section: The qualitative observations made by Helbing et al. [43] shed a unique light on large-scale pedestrian behavior in extreme events. They show a rich panel of dynamics, from laminar flow to instability propagation under the form of velocity waves and irregular movements bursts implying all length scales. They are, however, unlikely to be repeated: extreme events are rare and unpredictable, and often occur in complex geometrical settings. Without a previous understanding of human flows it is then delicate to infer generic laws from these observations.

High density field measurements are ideal candidates to obtain large statistics on human collective motion. As they are difficult to implement, though, such measurements are scarce. One way to bypass the technical difficulties of filming large human gatherings is to use the immense video resources now offered by social media, Youtube or Instagram, e.g., of concert audiences, readily available publicly [83, 6]. Although promising, this approach is for now limited by the low quality of the available resources, which makes their quantative exploitation delicate.

The most influential analysis of large human crowds comes from video recordings of the crowd disaster that took place in Mina/Makkah during the 2006 Hajj [43]. During this event, thousands of pilgrims went through the 44-meter-wide entrance to the Jamarat bridge (Fig. 2a). Helbing et al. analyzed a video recording of a $12 \times 20\,\mathrm{m}^2$ area in front of this entrance, and after successive image processing procedures obtained individual positions and velocities of the visible pilgims. From these measurements, they computed the velocity and density fields as a function of time and evidenced a rich phenomenology. Helbing et al. found that the relation between local density and velocity, usually called the "fundamental relation", did not fall on previous measurements made in the street [61, 75, 30] or in controlled experiments [82] (Fig. 2b). They showed that the density could be arbitrarily rescaled to make the fundamental relations from these different experiments agree (Fig. 2b inset), but noted that in contrast with theoretical predictions [99] the local velocity did not go to zero at a given density (Fig. 2b). Instead, velocity reaches a plateau at extreme density values, higher than 9 people per square meter. Helbing et al. suggested that such high density flow was associated to some complex crowd behavior.

In fact, as density increased on their footage, they evidenced three distinct behaviors. At lower densities, the pilgrims were going on the bridge smoothly, displaying a laminar flow. As density increased, the flow became intermittent and nonlinear excitations nucleate and propagate backwards in the crowd (Fig. 2c). Eventually this transitionned to an irregular flow pattern, in which the pilgrims were being physically pushed around in any direction in a turbulent-like pattern (Fig. 2a). More quantitatively, they showed that within this phase the displacement amplitude distribution decay as a power law, implying that all length scales were involved in this dynamics (Fig. 2d).

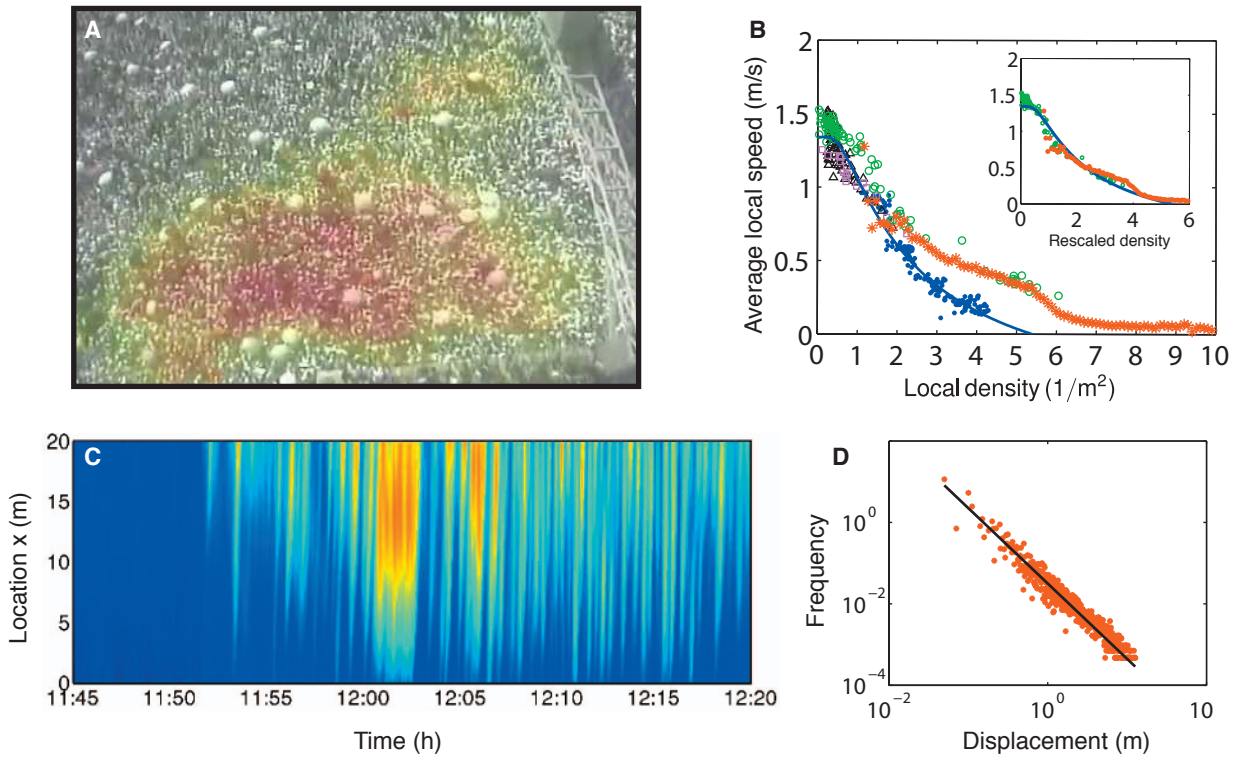

Figure 2 | Experimental data of the 2006 Hajj (all adapted from [43]). (A) Image from the video footage of the entrance of the Jamarat bridge, during the occurence of the so-called crowd turbulence. Color codes for displacement intensity (B) Fundamental relation: local speed as a function of the local density. Red stars are from the Hajj measurements [43], black triangles [30], green circles [61] and purple squares [75] from street measurements and blue dots from a controlled experiment [82]. Solid blue line is a theoretical fit [99]. Inset: scaling the density by a factor of 0.7 for [43] and a factor of 0.6 for [61], the rescaled fundamental relations are compatible with the theoretical fit [99]. Same color codes. (C) Kymograph of the local density. After 11:50, density oscillations start to appear and propagate in the crowd. (D) Distribution of displacements in the "turbulent" phase.

2 Controlled laboratory experiments

To avoid the complexity of natural environments, a remedy is to conduct controlled laboratory experiments. In these experiments, up to a hundred of participants are placed in a well-defined setup, e.g., a gymnasium with moveable cardboard walls, and instructed what-to-do. Instructions can be on where to go and how to go there, and techniques are available to enable accurate individual tracking. As they are highly adjustable and provide quality trajectories, controlled laboratory experiments are very well suited to investigate specific pedestrian behaviors. We will here present experimental results of pedestrian behavior in three different controlled environments: when they are instructed to move as a group, when they are placed in a unidimensional configuration and when they attempt to exit a room through a narrowing.

2.1 Group-following behavior

Summary of this section: Rio et al. [78] showed that when following a group, pedestrians adjusted their orientation and speed to match the one of their visible neighbors, akin to flocking systems in which local orientational alignement of every agent with the average orientation of its neighbors makes the group spontaneously go in a unique direction [95].

An innovative way to control the environment around a pedestrian is to construct it numerically. Participants can then be projected in this environment with a virtual reality setup. Recently, Rio et al. [78] used such a technique to obtain quantitative data on human interactions when they move as a group. They immersed a participant in two circles of virtual pedestrians walking in the same direction, and gave him or her the instruction to stay within the group (Fig. 3a). They could then change the speed and orientation of a subset of virtual pedestrians at will and investigate the response of the human participant. More specifically, in each experiment Rio et al. used a unique perturbation, either in speed or in orientation, and varied which virtual pedestrians were subject to it. They repeated this type of experiment with several participants, and evidenced three main features of the participants following behavior. Firstly, they showed that the participants adjusted their orientation and speed proportionally with the number of perturbed pedestrians, implying additivity of interactions (Fig. 3b). Secondly, they found that the participants responded stronger to closer perturbed pedestrians, suggesting that the interaction strength decayed with distance. It is unclear, however, if this dependence comes from the distance between pedestrians or from the obstruction from the closer pedestrians. At last, they demonstrated that as long as the perturbed pedestrians were in the visual field of the participant, their angular location with respect to the participant had no significant influence on his or her response. To confirm these results, Rio et al. then conducted an additional controlled experiment, without virtual reality. They instructed two groups of 16 and 20 participants to walk together for a few minutes, and measured the individual trajectories. They found that the spatial distribution of absolute orientation difference between the central participant and the other participants isotropically increased with distance (Fig. 3c), qualitatively supporting two of the conclusions reached by the virtual reality setup: the decay of the interaction strength with distance and the lack of angular dependence.

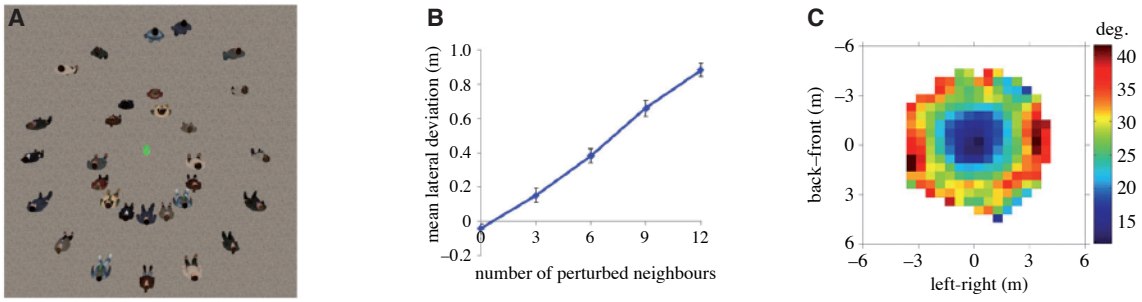

Figure 3 | Swarming experimental results (all adapted from [78]). (A) Participants (green dot) are immersed in two circles of virtual pedestrians. (B) The mean lateral deviation of participants increases linearly with the number of perturbed neighbors. (C) Spatial distribution of the mean absolute orientation difference between the central participant and the other participants in the human swarm.

2.2 Unidimensional flow

Summary of this section: The controlled unidimensional setup used by Jelic et al. [50] and Lemercier et al. [56] evidenced a robust velocity-density relation, and the appearance of spontaneous velocity waves within a given density range.

A simple way to investigate unidirectional human flows, often encountered in everyday life, in a systematic and repeatable manner is to create a unidimensional setup [50, 56, 82]. More specifically, pedestrians are usually placed in a single lane on a ring, to create periodic boundary condtions. Such setups have been used to characterize two main phenomena: the relation between velocity and density, and the appearance of spontaneous density-velocity waves. We here present two papers based on the same experimental data: Jelic et al. [50], which focuses on the velocity-density relation, and Lemercier et al. [56], which focuses on the spontaneous emergence of density-velocity waves. The joint experimental setup is the following: 28 participants are instructed to follow each other without overpassing in a circular setup (Fig. 4a). To vary the overall density, the researchers changed the number of participants or made them walk either on the inner or outer boundary of the setup (Fig. 4a). They used an optoelectronic capture motion system to obtain accurate trajectories of each individual.

Jelic et al.[50] investigated in details the relation between velocity and density, commonly referred to as the "fundamental diagram". Qualitatively, velocity decreases with increasing density: the more people on the ring the slower they walk. To characterize the so-called fundamental relation more precisely, Jelic et al. differentiated three ways to evaluate both density and velocity. First, density and velocity can be averaged over space and time, giving a macroscopic fundamental diagram. Second, they can be evaluated locally on a small portion of the circle, as done in previous work by Seyfried et al. [82]. At last, density and velocity can be estimated instantaneoulsy, at every time step, for every individual. Jelic et al. showed that the velocity-density relations obtained with these three measurements methods were alike, and consistent with the one obtained by Seyfried et al. [82] (Fig. 4b). They noted that instantaneuous measurements probe a wider range of density values, and found that even at relatively high densities the velocity does not go to zero, in agreement with the global velocity-density relation obtained by Helbing et al. [43] at the 2006 Hajj (Fig. 2b). Jelic et al. investigated the velocity-density relation in greater details by looking at the inverse of the density: the distance between successive pedestrians. They showed that the instantaneous distance between successive pedestrians varied piecewise linearly with the instantaneous velocity. More precisely, they identified three regimes: at low density, the individual velocity v was found to be insensitive to variations in the distance between pedestrians dx. At intermediate and high densities, the velocity changed linearly with inter-participant distance following two distinct slopes, corresponding to two different adaptation times (Fig. 4c). Jelic et al. then compared these results, obtained from French participants, with the ones of German and Indian participants walking on a circle [17]. They found no discrepancy between the three samples: all showed a linear relation between velocity and inter-participant distances at high densities, with similar adaptation times. They concluded that this behavior should be a universal feature of single pedestrian lanes.

Lemercier et al. [56] analysed the same experimental data as Jelic et al.[50], but focused on the fluctuations around the mean state. In a certain global density range, between 1 and 1.6 participant per meter, they observed strong fluctuations in density and velocity which translated into backwards propagating density-velocity waves (Fig. 4d). Such waves spontaneously appeared and vanished in an

unpredictable way, but consistently propagated backwards at a velocity of about 0.6 meters per second. To characterize the way these waves disappeared, they defined a damping parameter from their typical life time and found it to be of the order of 0.01 $\mathrm{m.s}^{-2}$. We do not know, however, if these waves have the same properties as the ones qualitatively observed at the 2006 Hajj [43]. In Chapter 2 we evidence and quantitatively characterize another type of waves: we observe velocity excitations that faithfully propagate at a velocity of the order of $1\,\mathrm{m.s}^{-1}$ over hundreds of meters.

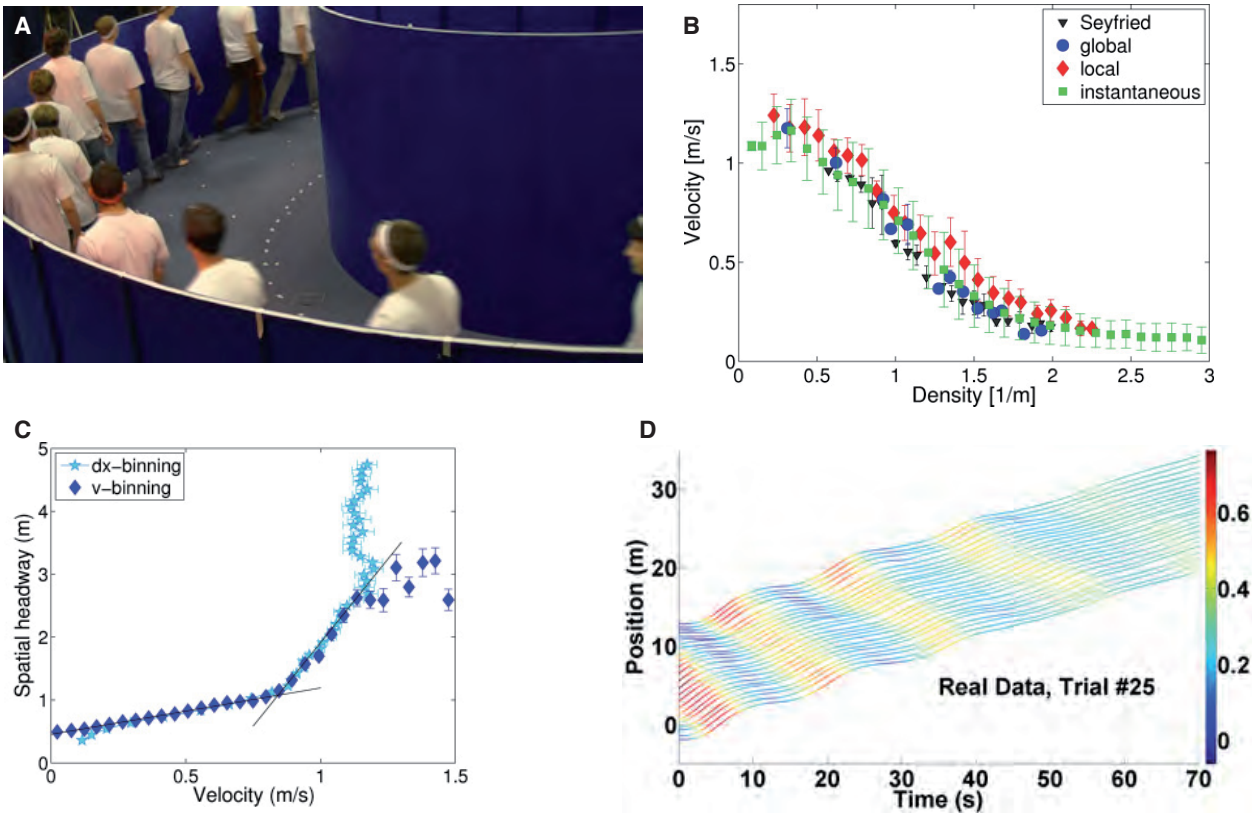

Figure 4 | Experimental results from unidimensional flows in a controlled setup . (A) Picture of the experimental setup. Participants are placed in a circular setup and instructed to follow one another without overtaking (adapted from [56]). (B) Fundamental relation between velocity and density. Blue dots are gobal measurements, red diamonds averaged over a segment of the setup and green squares are instantaneous measures. Black triangles are from averages over a segment of another setup [82] (adapted from [50]). (C) Instantaneous inter-pedestrian distance ($dx = 1/\rho$) as a function of velocity v. Light blue stars are for a binning over the distance and dark blue diamonds a binning over the velocity. (adapted from [50]). (D) Positions of pedestrians on the ring as a function of time as a velocity wave propagates and is damped. Color codes for the instantaneous velocity (adapted from [56]).

2.3 Flow at constrictions

Summary of this section: flows at constrictions exhibit the same global phenomenology for pedestrians, sheeps and grains. Instead of speeding the flow up, increasing the eagerness to exit creates longer lasting clogs, which eventually slows the exiting process down. Interestingly, such a similarity is not unique to flows at constrictions. As we mention later on in Chapter 1, bidirectional flows of pedestrians [55] army ants [20], complex plasmas [87] and colloidal mixtures [57] have all been evidenced to consistently form lanes.

Akin to unidirectional scenarii, flows at constrictions come about constantly. Whenever a class, a subway ride, or a concert is over, participants at some point have to go through a narrowing to exit the location. There, the flow slows down, leading to a density increase and sometimes to clogging. Some parameters, such as the door width or the eagerness of pedestrians to exit, are specific to each situation and affect the exiting dynamics. Controlled laboratory experiments are then ideal candidates to isolate the different variables and investigate their influence on pedestrian flow. Using such experiments, Pastor et al. [71] focused on the so-called "faster is slower" effect. This phenomena, which had been predicted numerically [41] but not characterized experimentally, states that the faster the pedestrians want to exit, the slower the flow. Pastor et al. conducted experiments with groups of 95 participants, who were instructed to exit a room through a 69 cm wide door (Fig. 5a). To change the desired exiting speed of the participants, they gave three sets of instructions. Pastor et al. asked the participants to exit the room as fast as possible while, in increasing level of competitivity, (i) avoiding touching anyone else, (ii) allowing soft contacts with other participants and (iii) gently pushing their way through. They observed that, in this specific order, the different instructions resulted in an increase in the initial speed to reach the door, an increase in the density in front of the door and an increase in the physical pressure exerted on the door frame (Figs. 5a and 5b). In other words, the directives were effective in affecting the motivation of the participants to exit. They quantified the exiting dynamics by measuring the time-lapse between consecutive exits, τ. Pastor et al. confirmed the existence of the faster is slower effect by showing that the average time between two exits $\langle\tau\rangle$ increased with the eagerness to exit, implying a slowdown of the flow with increased motivation to exit (Fig. 5c). More quantitatively, they computed the cumulative probability density function of the time-lapse τ, $p(t \geq \tau)$, and found that it displayed power-law tails $p(t \geq \tau) \propto \tau^{-\alpha}$ with a decay exponent α that decreased with increasing competitivity (Fig. 5d). To put it differently the time-lapse between exits are distributed over all scales, and when pedestrians try to exit faster the probability of large time-lapses, i.e. clogging, increases. These results confirm the numerical hypothesis that when pedestrians want to exit faster, they might slow the flow down by creating jams in front of the exit. Pastor et al. then conducted similar experiments on sheeps and changed the animals activity by carrying experiments on hot and cold days. They also found an increase of the average time-lapse $\langle\tau\rangle$ with the activity (Fig. 5c) and a power-law decay of the time-lapse cumulative probability density function (Fig. 5d), implying that this phenomenology is not specific to human behavior.

These experiments, however, are limited in size and repeatability. To investigate the "faster is slower" effect in greater details, Pastor et al. studied an equivalent setup with glass beads. They placed 500 beads on an inclined vibrating plate, made them flow through a constriction, and computed the time-lapse between two exiting beads at different plate inclinaisons. Since the inclinaison changes the effective gravity acting on the beads, it is used as the equivalent of the eagerness to exit. They showed

that a stronger incline increased the flow in between clogs but also increased clogs' lifespan, thereby decreasing the overall flow (Figs. 5c and 5d). This suggests that the "faster is slower" effect comes from the formation of clogs that last longer with increasing activity, and that this phenomenon is universal to any granular system of frictional particles that are driven out of equilibrium through a constriction.

2.4 Discussion

From an engineering point of view, controlled laboratory experiments, whether they reproduced a constriction situation or investigated the specifics of a unidirectional lane of pedestrians, provided useful insight into pedestrians dynamics. The concept of fundamental relation is frequently used to design urban facilites, and the analogy between grain and pedestrian flows at constrictions gave birth to a design solution used to fluidify exiting flow. In both pedestrian and grain flows, it has been shown that placing an obstacle in front of the exit can reduce the formation of clogs and thereby fluidify the flow [105, 39].

From a fundamental perspective, however, the current state of experimental knowledge is not sufficient to infer the local symetries of pedestrian interactions. In the aforementioned experiments, pedestrian behavior seems to be highly context-dependent. When following a group, individuals seem to behave like a flocking system, but when exiting a room they display a phenomenology similar to grains. In addition, as noted by Jelic et al. [50], the shape of the fundamental diagram strongly depends on the geometry of the experimental setup (see Fig. 1b), implying that the results obtained for single lanes do not necessarily extend to other configurations. Similarly, the propagation speed, damping rate, and even the nature of the waves obtained from the controlled experiment of Lemercier et al. [56] might not be the same as the stop and go waves observed in the field measurement of Helbing et al. [43]. A reason for this drawback is that controlled laboratory experiments are necessary small scale. Akin to any physical system with a small number of particles, they are therefore sensitive to boundary conditions.

3 Microscopic models

A second strategy to elucidate pedestrian behavior in controlled environments is to use numerical simulations. The striking resemblance between human and grain flows inspired physicists to construct numerous microscopic models of pedestrian dynamics. After all, human crowds are essentially composed of interacting individuals, so understanding the local interaction rules should provide sufficient information to fully describe global dynamics. This idea has been intensively exploited by the scientific community, and the current litterature is now populated with a large diversity of microscopic models [23, 80, 26]. We will not provide an exhaustive description of all existing models, but instead present two different ones, one from the physics community and one from the social sciences community, with the aim to render the current diversity of pedestrian models.

3.1 Social-force model

Summary of this section: the social-force model, inspired by the modelization of Newtonian particles, qualitatively reproduces a number of qualitative experimental observations of pedestrian behavior in controlled environments.

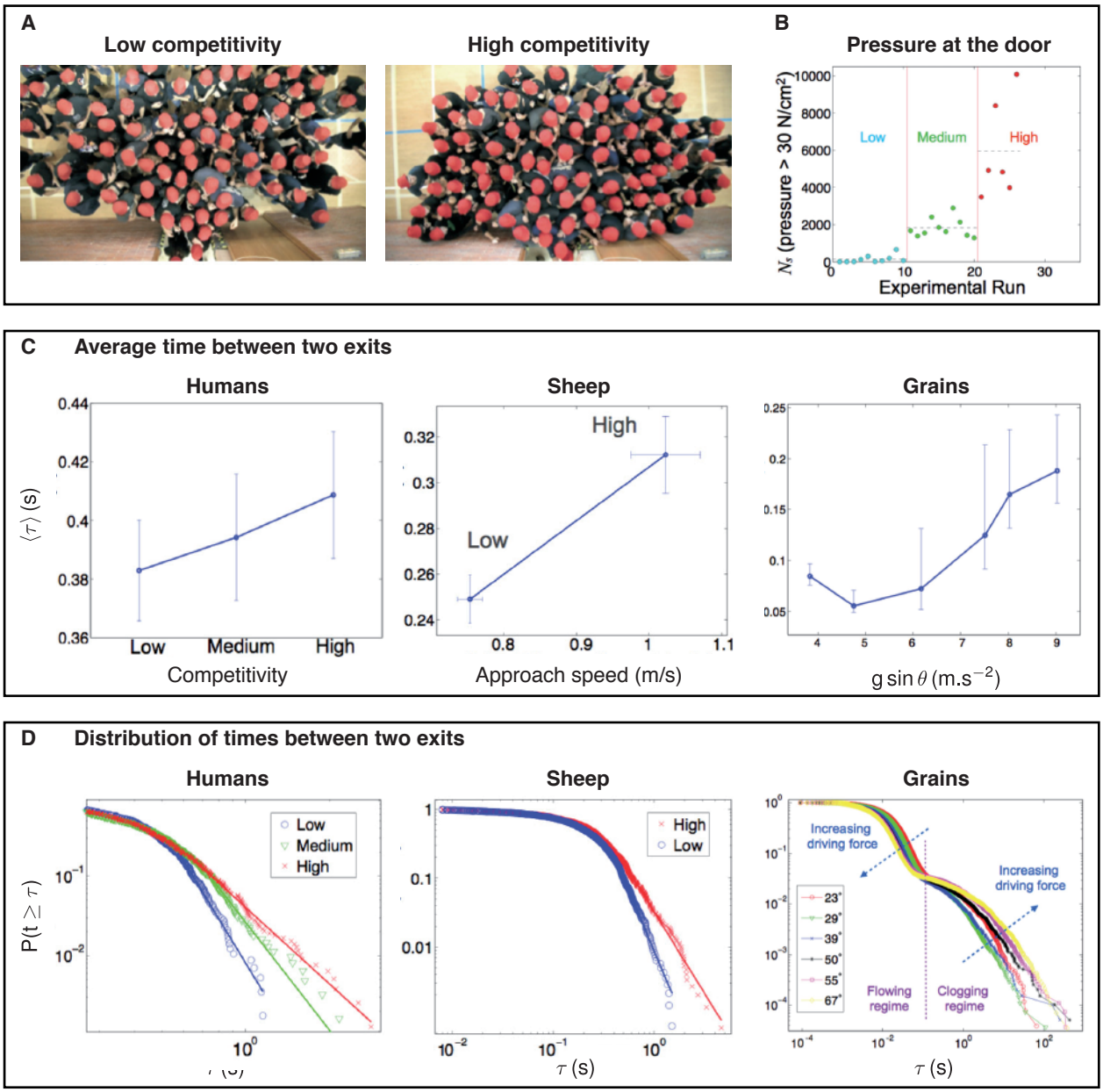

Figure 5 | Evidence of the "faster is slower" effect in systems of pedestrians, sheeps and grains (all adapted from [71]). (A) Images of the experimental setup when participants are instructed to leave with low (left) and high (right) competitivity. (B) Pressure exerted on the door frame for all the conducted experiments, orderd in level of competitivity. (C) Average time between two consecutive exits in systems of pedestrians, sheeps and grains, respectively as a function of intructed competitivity, approach speed and effective gravity. (D) Cumulative probability density function of time between two consecutive exits in systems of pedestrians, sheeps and grains. All exhibit law tails.

The first significant model, commonly referred to as the social force model, was developped by Helbing et al. [45] on the basis of a universal principle: momentum conservation. Like any other physical object, the rate of momentum change of a pedestrian results from a force balance. The two main forces acting on each pedestrian are the frictional contact with the ground and occasionally physical encounters with external bodies. The equation of motion for the position $\mathbf{r}_i$ of an individual of mass m_i then takes a simple form:

$$m_i \ddot{\mathbf{r}}_i = \boldsymbol{\mathcal{F}}_i + \sum_{j \neq i} \mathbf{f}_{ij}^{p}, \tag{1}$$

where $\boldsymbol{\mathcal{F}}_i$ is the friction with the ground and $\mathbf{f}_{ij}^{p}$ the physical interactions with the walls or other pedestrians. In dilute environments, where pedestrians move freely, the friction with the ground $\boldsymbol{\mathcal{F}}_i$ encapsulates all the complex cognitive processes of deciding what trajectory to follow. Helbing et al. postulated that this "social" force could be separated into two parts: the will to reach a given destination, and collision avoidance. More specifically, they suggested that any pedestrian relaxes its velocity to a so-called desired velocity $\boldsymbol{\nu}_i$ in a finite time m_i/α_i, and avoid collision with obstacle j through a social force $\mathbf{f}_{ij}^{s}$ that depends on the relative distance $\mathbf{r}_{ij} = (\mathbf{r}_i - \mathbf{r}_j)$:

$$\boldsymbol{\mathcal{F}}_i = -\alpha_i \left[\dot{\mathbf{r}}_i - \boldsymbol{\nu}_i\right] + \sum_{j \neq i} \mathbf{f}_{ij}^{s}(\mathbf{r}_{ij}). \tag{2}$$

The orientation of the desired velocity $\hat{\boldsymbol{\nu}}_i$ points towards the location pedestrian i wants to reach, and the magnitude of the desired velocity ν_i translates the eagerness to reach it. By postulating plausible forms for these repulstive forces and reasonnable coefficient values, Helbing et al. showed that numerically solving the equations of motion Eqs. (1) and (2) qualitatively reproduced some hallmarks human collective motion, such as lane formation in a bidirectional flow (Fig. 6a), and clogging at constrictions (Fig. 6b) [45, 40]. In addition, this model predicted the so-called "faster is slower" effect, which was only evidenced experimentally afterwards [71]. Helbing et al. also showed that adding an orientational coupling between the individuals, through the desired velocity $\boldsymbol{\nu}_i$ lead to flocking behavior.

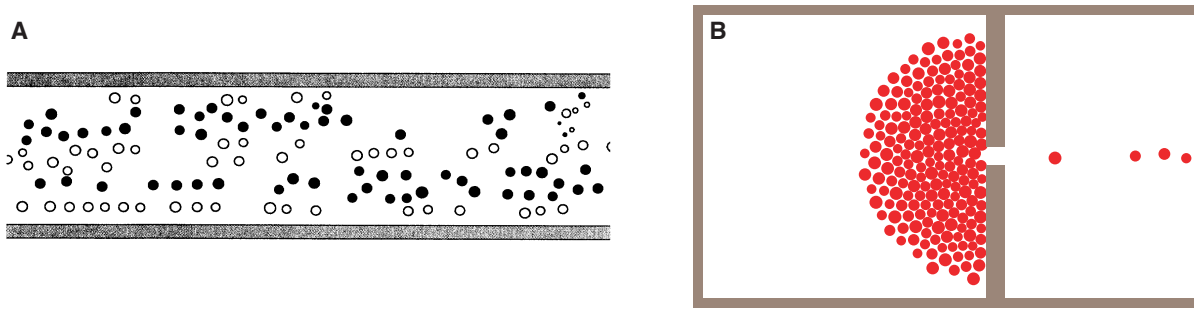

Figure 6 | The social force model qualitatively reproduces some large scale phenomena. (A) Lane formation in bidirectional flows (adapted from [45]). (B) Clogging at constrictions (adapted from [41]).

3.2 Heuristic-based model

Summary of this section: the heuristic-based model of Moussaid et al. [66] also reproduces several qualitative behavior of pedestrians in controlled environment, but shows a stronger descriptive power than the social force model. Its predictive power, however, remains difficults to assess, in particular because its computational cost prohibits quantitative comparison with large-scale phenomena.

In the social sciences community, noting that the social force model produced trajectories that resemble more grains that pedestrians [80, 51, 78], Moussaid et al. proposed a cognitive science approach. Instead of postulating the existence of social forces, which form was never successfully identified from experimental data [64, 66, 51], they constructed a minimal model based on behavioral heuristics [66]. In their model, the motion of every pedestrian is still described by a force balance, but, in contrast with the social force model, pedestrians do not adapt their motion through interaction forces. Alternatively, pedestrians only change their desired orientation $\hat{\boldsymbol{\nu}}_i$ or speed ν_i to navigate. The interaction forces $\mathbf{f}_{ij}$ and $\mathbf{f}_{iW}$ only enter into account in very dense crowds as an elastic repulsion. Additionally, Moussaid et al. assumed that the estimated time to collision with surrounding obstacles was the only information used by pedestrians to adapt their motion. In this sense, they anticipated the experimental observations of Karamouzas et al. [51]. The equations of motion for every pedestrian i then take the following form:

$$m_i \ddot{\mathbf{r}}_i(t) = -\alpha_i \left[\dot{\mathbf{r}}_i - \boldsymbol{\nu}_i(\tau)\right] + \sum_{j \neq i} \mathbf{f}^p_{ij}(\mathbf{r}_{ij}) + \sum_W \mathbf{f}^p_{iW}(\mathbf{r}_{iW}). \tag{3}$$

The orientation of the desired velocity $\hat{\boldsymbol{\nu}}_i$ is a trade-off between maximizing the potential collision time τ and minimizing the deviation from the desired destination. Given this orientation, the magnitude of the desired velocity ν_i is set as to avoid collisions. The interaction forces are purely physical and only enter into account in very dense setups. Moussaid et al. assessed the validity of their model by solving the equations of motion Eq. (3) in several different configurations. They showed that bidirectional flows reproduced the lane formation process and unidirectional flows could give rise to stop and go waves and "turbulence" [*sic*], two phenomena that were qualitatively described experimentally [43].

In addition to these qualitative verifications, Moussaid et al. conducted thorough comparisons with quantitative experimental data. At the individual level, they showed that trajectories of obstacle avoidance obtained from their model were close to recent experimental trajectories (Fig. 7a). At a larger scale, they demonstrated that unidirectional flow could give a velocity-density relationship compatible with some experimental data (Fig. 7b). Moussaid et al. also investigated very dense setups at constrictions. In this scenario the system is clogged and movements occur by bursts, in agreement with some field observations [43]. More quantitatively, their model gave the same algebraic relation between bursts frequency and amplitude as the field data in the 2006 Hajj (Figs. 2d and 7c).

3.3 Discussion

The two models described above are in essence profoundly different. Except when an orientational coupling is added, the social force model describes pedestrians as passive particles, driven to a destination by an external force: the so-called desired velocity. In the heuristic model, the direction of this desired velocity is an independant degree of freedom, making pedestrians active particles. In the social force model, avoidance interactions only depend on inter-pedestrian distance. In the heuristic

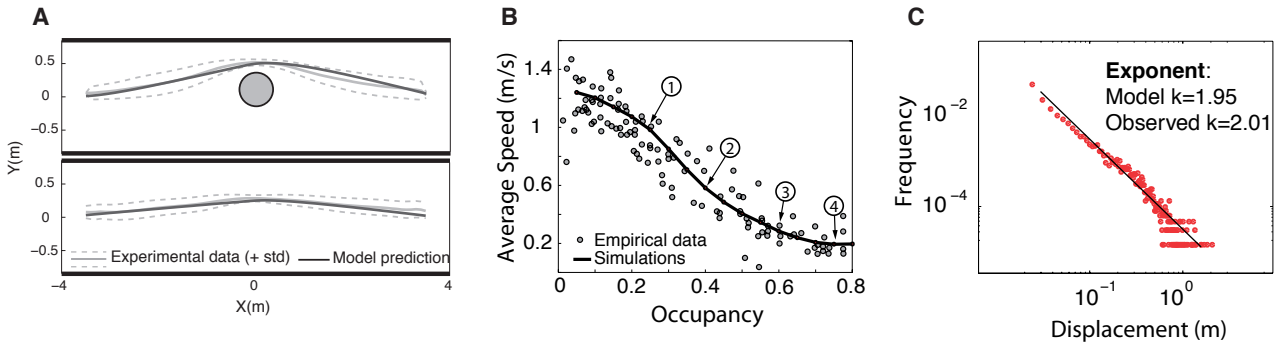

Figure 7 | Quantitative comparisons between the heuristic model and experiments (all adapted from [66]). (A) Trajectory comparison of obstacle (top) and pedestrian (bottom) avoidance in a narrow corridor. Light grey: experiments (from [64]). Dark grey: model. (B) Speed-density comparison between numerical simulations of 6 to 96 pedestrians in a unidirectional corridor and field measurements (from [70]). (C) Frequency-amplitude of displacement bursts comparison between numerical simulations of 360 pedestrians at a bottleneck and field measurements (from [43]).

model, they are non-local and function of a non linear combinaison of relative distance and velocity through an anticipation collision time. In the social force model, repulsive interactions add-up, while the heuristic model is constructed to avoid this feature. Despite these differences, both models effectively render hallmark pedestrian behavior, such as clogging at constrictions and lane formation in bidirectional flows. In dense constrictions, the heuristic-based model quantitatively reproduced the power law decay of displacements probability experimentally observed by Helbing et al. [43]. But at such densities, elastic repulsions are the dominant interactions in this model and it is impossible to know if this power-law is specific to the heuristic-based model and human systems or if it is a universal feature of out-of-equilibrium clogged particle systems. These hallmark phenomena therefore cannot be used to discriminate between different microscopic models. They all have numerous adjustable parameters, and we do not know which ones are important to correctly reproduce the observed collective phenomena. We show in Chapter 1 that bidirectional active and passive systems both form lanes, but that activity gives rise to a critical phase transition between a fully-laned state and a mixed state, absent in passive systems. Such a difference would, however, be difficult to observe experimentally: avoiding finite-size effects would require observing bidirectional human flows on very large scales.

4 Macroscopic models

As several microscopic models with different local symetries are capable to reproduce the hallmark experimental observations of crowd dynamics, it is for now impossible to definitely identify any microscopic model as *the* model of pedestrian behavior, provided that such a model exists. A way to circumvent this issue is to construct macroscopic models, only valid at long-time and large-length scales. Such models can only be meaningfully confronted to large-scale experimental data, for now scarcely avaible, but should be an effective way to describe human flows involving many individuals without having to identify the details of the local interactions.

4.1 Kinetic model

One direct way to obtain a macroscopic model is paradoxically to start from microscopic interactions. A few papers have used such an approach for pedestrian systems [24, 5]. We will here present a Boltzman-type approach, as conducted in Bellomo et al. [5] (and in Chapter 1). We derive a set of macroscopic equations from a description in terms of probability densities. We define $\psi(t, \mathbf{x}, \mathbf{v})$ the probability to find a pedestrian at velocity $\mathbf{v}$ at location $\mathbf{x}$ at time t. We assume that only advection and interactions between individuals can affect this probability:

$$\partial_t \psi + \boldsymbol{\nabla} \cdot [\mathbf{v}\, \psi] = \mathcal{I}, \tag{4}$$

where $\mathcal{I}$ carries all the informations and symetries of the interactions. From this description, time evolution of quantities such as density $\rho(t, \mathbf{x}) = \int \psi(t, \mathbf{x}, \mathbf{v}) \mathrm{d}\mathbf{v}$ and momentum $\mathbf{p} = \int \mathbf{v} \psi(t, \mathbf{x}, \mathbf{v}) \mathrm{d}\mathbf{v}$ can be obtained by appropriately integrating Eq. (4). Integrating once over the velocity, we obtain the mass conservation equation

$$\partial_t \rho + \boldsymbol{\nabla} \cdot \mathbf{p} = 0, \tag{5}$$

imposing $\int \mathcal{I} \mathrm{d}\mathbf{v} = 0$. Similarly, we derive the time evolution of momentum

$$\partial_t \mathbf{p} + \boldsymbol{\nabla} \cdot \mathbf{Q} = \int (\mathbf{v}\mathcal{I})\, \mathrm{d}\mathbf{v}, \tag{6}$$

where $\mathbf{Q} = \int \mathbf{v}\mathbf{v}\, \psi(t, \mathbf{x}, \mathbf{v}) \mathrm{d}\mathbf{v}$ is a higher order moment of the velocity. With the same procedure, another equation could be obtained for the time evolution of the nematic tensor $\mathbf{Q}$ which would depend again on a higher order moment and so on, giving a hierarchy of equations. At this point, two supplementary imformations are needed to obtain a macroscopic description of the density and momentum fields. First, the generic form of the interactions has to be determined. Second, the hierarchy of equations has to be closed with an appropriate closure relation. These two parameters are going to determine the form of the macroscopic equations. To do so Bellomo et al. [5] decoupled the interaction term into local interactions $\mathcal{I}^*$ happening with an equal probability within an interaction domain $\Omega(\mathbf{x})$ and small deviations from the local interactions $(\mathcal{I} - \mathcal{I}^*)$. They assumed that local interactions made the system locally relax towards a kinetic equilibrium $\psi^e(\rho)$, with a relaxation rate that depends on the local density only $\mathcal{I}^* = -\nu(\rho)(\psi - \psi^e(\rho))$. They estimated the expression for the non-local interactions by conducting a first-order expansion around the interaction domain. At lowest order, after some lengthy calculus, they obtained a pressure term that was function of the density gradient in the momentum balance equation Eq. (6). As for the closure relation, Bellomo et al. separated the higher order term into an advection term $\rho(\mathbf{qq})$ (where $\mathbf{q} = \mathbf{p}/\rho$ is the velocity field) and a pressure tensor $\mathbf{P} = \int (\mathbf{v} - \mathbf{q})(\mathbf{v} - \mathbf{q})\, \psi \mathrm{d}\mathbf{v}$, and assumed the distribution in the pressure term was at local equilibrium $\mathbf{P} = \mathbf{P}^e(\rho)$. Eventually, they obtained a momentum balance equation of the form

$$\partial_t \mathbf{q} + (\mathbf{q} \cdot \boldsymbol{\nabla})\mathbf{q} = -\nu(\rho)\, [\mathbf{q} - \mathbf{q}^e(\rho)] - p(\rho) \boldsymbol{\nabla} \rho, \tag{7}$$

where $p(\rho)$ is the total pressure coefficient. The balance equations Eqs. (5) and (7) form a macroscopic model that couples the velocity and the density fields. It states that mass is conserved, and that the velocity relaxes towards an equilibrium velocity that is itself a function of the local density. This model is in fact equivalent to the so-called "Payne -Whitham second-order model" for car traffic [72]. It is based on the idea that drivers try to attain a given velocity which is density-dependent $\mathbf{q}^e(\rho)$: the equivalent of the fundamental diagram we mentionned previously. This model is known to give rise

to nonlinear velocity waves, called jamitons, that propagate upstream a constant speed with a specific shape [28]. Although this model was shown to be linearly stable within a given density range [42], traffic waves are usually considered as intrinsically nonlinear and we have not found any study of linear wave propagation. As a side note, we should mention that the lack of Galilean invariance in human crowds, akin again flocking systems, could allow the advection term $(\mathbf{q}\cdot\boldsymbol{\nabla})\mathbf{q}$ to be weighted with a coefficient different from unity [92].

4.2 Hydrodynamic model

Another way to obtain a macroscopic model is to derive it phenomenologically from empirical considerations, conservation laws and symetry principles. Perhaps the most widely used phenomenological model of crowd dynamics is the one constructed by Hughes [47]. Hughes based his model on three hypothesis. First, that the speed of pedestrians was a function of the local density. Second, that the orientation of the pedestrians minimized some potential. Third, that this potential was a balance between minimizing travel time and avoiding high density areas. Hughes then postulated that these three behavioral hypothesis could be included in a mass conservation equation

$$\partial_t\rho + \boldsymbol{\nabla}\cdot[\rho\mathbf{v}] = 0, \tag{8}$$

where the norm of velocity field $\mathbf{v}$, $v(\rho)$ depends on the local density only and its orientation minimizes a given potential ϕ: $\mathbf{v} = v(\rho)(-\boldsymbol{\nabla}\phi/|\boldsymbol{\nabla}\phi|)$. Hughes then suggests that the exact form of both the potential and the density-dependent velocity may vary with each situation, and he proposed a solution that is conformally mappable. This model is a bidimensional version of so-called "first-order" models in vehicular traffic, where $v(\rho)$ would be the so-called fundamental relation. Akin to these models, it is a hyperbolic conservation equation and can sustain the propagation of shock waves. In particular, this model was used to explain the process of queue formation at bottlenecks [44].

4.3 Discussion

Interestingly, the macroscopic model Eq. (8) is nothing but the hydrodynamic limit of the kinetic model derived by Bellomo et al. Eqs. (5) and (7). At long times and large lengths scales, the velocity field relaxes quickly towards the equilibrium velocity field, $\mathbf{q} = \mathbf{q}^e(\rho)$, making the density the only hydrodynamic variable. From a fundamental perspective, as discussed more carefully in Chapter 2, this is not surprising. In human crowds, only mass is a conserved quantity. In the absence of Goldstone modes and critical behavior, there should be only one hydrodynamic variable. Which approach to use, between a "first-order" or a "second-order" model, should mostly depend on the considered time and length scales. To the best of our knowledge, however, no large-scale experimental data in simple geometries exist to confront and test these macroscopic models.

5 Outline of this thesis

The initial goal of this thesis was to fill in this gap by conducting field measurements of large human crowds in a simple and predictable setting: marathon races. Implementing such experiments required some planning, during which we could conduct a numerical and theoretical project on the lane formation process in bidirectional active flows. We here present both projects in chronological order.

5.1 Part 1: Numerical study of bidirectional active flows

As a first project, we focused on the lane formation process in bidirectional flows, a hallmark phenomenon of pedestrian dynamics, and investigated it from an active-matter point of view. For that purpose, we built a minimal model of active particle populations targetting opposite directions and solved the equations of motion numerically at different density and repulsion rates. We first evidenced the existence of two distinct phases: one fully laned and one homogeneously mixed, separated by a critical phase transition, unique to active systems. We then found that the mixed phase displayed algebraic structural correlations, akin to systems of passive particles driven in opposite directions. We explained this similarity by constructing a hydrodynamic theory, through which we identified the physical mechanisms responsible for these long-range correlations and demonstrated they were a universal feature of any system of oppositely moving particles. We end this part by reproducing the paper corresponding to this work and its associated supplementary materials.

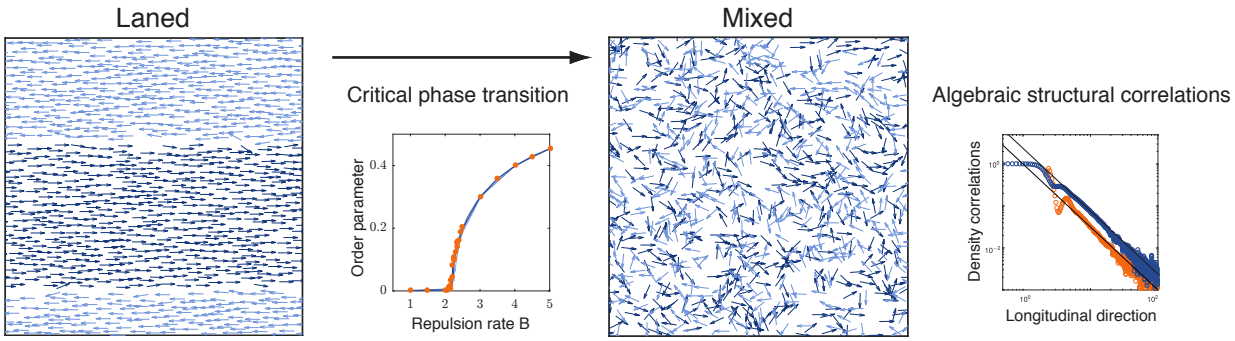

Figure 8 | Numerical simulations of active populations targetting opposite directions show two disctinct phases, a laned phase and a mixed phase, separated by a critical phase transition. The mixed phase displays algebraic structural correlations.

5.2 Part 2: Experimental study of unidirectionally polarized crowds

As a second project, we conducted numerous field measurements of a massive crowd in a unidirectional setup. More specifically, we filmed the starting corrals of major road-race events from highly-located hotel rooms, catching thousands of participants at once on every frame. We investigated the crowd response to boundary perturbations, and established how information is conveyed in large polarized crowds: speed and density information propagate freely in the direction of polarization while orientational information is overdamped over short distances. We then constructed a hydrodynamic theory of polarized crowds that is fully consistent with all our experimental observations, and found it to be valid for time scales larger than a few seconds and length scales larger than ten meters. After presenting this work, we detail the methods used in this experimental work. We then reproduce a submitted paper and add a thorough derivation of the hydrodynamic theory. Both the methods and the hydrodynamic theory sections were submitted as supplementary information of the associated paper. We here place the methods before the paper to emphasize the experimental aspect of this work.

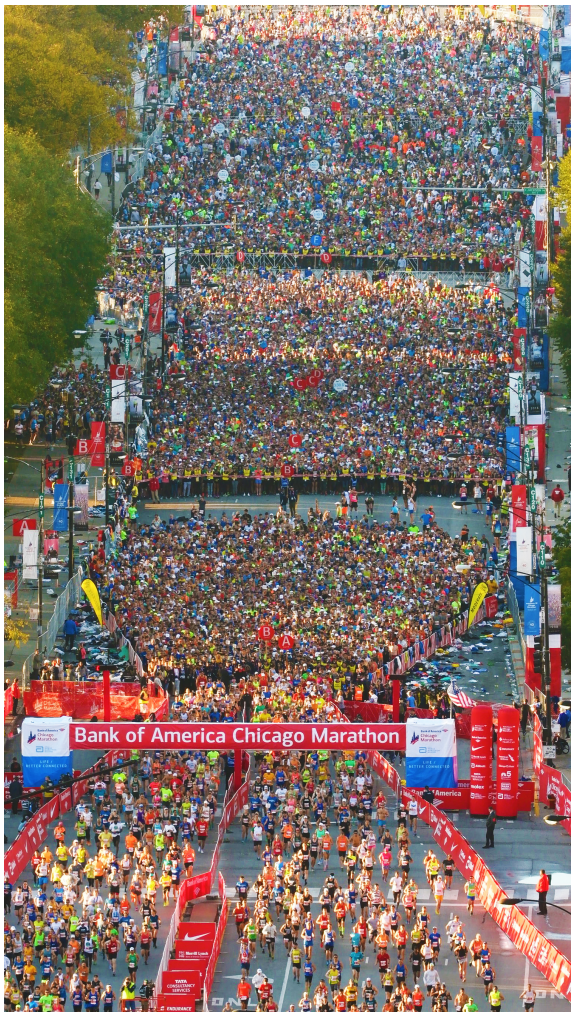

Figure 9 | Image of an experimental setup: the starting area of the 2017 Bank of America Chicago Marathon.

Part 1

Numerical study of bidirectional active flows

1 Introduction

Lane formation is among the most robust phenomena in crowd dynamics. It occurs whenever two pedestrian groups flow in opposite directions. Millions of people experience this situation on a daily basis, e.g., in crowded subway stations, and it has been reproduced and studied in controlled experiments (Fig. 1.1a) [55]. This feature, however, is not unique to human flows. Systems as diverse as army ants [20], complex plasmas [87] and colloidal mixtures [57] (Fig. 1.1b) also form lanes when forced in opposite directions. The ability of finite lanes to emerge from systems with different interaction rules and at different scales suggests that it is a universal behaviour of oppositely moving populations.

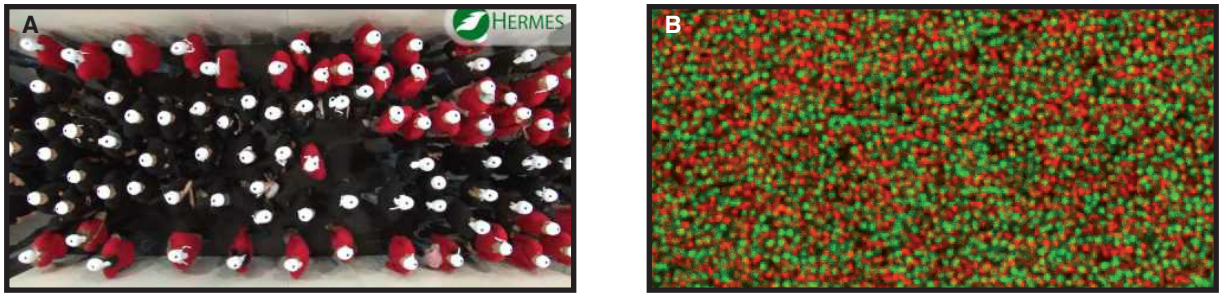

Figure 1.1 | Universality of the lane formation process. Finite lanes spontaneously emerge in systems as diverse as (A) oppositely moving human crowds (adapted from [55]) and (B) driven mixtures of oppositely charged colloids (adapted from [97]).

2 Passive systems

A natural way to investigate the lane formation process is to numerically solve the equations of motion of a model system. Most of the existing litterature is focused on the overdamped dynamics of passive particles driven in opposite directions by an external field. Within this framework, the position of every particle $\mathbf{r}_i$ evolves in time as

$$\dot{\mathbf{r}}_i = \sum_{j \neq i} \mathbf{F}_{ij} + \mathbf{F}_d + \boldsymbol{\xi}_i. \tag{1.1}$$

The first term on the right hand side of Eq. (1.1) is the repulsion force between all particles, and usually derives from a repulsive potential. The second term is the external drive $\mathbf{F}_d = \pm F_d \, \hat{\mathbf{x}}$, pointing left or right for one in every two particle. The last term is a white gaussian noise which translates random fluctuations of a particle's position, e.g., thermal fluctuations in colloidal systems.

To the best of our knowledge, two significant results emerge from the current litterature on bidirectional passive systems. First, large two-dimensional simulations evidenced that lane formation is a smooth crossover [34]. Any non-zero external forcing causes finite lanes to form, and the size of these lanes increases continuously with the intensity of the driving field (Fig. 1.2a). Second, theoretical and numerical work proved that density is infinitely correlated in the forcing direction [76]. In any dimension, at any non-zero forcing, density correlations decay algebraically in the driving direction with a dimensionally dependent coefficient, equal to 3/2 in two dimensions (Fig. 1.2b). These two key results should be generic to any system of passive particles driven in opposite directions.

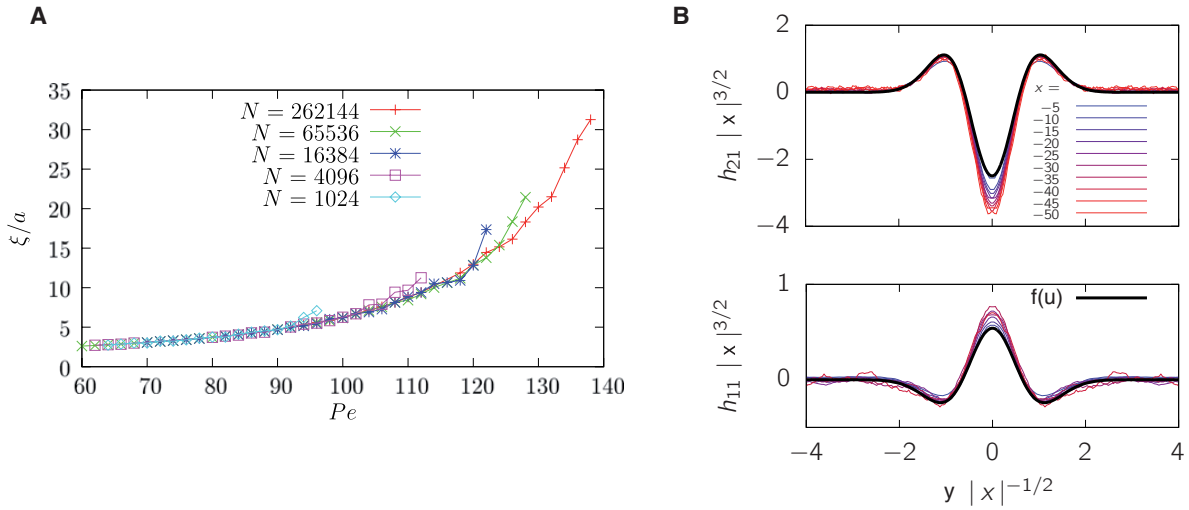

Figure 1.2 | Two key results emerge from the litterature on passive systems. (A) Lane size ξ increases continuously with the driving force (the external drive is by definition proportionnal to the Peclet number Pe). Adapted from [34]. (B) The density correlation function $g(x, y)$ decays algebraically in the forcing direction, as $x^{-3/2}$ in two dimensions. Here $h(x, y) = [g(x, y) - 1]$ is numerically shown to rescale as $x^{3/2}h(x, y) = f(yx^{-1/2})$, with $f(u)$ a generic function, proving the long-range correlation $[g(x, y) - 1] \propto x^{-3/2}$. h_{11} and h_{21} respectively denote the correlations between particles travelling in the same and in opposite directions. Adapted from [76].

3 A model bidirectionnal active system

Populations of living creatures, however, are commonly modeled as active systems: every individual has an orientational degree of freedom along which it self-propells [21, 58, 78]. This additional degree of freedom is known to give rise to new collective phenomena, such as flocking and motility-induced phase transition [91, 11]. To investigate if counterflows of active fluids have different dynamics than their passive counterparts, we constructed a simple model that isolates the orientational degree of freedom. We considered particles that self-propell at constant speed along their orientation $\hat{\mathbf{p}}_i = (\cos\theta_i, \sin\theta_i)$ without drifting

$$\dot{\mathbf{r}}_i = \hat{\mathbf{p}}_i. \tag{1.2}$$

The positional degrees of freedom are slaved to the orientations θ_i, which evolve in time as

$$\dot{\theta}_i = \sum_j B_{ij} - \partial_{\theta_i}\mathcal{V}(\theta_i). \tag{1.3}$$

The first term on the right hand side of Eq. (1.3) corresponds to repulsive torques between all particles, and is a function of both interparticle distance and orientation. The orientational dependence derives from an angular potential which is minimal when particles turn their back to each other (Fig. 1.3). The interaction rate decays with interparticle distance, and vanishes outside an interaction radius a. The second term on the right hand side of Eq. (1.3) derives from a harmonic potential $\mathcal{V}(\theta_i) = H(\theta_i - \Theta_i)^2$, with H a constant and $\Theta_i = 0$ or π for one in every two particle. The bidirectional nature of the flow is enforced by this potential, and particles naturally align their orientation either to the right or to the left (Fig. 1.3a).

We defined the time unit in the equations of motion Eqs (1.2) and (1.3) as the inverse relaxation time of the orientational confinement H^{-1}, and the length unit as the effective particle size a. Particles then self-propell at velocity $a\,H$, and the only free parameters left are the repulsion rate B and the total density.

4 Critical phase transition

Probing total surface occupations from 10% to 70% and repulsion rates in the range $B \in [1, 10]$ (in H units), we evidenced two macroscopic steady states (Fig. 1.4). First, at low densities and low repulsion rates, particles phase separate into system-spanning lanes (Figs. 1.4a and 1.4b). Second, at high densities or high repulsion rates particles form a mingled state in which each population has a net flow along its preferred direction but is homogeneously distributed in space (Figs. 1.4b and 1.4c). This phenomenology is a priori similar to the one exhibited in driven passive systems, in the sense that lanes spontaneously form in some range of the parameter space. To characterize further the lane formation process, we investigated the transition from laned to mingled states at constant density through a dynamic order parameter

$$\langle W \rangle = \langle 1 - \cos(\theta_i - \Theta_i) \rangle_i. \tag{1.4}$$

This order parameter characterizes the global alignment of both populations with their respective preferred direction, left or right. It vanishes when every particle is aligned with its preferred direction,

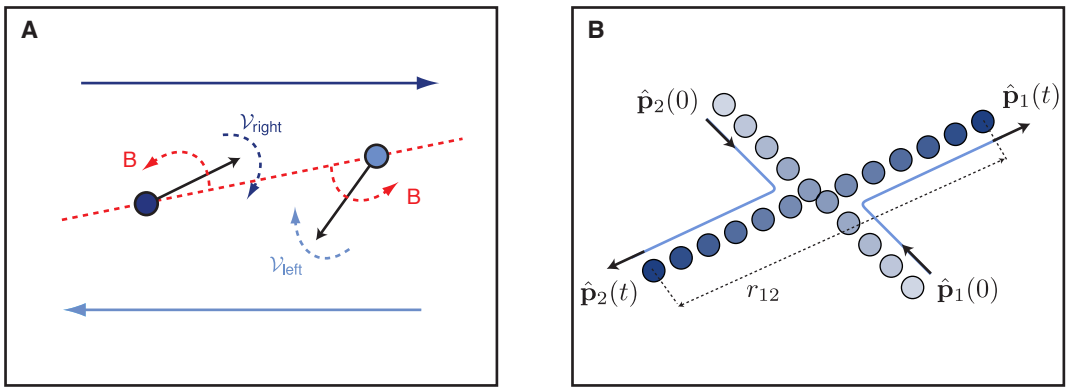

Figure 1.3 | Schematic description of the individual dynamics. (A) Illustration of the equations of motion Eqs. (1.2) and (1.3) for two particles of opposite species. Each particle travels at constant speed along its preferred direction (black arrow). Their respective orientations change via a repulsion torque B (red arrows) and the alignment on an external field $\mathcal{V}$ (blue arrows). (B) Trajectories of two particles interacting solely via a repulsive torque as defined in Eq. (1.3). The post-collision orientations $\hat{\mathbf{p}}_i(t)$ are along the center to center axis r_{ij}.

and is finite otherwise. Increasing the repulsion rate B at a constant density, we evidenced a critical second-order phase transition: the order parameter $\langle W \rangle$ goes through a bifurcation point and both the time fluctuations and the correlation time of the order parameter diverge as power laws at a critical repulsion rate B_c. Both the form of the bifurcation curve and the value of the critical repulsion rate are independent of system size, excluding finite-size effects (Fig 1.4d).

This phase transition is in stark contrast with the smooth crossover occuring in driven passive systems: below a critical repulsion rate, the two populations self-organize into system-spanning lanes. This fully laned phase has not been evidenced in passive systems, suggesting that the lane formation process is sensitive to the microscopic details of the system.

5 Universal long-range correlations

5.1 Numerical evidence of long-range correlations

The mingled phase, however, is reminiscent of the high-temperature phases of passive systems: both populations are homogeneously mixed but each displays a net flow. To examine this similarity in greater details, we numerically computed the density correlation of the mingled phase, far from the critical repulsion rate B_c. At first glance, the two-dimensional point correlation function $g(x, y)$ looks similar to a classic anisotropic fluid (Fig. 1.5a). Its longitudinal component $g(x, 0)$, however, decays algebraically with an exponent $|1 - g(x, 0)| \sim x^{-3/2}$, exaclty like passive driven systems (Fig. 1.5b).

This similarity points toward a universal property of oppositely moving populations. We elucidated this universality with a hydrodynamic description of the active binary fluid.

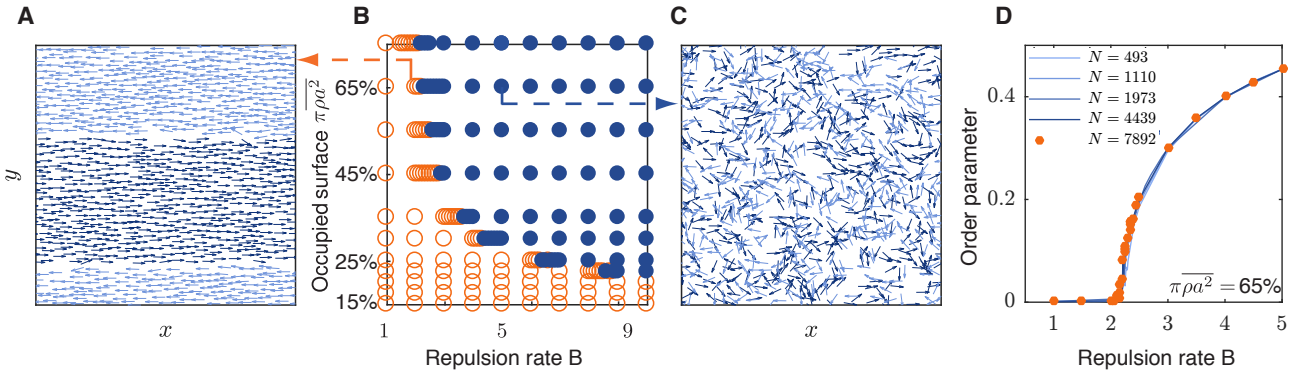

Figure 1.4 | A true phase transition. (A) and (C) Snapshots of the numerical simulations in (A) the laned phase and (C) the mingled phase. The arrows indicate the instantaneous position and orientation of the particles. Dark blue: right movers. Light blue: left movers. (B) Phase diagram. $\pi\rho a^2$ is the particle area fraction. Filled symbols: mingled phase. Open symbols: laned phase. (D) Order parameter at different repulsion rates B at a surface occupation of 65%. The bifurcation curves collapse for five system sizes.

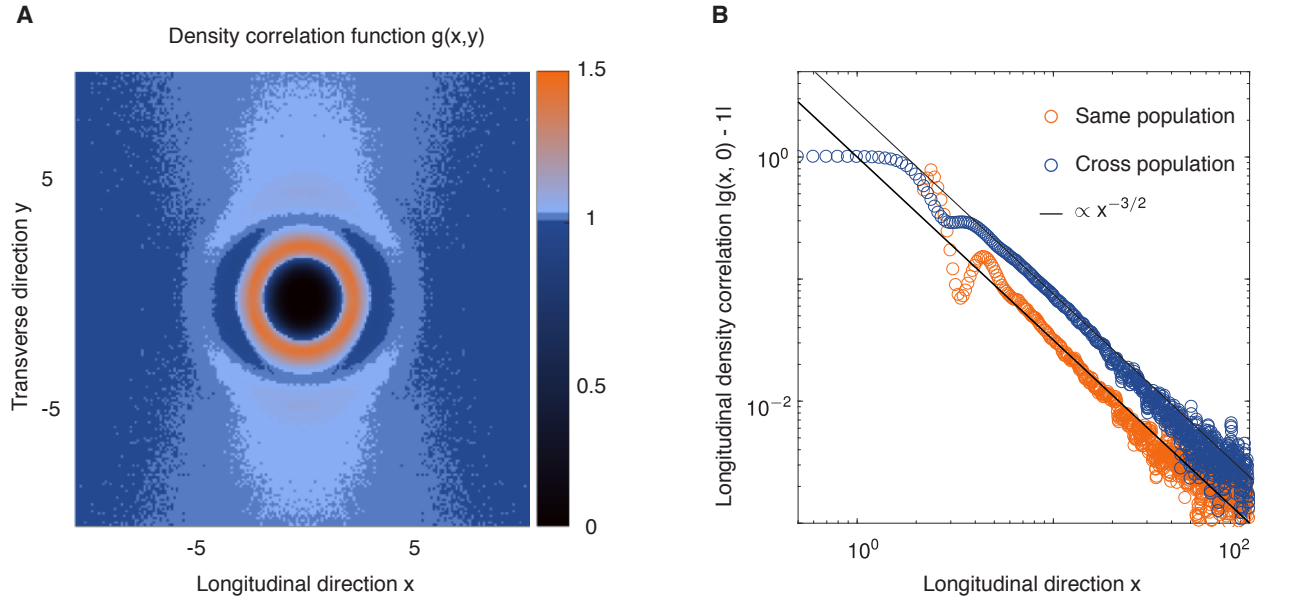

Figure 1.5 | Numerical evidence of long-range structural correlation. (A) Overall pair correlation function $g(x, y)$. (B) Plot of the longitudinal decay of the density auto- (light orange) and cross- (dark blue) correlation functions at $y = 0$. Black lines: algebraic decay $x^{-\frac{3}{2}}$.

5.2 Hydrodynamic description, universal long-range correlations

In the spirit of active hydrodynamics, we described the mingled phase with sets of density ($\rho_{\text{right}}, \rho_{\text{left}}$), velocity ($\mathbf{v}_{\text{right}}, \mathbf{v}_{\text{left}}$), and polarization fields ($\mathbf{p}_{\text{right}}, \mathbf{p}_{\text{left}}$). Since the particles advance at constant speed Eq. (1.3), the polarization and velocity fields are identical. We are therefore left with four coupled dynamic fields, as in driven passive systems. In this section, we highlight the generic ideas that lead to long-range density correlations in both active and passive systems. A complete derivation of the hydrodynamic equations of an active binary liquid in the low and high density limits is provided in the Supplementary informations (6).

The sole conserved quantity here is density. Momentum is conserved neither in active nor in driven liquids, and unlike flocking systems the orientation of the velocity field is not a soft mode. The only true hydrodynamic variables are therefore the density field of each population, and the velocity fluctuations around the mingled state are slaved to the density fluctuations. We can describe the mingled state as homogeneous $\rho_{\text{right}} = \rho_{\text{left}} = \rho_0$ and partly polarized $\mathbf{v}_{\text{right}} = -\mathbf{v}_{\text{left}} = v_0\,\hat{\mathbf{x}}$. For linear fluctuations around this state, mass conservation takes the following form:

$$\partial_t \delta\rho_\alpha + v_0 \partial_x \delta\rho_\alpha + \rho_0 \boldsymbol{\nabla}\cdot\delta\mathbf{v}_\alpha = 0, \tag{1.5}$$

where the α and β indices are generic notations to denote the two different populations. We can phenomenologically express the density-induced velocity fluctuations up to the first order in gradient as: $\rho_0\delta\mathbf{v}_\alpha = -\left[v_{\text{s}}\hat{\mathbf{x}} + D_{\text{s}}\boldsymbol{\nabla}\right]\delta\rho_\alpha - \left[v_{\text{c}}\hat{\mathbf{x}} + D_{\text{c}}\boldsymbol{\nabla}\right]\delta\rho_\beta$. The two constants v_{s} and v_{c} translate the speed change due to an excess or a lack of density, respectively from the same or the crossed species. Similarly, D_{s} and D_{c} translate the effect of the density gradients of each population on the velocity fluctuations. Replacing the velocity fluctuations into the mass conservation Eq. (1.5), we obtain the coupled density conservation laws

$$\partial_{\text{t}}\delta\rho_\alpha + \boldsymbol{\nabla}\cdot\left(\mathbf{J}_\alpha + \mathbf{J}_{\text{c}}\right) = 0, \tag{1.6}$$

where $\mathbf{J}_\alpha = \left[(v_0 - v_{\text{s}})\hat{\mathbf{x}} - D_{\text{s}}\boldsymbol{\nabla}\right]\delta\rho_\alpha$ is the mass flux due to convection and interactions between particles of the same species, and $\mathbf{J}_{\text{c}} = \left[-v_{\text{c}}\hat{\mathbf{x}} - D_{\text{c}}\boldsymbol{\nabla}\right]\delta\rho_\beta$ is the mass flux induced by cross-population interactions. To calculate the density correlations, we assumed that density fluctuations respond to an uncorrelated conserved white noise through the mass conservation equations Eq. (1.6). Going to Fourier space, and after lenghty but straightforward algebra, we obtain in the long wavelength limit the following structure factor:

$$\langle|\delta\rho_\alpha(\mathbf{q})|^2\rangle \propto \frac{D_{\text{s}}^2\, q_{\text{y}}^4 + (v_0 - v_{\text{s}})^2\, q_{\text{x}}^2}{\left[D_{\text{s}}^2 - D_{\text{c}}^2\right]\, q_{\text{y}}^4 + \left[(v_0 - v_{\text{s}})^2 - v_{\text{c}}^2\right]\, q_{\text{x}}^2}, \tag{1.7}$$

where $\mathbf{q} = (q_x, q_y)$ is the spatial wave vector. At vanishing wave vector, the obtained structure factor is non-analytic: its value depends on the way the $\mathbf{q} \to 0$ limit is taken. This non-analycity is at the origin of the long-range density correlations: the inverse Fourier transform of the structure factor leads to density correlations that decay algebraically as $\langle|\rho_\alpha(0,0)\rho_\alpha(x,0)|\rangle = |1 - g_{\alpha\alpha}(x)| \sim x^{-\frac{3}{2}}$. Consequently, these long-range density correlations are a universal feature of any system of oppositely moving populations, passive or active. They will be present as long as there is a coupling between the two populations, either as a transverse diffusivity D_c or a longitudinal convection v_c.

6 Discussion and perspectives

We investigated a model system of active counterflows, and revealed a critical phase transition between a fully laned phase and a mingled phase. Deep in the mingled phase, we numerically evidenced long-range density correlations, and elucidated their origin from a hydrodynamic description. We showed that these correlations were universal to driven and active counterflows. The mingling phase transition, on the contrary, has no known counterpart in passive systems. At this point, two natural perspectives emerge.

The first one is experimental. Measuring the density correlations in experimental setups of oppositely moving populations would be a powerful way to validate or invalidate our universality claims. We do not know, however, if it is technically feasible as it requires observations on very long length scales. Additional experimental works could also provide useful insights into the lane formation process.

The second perspective is theoretical. As mentionned in [76], there is an apparent contradiction in passive driven systems between the continuous increase of lane size and the algebraic decay of the density correlations: infinite density correlation suggests that no length scale can be defined. A comprehensive theoretical framework could solve this contradiction and potentially explain the critical phase transition observed in active systems.

Article

Critical mingling and universal correlations in model binary active liquids

Bain, N. and Bartolo, D. Nat. Commun. 8, 15969 doi: 10.1038/ncomms15969 (2017).

Ensembles of driven or motile bodies moving along opposite directions are generically reported to self-organize into strongly anisotropic lanes. Here, building on a minimal model of self-propelled bodies targeting opposite directions, we first evidence a critical phase transition between a mingled state and a phase-separated lane state specific to active particles. We then demonstrate that the mingled state displays algebraic structural correlations also found in driven binary mixtures. Finally, constructing a hydrodynamic theory, we single out the physical mechanisms responsible for these universal long-range correlations typical of ensembles of oppositely moving bodies.

Introduction

Should you want to mix two groups of pedestrians, or two ensembles of colloidal beads, one of the worst possible strategies would be pushing them towards each other. Both experiments and numerical simulations have demonstrated the segregation of oppositely driven Brownian particles into parallel lanes [27, 57, 97, 54, 34]. Even the tiniest drive results in the formation of finite slender lanes which exponentially grow with the driving strength [34]. The same qualitative phenomenology is consistently observed in pedestrian counterflows [70, 60, 46, 55, 63]. From our daily observation of urban traffic to laboratory experiments, the emergence of counter propagating lanes is one of the most robust phenomena in population dynamics, and has been at the very origin of the early description of pedestrians as granular materials [45, 41]. However, a description as isotropic grains is usually not sufficient to account for the dynamics of interacting motile bodies [59, 104, 11]. From motility-induced phase separation [11], to giant density fluctuations in flocks [91, 93, 59], to pedestrian scattering [65, 66], the most significant collective phenomena in active matter stem from the interplay between their position and orientation degrees of freedom.

In this communication, we address the phase behavior of a binary mixture of active particles targeting opposite directions. Building on a prototypical model of self-propelled bodies with repulsive interactions, we numerically evidence two nonequilibrium steady states: a lane state where the two

populations maximize their flux and phase separate, and a mixed state where all motile particles mingle homogeneously. We show that these two distinct states are separated by a genuine critical phase transition. In addition, we demonstrate algebraic density correlations in the homogeneous phase, akin to that recently reported for oppositely driven Brownian particles [76]. Finally, we construct a hydrodynamic description to elucidate these long-range structural correlations, and conclude that they are universal to both active and driven ensembles of oppositely-moving bodies.

Results

A minimal model of active binary mixtures

We consider an ensemble of N self-propelled particles characterized by their instantaneous positions $\mathbf{r}_i(t)$ and orientations $\hat{\mathbf{p}}_i(t) = (\cos\theta_i, \sin\theta_i)$, where $i = 1, \ldots, N$ (in all that follows $\hat{\mathbf{x}}$ stands for $\mathbf{x}/|\mathbf{x}|$). Each particle moves along its orientation vector at constant speed ($|\dot{\mathbf{r}}_i| = 1$). We separate the particle ensemble into two groups of equal size following either the direction $\Theta_i = 0$ (right movers) or π (left movers) according to a harmonic angular potential $\mathcal{V}(\theta_i) = \frac{H}{2}(\theta_i - \Theta_i)^2$. Their equations of motion take the simple form:

$$\dot{\mathbf{r}}_i = \hat{\mathbf{p}}_i, \tag{1.8}$$

$$\dot{\theta}_i = -\partial_{\theta_i}\mathcal{V}(\theta_i) + \sum_j T_{ij}. \tag{1.9}$$

In principle, oriented particles can interact via both forces and torques. We here focus on the impact of orientational couplings and consider that neighbouring particles interact solely through pairwise additive torques T_{ij}. This type of model has been successfully used to describe a number of seemingly different active systems, starting from bird flocks, fish schools and bacteria colonies to synthetic active matter made of self-propelled colloids or polymeric biofilaments [96, 59, 13, 22, 9, 18, 86, 10]. We here elaborate on a minimal construction where the particles interact only via repulsive torques. In practical terms, we choose the standard form $T_{ij} = -\partial_{\theta_i}\mathcal{E}_{ij}$, where the effective angular energy simply reads $\mathcal{E}_{ij} = -B(r_{ij})\hat{\mathbf{p}}_i.\hat{\mathbf{r}}_{ij}$. As sketched in Fig. 1.6a, this interaction promotes the orientation of $\hat{\mathbf{p}}_i$ along the direction of the center-to-center vector $\mathbf{r}_{ij} = (\mathbf{r}_i - \mathbf{r}_j)$: as they interact particles turn their back to each other (see also e.g. [9, 12, 35, 98]). The spatial decay of the interactions is given by: $B(r_{ij}) = B\,(1 - r_{ij}/(a_i + a_j))$, where B is a finite constant if $r_{ij} < (a_i + a_j)$ and 0 otherwise. In all that follows we focus on the regime where repulsion overcomes alignment along the preferred direction ($B > 1$). The interaction ranges a_i are chosen to be polydisperse in order to avoid the specifics of crystallization, and we make the classic choice $a = 1$ or 1.4 for one in every two particles. Before solving Eqs. (1.8) and (1.9), two comments are in order. Firstly, this model is not intended to provide a faithful description of a specific experiment. Instead, this minimal setup is used to single out the importance of repulsion torques typical of active bodies. Any more realistic description would also include hard-core interactions. However, in the limit of dilute ensembles and long-range repulsive torques, hard-core interactions are not expected to alter any of the results presented below. Secondly, unlike models of driven colloids or grains interacting via repulsive forces [27, 34, 76], Eqs. (1.8) and (1.9) are not invariant upon Gallilean boosts, and therefore are not suited to describe particles moving at different speeds along the same preferred direction.

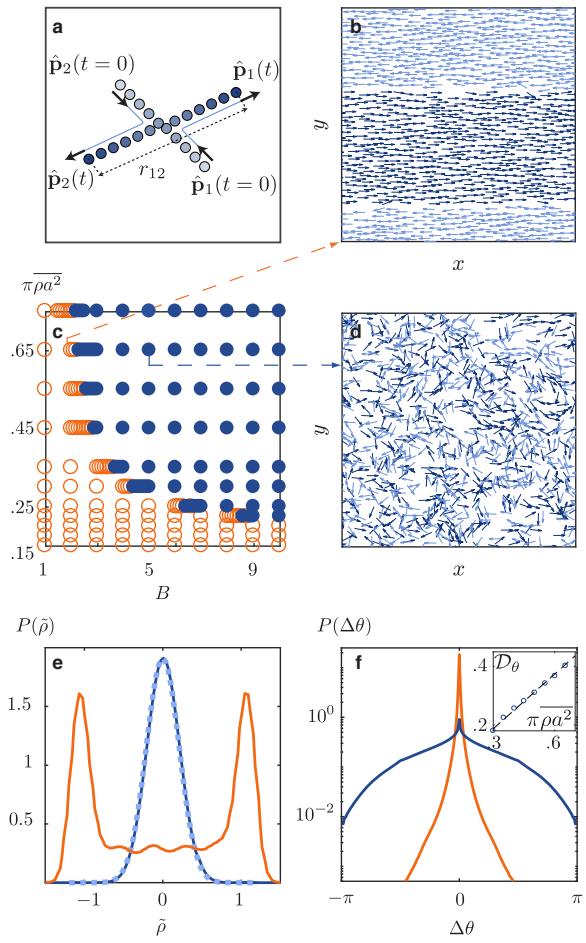

Figure 1.6 | Phase behavior. (a) Trajectories of two particles interacting solely via a repulsive torque as defined in Eq. (1.9) with $B = 5$. The post-collision orientations $\hat{\mathbf{p}}_i(t)$ are along the center to center axis r_{ij}. (b) and (d) Snapshots of a square window at the center of the simulation box ($L_x = 168$, $N = 1973$, $\pi\overline{\rho a^2} = 0.65$), respectively in the lane ($B = 2$) and the homogeneous ($B = 5$) states. The arrows indicate the instantaneous position and orientation of the particles. Dark blue: right movers. Light blue: left movers. (c) Phase diagram. $\pi\overline{\rho a^2}$ is the particle area fraction. Filled symbols: homogeneous state. Open symbols: lanes. (e) Probability distribution of the density difference $\tilde{\rho} = \rho_r - \rho_l$. Light orange line: $B = 2$, $\pi\overline{\rho a^2} = 0.65$. Dark blue line: $B = 5$, $\pi\overline{\rho a^2} = 0.65$. Dashed line: best Gaussian fit. (f) P.d.f. of the orientational fluctuations around the preferred orientation (lin-log plot). Same parameters and colors as in (e). Inset: orientational diffusivity $\mathcal{D}_\theta$ in the homogeneous state at a fixed repulsion magnitude ($B = 5$) and different particle area fractions $\pi\overline{\rho a^2}$. $\mathcal{D}_\theta$ is defined as the decorrelation time of the particle orientation. In the mingled state, the velocity autocorrelation decays exponentially at short time, $\mathcal{D}_\theta$ is therefore defined without ambiguity, see also Supplementary Note 1 for a full description of the numerical computation of $\mathcal{D}_\theta$. Dashed line: best linear fit.

Critical mingling

Starting from random initial conditions, we numerically solve Eqs. (1.8) and (1.9) using forward Euler integration with a time step of 10^{-2}, and a sweep-and-prune algorithm for neighbour summation. We use a rectangular simulation box of aspect ratio $L_x = 2L_y$ with periodic boundary conditions in both directions. We also restrain our analysis to $H = 1$, leaving two control parameters that are the repulsion strength B and the overall density $\bar{\rho}$. The following results correspond to simulations with N comprised between 493 and 197,300 particles.

We observe two clearly distinct stationary states illustrated in Figs. 1.6b and 1.6d. At low density and/or weak repulsion the system quickly phase separates. Computing the local density difference between the right and left movers $\tilde{\rho}(\mathbf{r}, t) = \rho_r(\mathbf{r}, t) - \rho_l(\mathbf{r}, t)$, we show that this dynamical state is characterized by a strongly bimodal density distribution, see Fig. 1.6e. The left and right movers quickly self-organize into counter-propagating lanes separated by a sharp interface, Fig. 1.6b. In each stream, virtually no particle interact and most of the interactions occur at the interface. As a result the particle orientations are very narrowly distributed around their mean value, Fig. 1.6f. In stark contrast, at high density and/or strong repulsion, the motile particles do not phase separate. Instead, the two populations mingle and continuously interact to form a homogeneous liquid phase with Gaussian density fluctuations, and much broader orientational fluctuations, Figs. 1.6d, 1.6e, and 1.6f. This behavior is summarized by the phase diagram in Fig. 1.6c. Although phase separation is most often synonymous of first order transition in equilibrium liquids, we now argue that the lane and the mingled states are two genuine non-equilibrium phases separated by a critical line in the $(B, \bar{\rho})$ plane. To do so, we first introduce the following orientational order parameter:

$$\langle W \rangle = \langle 1 - \cos(\theta_i - \Theta_i) \rangle_i. \tag{1.10}$$

$\langle W \rangle$ vanishes in the lane phase where on average all particles follow their preferred direction, and takes a non zero value otherwise. We show in Fig. 1.7a how $\langle W \rangle$ increases with the repulsion strength B at constant $\bar{\rho}$. For $\pi\overline{\rho a^2} = 0.65$ the order parameter averages to zero below $B_c = 2.17 \pm 0.02$, while above B_c it sharply increases as $W \sim |B - B_c|^\beta$, with $\beta = 0.33 \pm 0.07$, Fig. 1.7b. This scaling law suggests a genuine critical behavior. We further confirm this hypothesis in Fig. 1.7c, showing that the fluctuations of the order parameter diverge as $|B - B_c|^{-\gamma}$, with $\gamma = 0.64 \pm 0.07$. Deep in the homogeneous phase the fluctuations plateau to a constant value of the order of $1/N$. Finally, the criticality hypothesis is unambiguously ascertained by Fig. 1.7d, which shows the power-law divergence of the correlation time of $\langle W \rangle(t)$: $\tau_W \sim |B - B_c|^{-z\nu}$ with $z\nu = 1.21 \pm 0.16$.

We do not have a quantitative explanation for this criticla behavior. However, we can gain some insight from the counterintuitive two-body scattering between active particles. In the overdamped limit, the collision between two passive colloids driven by an external field would at most shift their position over an interaction diameter [52]. Here these transverse displacements are not bounded by the range of the repulsive interactions. For a finite set of impact parameters, collisions between self-propelled particles result in persistent deviations transverse to their preferred trajectories illustrated in Fig. 1.8 and Supplementary Note 2. This persistent scattering stems from the competition between repulsion and alignement. When these two contributions compare, bound pairs of oppositely moving particles can even form and steadily propel along the transverse direction $\hat{\mathbf{y}}$, Figs. 1.8a and 1.8b. We stress that this behavior is not peculiar to this two-body setting: persistent transverse motion of bound pairs is clearly observed in simulations at the onset of laning. We therefore strongly suspect the resulting enhanced mixing to be at the origin of the sharp melting of the lanes and the emergence of the mingled state.

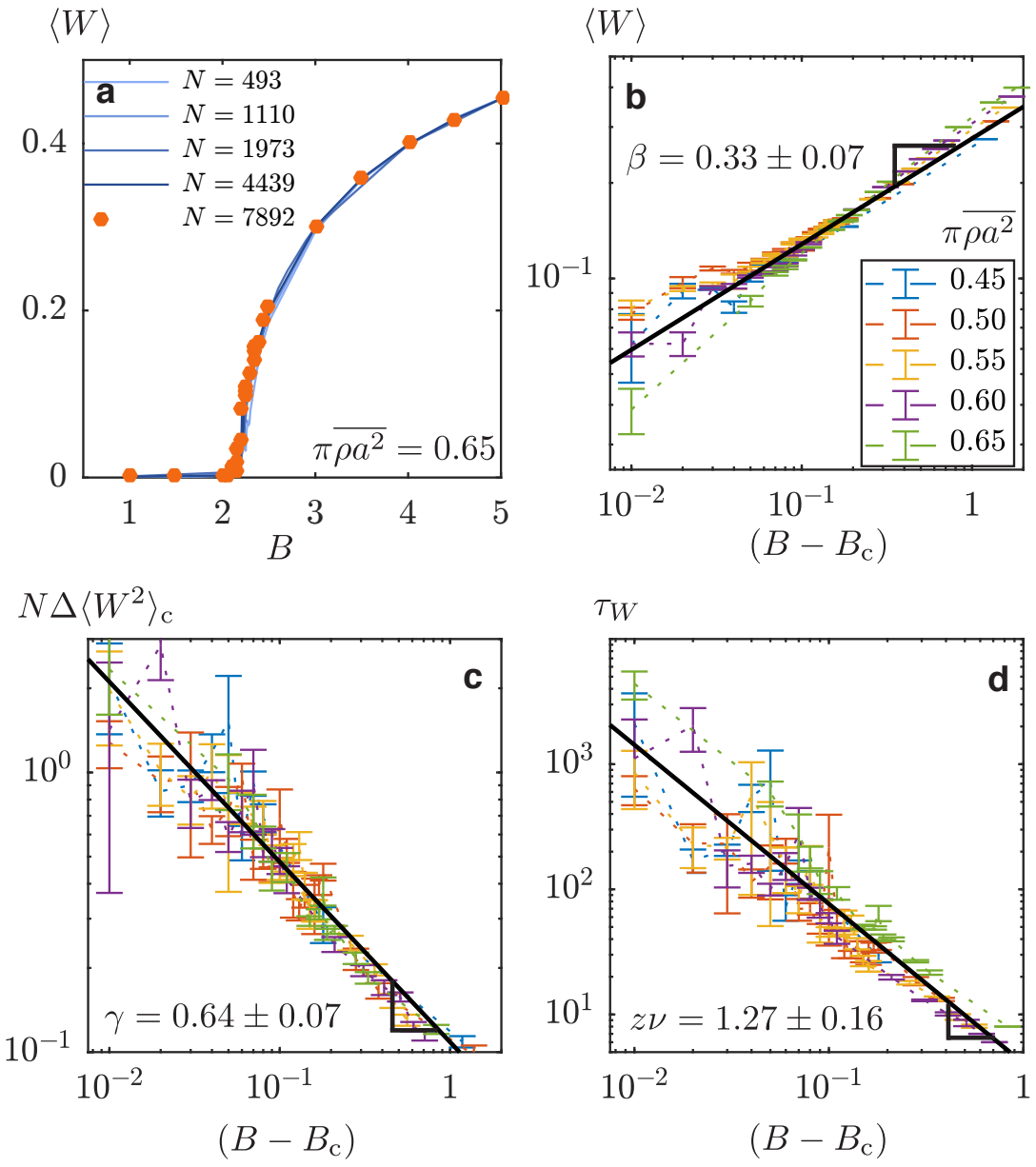

Figure 1.7 | Critical transition from laned to homogeneous liquid states. (a) and (b) Linear and log plots of the order parameter $\langle W\rangle$ defined in Eq. (1.10). (a): $\pi\overline{\rho a^2} = 0.65$, the bifurcation curves collapse for five system sizes. (b), (c) and (d) Log plots at five densities for a box of length $L_x = 336$ (N ranges from 5462 to 7892). (c) Fluctuations of the order parameter plotted versus $B - B_c$ for the same densities as in (b). The fluctuations are defined as $\Delta\langle W^2\rangle_c \equiv \langle W^2\rangle_c(B) - \langle W^2\rangle_c(B \to \infty)$. (d) Correlation time τ_W plotted against $B - B_c$. The correlation time is defined as $\langle W(t+\tau_W)W(t)\rangle_c = \frac{1}{2}\langle W^2(t)\rangle_c$. All error bars correspond to two standard deviations. The error on the estimate of the exponents correspond to one standard deviation after considering linear fits for each density.

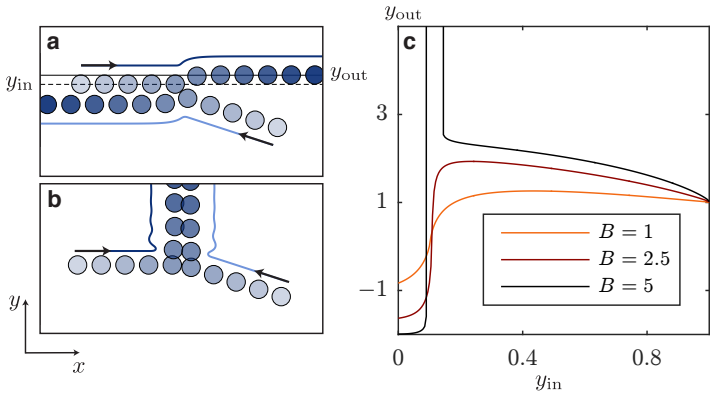

Figure 1.8 | Collision between left and right movers. (a) and (b) Trajectories of two colliding particles in the presence of an alignment field. The trajectories before contact are prolongations of the incoming orientations, both interactions and alignment field are only turned on at contact. (a) Scattering trajectory for $B = 5$, and $y_{\rm in} = 0.75$. $y_{\rm in}$ (resp. $y_{\rm out}$) is the initial (resp. final) vertical position of the right mover with respect to the contact point. $y_{\rm in}$ (resp. $y_{\rm out}$) is represented by the dashed line (resp. plain line). (b) Example of collision resulting in a strong and persistent deviation along the transverse direction ($B = 5$, $y_{\rm in} = 0.125$). (c) The transverse displacement $y_{\rm out}$ is plotted as a function of the impact parameter $y_{\rm in}$ as defined in (a), for different values of the repulsion strength B. Initial conditions: a right mover with an orientation $\theta_{\rm r} = 0$ and a left mover with $\theta_{\rm l} = \pi - \pi/10$ are vertically placed at $+y_{\rm in}$ and $-y_{\rm in}$. Their x coordinate is chosen so that they start interacting at $t = 0$.

Long-range correlations in mingled liquids

We now evidence long-range structural correlations in this active-liquid phase, and analytically demonstrate their universality. The overall pair correlation function of the active liquid, $g(\mathbf{r})$, is plotted in Fig. 1.9a. At a first glance, deep in the homogeneous phase, the few visible oscillations would suggest a simple anisotropic liquid structure. However, denoting α and β the preferred direction of the populations (left or right), we find that the asymptotic behaviors of all pair correlation functions $g_{\alpha\beta}(x, y = 0)$ decay algebraically as $|1 - g_{\alpha\beta}(x, 0)| \sim x^{-\nu_{\rm x}}$ with $\nu_{\rm x} \sim 1.5$, Fig. 1.9b. This power-law behavior is very close to that reported in numerical simulations [54] and fluctuating density functional theories of oppositely driven colloids at finite temperature [76].

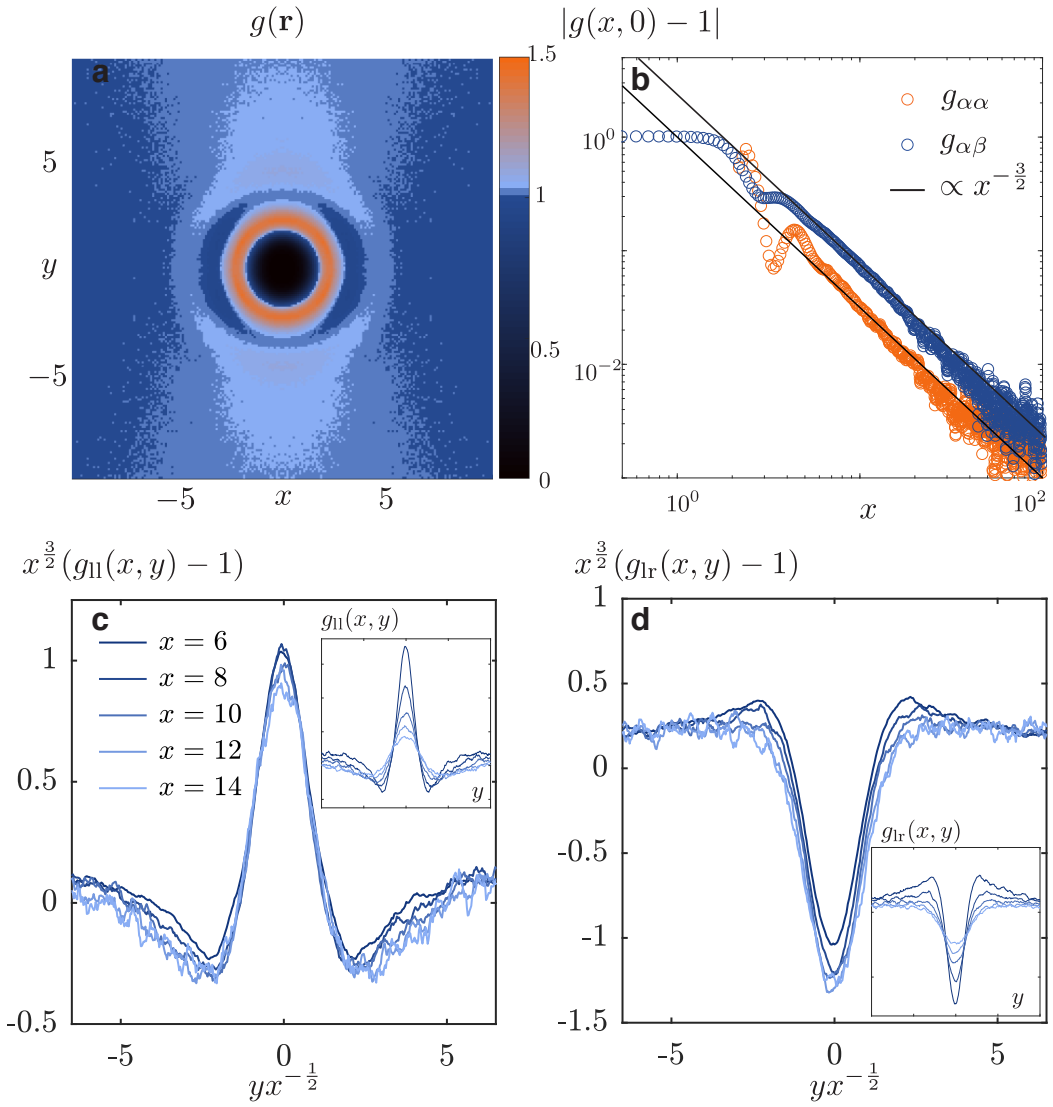

Figure 1.9 | Structural correlations. (a) Overall pair correlation function deep in the homogeneous phase ($B = 5$). (b) Plot of the longitudinal decay of the density auto- (light orange) and cross- (dark blue) correlation functions at $y = 0$. Black lines: algebraic decay $x^{-\frac{3}{2}}$. (c) and (d) Collapse of the pair correlations once rescaled by the universal $x^{-3/2}$ power law and plotted as a function of the rescaled distance $y/\sqrt{x}$. Insets: bare correlations. The good collapse of the rescaled curves supports the validity of the scaling deduced from the linearized fluctuating hydrodynamics. $B = 5$, $\pi\overline{\rho a^2} = 0.65$ and $L_y = 84$ for all panels. $N = 197,300$ particles in (b) and $N = 31,566$ in (a), (c) and (d).

Hydrodynamic description

In order to explain the robustness of these long-range correlations, we provide a hydrodynamic description of the mingled state, and compute its structural response to random fluctuations. We first observe that the orientational diffusivity of the particles increases linearly with the average density $\overline{\rho}$ in Fig. 1.6f inset. This behavior indicates that binary collisions set the fluctuations of this active liquid, and hence suggests using a Boltzmann kinetic-theory framework, see e.g [74, 89] from an active-matter perspective. In the large B limit, the microscopic interactions are accounted for by a simplified scattering rule anticipated from Eq. (1.9) and confirmed by the inspection of typical trajectories (see Fig. 1.6a). Upon binary collisions the self-propelled particles align their orientation with the center-to-center axis regardless of their initial orientation and external drive. Assuming molecular chaos and binary collisions only, the time evolution of the one-point distribution functions $\psi_\alpha(\mathbf{r},\theta,t)$ reads:

$$\partial_t\psi_\alpha + \boldsymbol{\nabla}\cdot[\hat{\mathbf{p}}\psi_\alpha] + \partial_\theta\left[\partial_\theta\left(\hat{\mathbf{p}}\cdot\hat{\mathbf{h}}_\alpha\right)\psi_\alpha\right] = \mathcal{I}_\alpha^{\mathrm{coll}}. \tag{1.11}$$

The convective term on the l.h.s stems from self-propulsion, the third term accounts for alignment with the preferred direction $\hat{\mathbf{h}}_\alpha = \hat{\mathbf{x}}$ (resp. $-\hat{\mathbf{x}}$) for the right (resp. left) movers. Using the simplified scattering rule to express the so-called collision integral on the r.h.s, we can establish the dynamical equations for the density fluctuations $\delta\rho_\alpha$ around the average homogeneous state (see Methods for technical details). Within a linear response approximation, they take the compact form:

$$\partial_t\delta\rho_\alpha(\mathbf{r},t) + \boldsymbol{\nabla}\cdot(\mathbf{J}_\alpha + \tilde{\mathbf{J}}) = 0, \tag{1.12}$$

where $\mathbf{J}_\alpha$ describes the convection and the collision-induced diffusion of the α species, and $\tilde{\mathbf{J}}$ is the coupling term, crucial to the anomalous fluctuations of the active liquid:

$$\mathbf{J}_\alpha = v_0\hat{\mathbf{h}}_\alpha\delta\rho_\alpha - \mathbf{D}\cdot\boldsymbol{\nabla}\delta\rho_\alpha, \tag{1.13}$$

$$\tilde{\mathbf{J}} = -\tilde{v}\hat{\mathbf{h}}_\alpha\delta\overline{\rho} - \tilde{\mathbf{D}}\cdot\boldsymbol{\nabla}\delta\overline{\rho},. \tag{1.14}$$

The two anisotropic diffusion tensors $\mathbf{D}$ and $\tilde{\mathbf{D}}$ are diagonal and their expression is provided in Supplementary Note 3 together with all the hydrodynamic coefficients. $\tilde{\mathbf{J}}$ is a particle current stemming from the fluctuations of the other species and has two origins. The first term arises from the competition between alignment along the driving direction $\hat{\mathbf{h}}_\alpha$ and orientational diffusion caused by the collisions: the higher the local density $\overline{\rho}$, the smaller the longitudinal current. The second term originates from the pressure term $\propto \boldsymbol{\nabla}\overline{\rho}$: a local density gradient results in a net flow of both species (see Methods for details). This diffusive coupling is therefore generic and enters the description of any binary compressible fluid. Two additional comments are in order. Firstly, this prediction is not specific to the small-density regime and is expected to be robust to the microscopic details of the interactions. As a matter of fact, the above hydrodynamic description is not only valid in the limit of strong repulsion and small densities discussed above but also in the opposite limit, where the particle density is very large while the repulsion remains finite as detailed in the Supplementary Note 5. Secondly, the robustness of this hydrodynamic description could have been anticipated using conservation laws and symmetry considerations, as done e. g. in [91] for active flocks. Here the situation is simpler, momentum is not conserved and no soft mode is associated to any spontaneous symmetry breaking. As a result the only two hydrodynamic variables are the coupled (self-advected) densities of the two populations [16]. The associated mass currents are constructed from the only two vectors that can be formed in this

homogeneous but anisotropic setting: $\mathbf{h}_\alpha$ and $\boldsymbol{\nabla}\delta\rho_\alpha$. These simple observations are enough to set the functional form of Eqs. (1.12), (1.13) and (1.14).

By construction the above hydrodynamic description alone cannot account for any structural correlation. In order to go beyond this mean-field picture we classically account for fluctuations by adding a conserved noise source to Eqs. (1.12) and compute the resulting density-fluctuation spectrum [59]. At the linear response level, without loss of generality, we can restrain ourselves to the case of an isotropic additive white noise of variance $2T$ (see Supplementarty Note 4). Going to Fourier space, and after lengthy yet straightforward algebra we obtain in the long wavelength limit:

$$\langle|\delta\rho_\alpha(\mathbf{q})|^2\rangle \propto \frac{q_{\rm y}^4(D_{\rm y}+\tilde{D}_{\rm y})^2+q_{\rm x}^2(v_0-\tilde{v})^2}{q_{\rm y}^4 D_{\rm y}(D_{\rm y}+2\tilde{D}_{\rm y})+q_{\rm x}^2 v_0(v_0-2\tilde{v})} \tag{1.15}$$

with $\delta\rho(\mathbf{q})=\int\delta\rho(\mathbf{r})\exp(-i\mathbf{q}\cdot\mathbf{r})\mathrm{d}\mathbf{r}$, and where $\langle\cdot\rangle$ is a noise average. The cross-correlation $\langle\delta\rho_\alpha(\mathbf{q})\delta\rho_\beta(-\mathbf{q})\rangle$ has a similar form, see Supplementary Note 4. Even though the above hydrodynamic description qualitatively differs from that of driven colloids, they both yield the same fluctuation spectra [76]. A key observation is that the structure factor given by Eq. (1.15) is non analytic at $q=0$. Approaching $q=0$ from different directions yields different limits, which is readily demonstrated noting that $\langle|\delta\rho_\alpha(q_{\rm x},q_{\rm y}=0)|^2\rangle$ and $\langle|\delta\rho_\alpha(q_{\rm x}=0,q_{\rm y})|^2\rangle$ are both constant functions but have different values. The non analyticity of Eq. (1.15) in the long wavelength limit translates in an algebraic decay of the density correlations in real space. After a Fourier transform we find: $\langle|\rho_\alpha(0,0)\rho_\alpha(x,0)|\rangle=|1-g_{\alpha\alpha}(x)|\sim x^{-\frac{3}{2}}$, in agreement with our numerical simulations of both self-propelled particles, Fig. 1.9b, and driven colloids, see [54, 76]. Beyond these long-range correlations it can also be shown (see Supplementary Note 4) that the pair correlation functions take the form $|1-g_{\alpha\beta}(x,y)|\sim x^{-3/2}\mathcal{C}(y/x^{1/2})$ again in excellent agreement with our numerical findings. Figs. 1.9c and 1.9d indeed confirm that the pair correlations between both populations are correctly collapsed when normalized by $x^{-3/2}$ and plotted versus the rescaled distance $y/x^{1/2}$.

Discussion

Different non-equilibrium processes can result in algebraic density correlations with different power laws, see e.g. [36]. We thus need to identify the very ingredients yielding universal $x^{-\frac{3}{2}}$ decay, or equivalently structure factors of the form $\langle|\delta\rho_\alpha(\mathbf{q})|^2\rangle\propto(q_{\rm y}^4+a^2q_{\rm x}^2)/(q_{\rm y}^4+b^2q_{\rm x}^2)$ found both in active and driven binary mixtures. We first recall that this structure factor has been computed from hydrodynamic equations common to any system of coupled conserved fields in a homogeneous and anisotropic setting (regardless of the associated noise anisotropy, see [36] and Supplementary Note 4). The structure factor is non-analytic as $q\to0$, and the density correlations algebraic, only when $a\neq b$. Inspecting Eq. (1.15), we readily see that this condition is generically fulfilled as soon as the coupling current $\tilde{\mathbf{J}}$ is non zero. In other words, as soon as the collisions between the particles either modify their transverse diffusion ($\tilde{\mathbf{D}}\cdot\boldsymbol{\nabla}\delta\overline{\rho}$), or their longitudinal advection ($\tilde{v}\hat{\mathbf{h}}_\alpha\delta\overline{\rho}$). Both ingredients are present in our model of active particles (see Eq. (1.12)) and, based on symmetry considerations, should be generic to any driven binary mixtures with local interactions. Another simple physical explanation can be provided to account for the variations of the pair correlations in the transverse direction shown in Figs. 1.9c and 1.9d and also reported in simulations of driven particles [76]. Self-propulsion causes the particles to move, on average, at constant speed along the x-direction while frontal collisions induce their transverse diffusion. As a result the x-position of the particles increase linearly with time, and their transverse

position increases as $\sim t^{1/2}$. We therefore expect the longitudinal and transverse correlations to be related by a homogeneous function of $y/x^{1/2}$ in steady state as observed in simulations of both active and driven particles. Altogether these observations confirm the universality of the long-range structural correlations found in both classes of non-equilibrium mixtures.

In conclusion, we have demonstrated that the interplay between orientational and translational degrees of freedom, inherent to motile bodies, can result in a critical transition between a phase separated and a mingled state in binary active mixtures. In addition we have singled out the very mechanisms responsible for long-range structural correlations in any ensemble of particles driven towards opposite directions, should they be passive colloids or self-propelled agents.

Methods

Boltzmann kinetic theory

Let us summarize the main steps of the kinetic theory employed to establish Eqs. (1.12), (1.13) and (1.14). The so-called collision integral on the r.h.s of Eq. (1.11) includes two contributions which translate the behavior illustrated in Fig. 1.6a:

$$\mathcal{I}_\alpha^{\rm coll} = \mathcal{D}_{\rm in}\rho_\alpha(\mathbf{r})\overline{\rho}(\mathbf{r}-2a\hat{\mathbf{p}}) - \mathcal{D}_{\rm out}\overline{\rho}(\mathbf{r})\psi_\alpha(\mathbf{r},\theta). \tag{1.16}$$

The first term indicates that a collision with any particle located at $(\mathbf{r}-2a\hat{\mathbf{p}})$ reorients the α particles along $\hat{\mathbf{p}}(\theta)$ at a rate $\mathcal{D}_{\rm in}$. The second term accounts for the random reorientation, at a rate $\mathcal{D}_{\rm out}$, of a particle aligned with $\hat{\mathbf{p}}(\theta)$ upon collision with any other particle. Within a two-fluid picture, the velocity and nematic texture of the α particles are given by $\mathbf{v}_\alpha = \rho_\alpha^{-1}\langle\hat{\mathbf{p}}\rangle_\theta$ and $\mathbf{Q}_\alpha = \rho_\alpha^{-1}\langle\hat{\mathbf{p}}\hat{\mathbf{p}} - \frac{1}{2}\mathbb{I}\rangle_\theta$. The mass conservation relation, $\partial_{\rm t}\rho_\alpha + \boldsymbol{\nabla}\cdot(\rho_\alpha\mathbf{v}_\alpha) = 0$, is obtained by integrating Eq. (1.11) with respect to θ and constrains $(2\pi\mathcal{D}_{\rm in}) = \mathcal{D}_{\rm out} \equiv \mathcal{D}$. The time evolution of the velocity field is also readily obtained from Eq. (1.11):

$$\partial_{\rm t}(\rho_\alpha\mathbf{v}_\alpha) + \boldsymbol{\nabla}\cdot\left[\rho_\alpha\left(\frac{\mathbb{I}}{2}+\mathbf{Q}_\alpha\right)\right] = \boldsymbol{\mathcal{F}}_\alpha, \tag{1.17}$$

where the second term on the l.h.s is a convective term stemming from self-propulsion. The force field $\boldsymbol{\mathcal{F}}_\alpha$ on the r.h.s of Eq. (1.17) reads: $\boldsymbol{\mathcal{F}}_\alpha = \rho_\alpha\left(\frac{\mathbb{I}}{2}-\mathbf{Q}_\alpha\right)\cdot\hat{\mathbf{h}}_\alpha - (a\mathcal{D}\rho_\alpha)\boldsymbol{\nabla}\overline{\rho} - (\mathcal{D}\overline{\rho})\rho_\alpha\mathbf{v}_\alpha$. The first term originates from the alignment of particles along the $\hat{\mathbf{h}}_\alpha$ direction, the second term is a repulsion-induced pressure, and the third one echoes the collision-induced rotational diffusivity of the particles. An additional closure relation between $\mathbf{Q}_\alpha$, $\mathbf{v}_\alpha$ and ρ_α is required to yield a self-consistent hydrodynamic description. Deep in the homogeneous phase, we make a wrapped Gaussian approximation for the orientational fluctuations in each population [9, 81]. This hypothesis is equivalent to setting $\mathbf{Q}_\alpha = |\mathbf{v}_\alpha|^4(\hat{\mathbf{v}}_\alpha\hat{\mathbf{v}}_\alpha - \frac{1}{2}\mathbb{I})$ [9, 8]. As momentum is not conserved, the velocity field is not a hydrodynamic variable; in the long wavelength limit the velocity modes relax much faster than the (conserved) density modes. We therefore ignore the temporal variations in Eq. (1.17) and use this simplified equation to eliminate $\mathbf{v}_\alpha$ in the mass-conservation relation, leading to the mass conservation equation Eq. (1.12).

Supplementary information

Supplementary Note 1: Orientational Diffusivity

We explain the method used to measure the orientational diffusivity shown in Fig. 1f in the main document. This measurement is reported only for particles in the homogeneous mingled state. The results below correspond to $B = 5$ and $\pi\overline{\rho a^2} \geq 0.3$. We first compute the autocorrelation function of the particle orientation: $\langle \hat{\mathbf{p}}_i(t+T) \cdot \hat{\mathbf{p}}_i(t) \rangle_{i,\mathrm{t}}$ where the average is performed both over the particles and the reference time t. This function decays exponentially with the lag time T as shown in Supplementary Figure 1.10a. $\mathcal{D}_\theta$ is therefore unambiguously defined from the associated decorrelation time from an exponential fit. Repeating the same measurement for different densities we find that $\mathcal{D}_\theta$ increases linearly with $\overline{\rho}$, as shown in Supplementary Figure 1.10b.

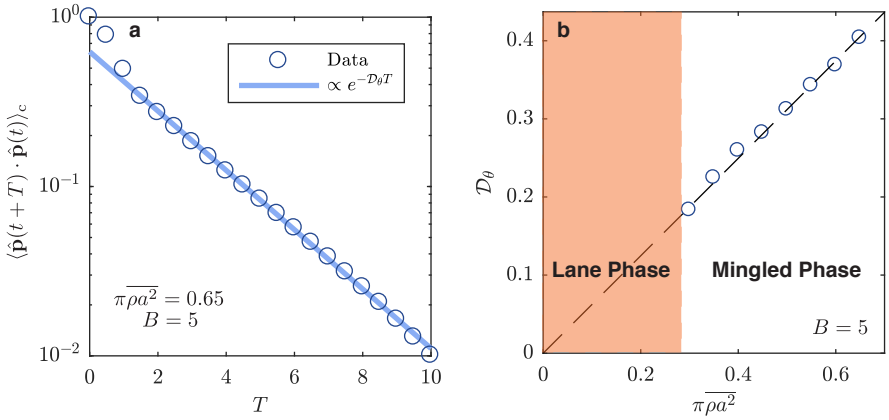

Figure 1.10 | Computation of the orientational diffusivity. (a) Log-lin plot of the orientational diffusivity. Dark blue circles: Numerical time autocorrelation function of the unit orientation vector $\hat{\mathbf{p}}$ averaged over all the particles, in the mingled phase at repulsion magnitude $B = 5$ and density $\pi\overline{\rho a^2} = 0.65$. Light blue line: best exponential fit. (b) Orientational diffusivity $\mathcal{D}_\theta$ as a function of the particle area fracion $\pi\overline{\rho a^2}$, at constant repulsion magnitude $B = 5$. It is very nicely approached by a linear fit starting from the origin. The orange area represents the location of the lane phase.

Supplementary Note 2: Persistent transverse scattering

In this section we study the scattering dynamics of two self-propelled particles of unit radius. For this purpose, let us consider a left mover l and a right mover r, and place the origin of time when contact starts, i.e. when the two interaction disks are tangent. The equations of motion, Supplementary Equations (1.18) and (1.19), which we recall below, tell us that the scattering dynamics are fully determined by the magnitude of the repulsive interactions B, the initial orientation of each particle,

$\theta_{\mathrm{r}}(t=0)$ and $\theta_{\mathrm{l}}(t=0)$, and by the initial orientation of the center-to-center vector $\mathbf{r}_{\mathrm{rl}}(t=0)$.

$$\dot{\mathbf{r}}_i = \hat{\mathbf{p}}_i, \tag{1.18}$$

$$\dot{\theta}_i = -\partial_{\theta_i}\mathcal{V}(\theta_i) + \sum_j T_{ij}. \tag{1.19}$$

Since we assume the particles to be tangent, we are free to place the origin of the $y-$coordinate $y=0$ halfway between the two particles, making the orientation of the center-to-center vector simply equivalent to the initial vertical position of the right mover: $y_{\mathrm{in}} = y_{\mathrm{r}}(0) = [y_{\mathrm{r}}(0) - y_{\mathrm{l}}(0)]/2$, see Supplementary Figure 1.11a. We are therefore left with a four dimensional parameter space.

A. Frontal collision

As a first approach it is instructive to restrain ourselves to frontal collisions, corresponding to $\theta_{\mathrm{r}}(0)=0$ and $\theta_{\mathrm{l}}(0)=\pi$. This situation is particularly relevant to very dilute systems, where the particles have time to perfectly realign with their respective external fields between each collision. The sole impact parameter in this case is the initial vertical distance. Solving the equations of motion, we notice that when the repulsion magnitude increases, so does the final vertical position $y_{\mathrm{out}} = y_{\mathrm{r}}(t\to\infty)$. Moreover, in contrast with what is expected for hardcore repulsion or oppositely driven colloids, it is almost always different from one particle radius (i.e. $y_{\mathrm{out}}=1$), see Supplementary Figure 1.11b. This can be explained by the competition between the colliding and alignment along the external field. Since no exclusion process is implemented, a weak repulsion implies that the particles realign faster than they deviate from the external field, which results in a small vertical displacement $y_{\mathrm{out}}<1$. Conversely, strong repulsion implies that the particles persist in their deviation for a longer period of time before they realign with the field, leading to $y_{\mathrm{out}}>1$. For $y_{\mathrm{in}}>1$ however, no collision occurs and we simply recover $y_{\mathrm{in}}=y_{\mathrm{out}}$. Overall, the transverse scattering of opposite self-propelled particles is strongly enhanced by the magnitude of the repulsive torque B.

B. Transverse motion

This is, however, just a part of the story. Let us now assume that the collision is not frontal, but that the left mover has an incoming angle of $\theta_{\mathrm{l}}(0)=\pi-\epsilon$. Solving the equations of motion numerically, we find that the two particles can effectively stick to each other and travel upwards or downwards as a bound pair, as illustrated in Supplementary Figures 1.11c and 1.11d. This counterintuitive behavior can be however easily explained. Bound pairs form when the two particles turn together either upwards or downwards to avoid each other. In such cases alignement and repulsion compete, and the particles get stuck in this movement until an external event (such as another collision) breaks the pair. The existence of this peculiar solution can be found analytically by looking at the steady state solution of two interacting particles. The $\theta_{\mathrm{r}}=\theta_{\mathrm{l}}=\pm\frac{\pi}{2}$ solution always exists, and it is quite straightforward to show that it is stable for a range of parameters that increases with the magnitude of the interaction B.

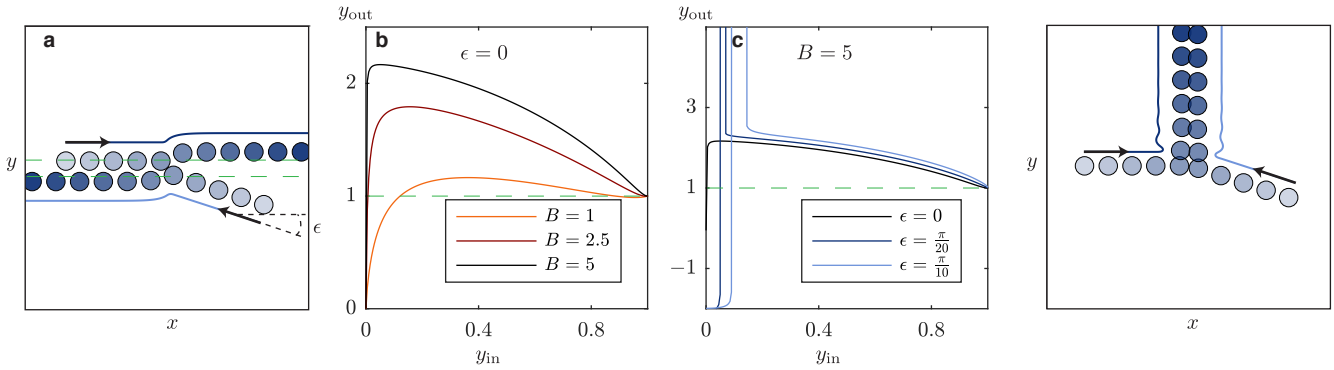

Figure 1.11 | Persistent transverse scattering. (a)Typical scattering trajectory for two particles targeting opposite directions ($B = 5$, $\epsilon = \frac{\pi}{10}$ and $y_{\rm in} = 0.75$). The initial and final vertical positions $y_{\rm in}$ and $y_{\rm out}$ are defined in the main text, Fig. 3a. ϵ is the incoming deviation of the left mover. (b) Final vertical position $y_{\rm out}$ as a function of the initial vertical position $y_{\rm in}$ for a left and a right mover experiencing a frontal collision ($\epsilon = 0$) at different values of the repulsion magnitude B. The transverse scattering is always different from the expected value for hard-core collisions (green line), and grows with the repulsion magnitude. (c) Final vertical position $y_{\rm out}$ as a function of the initial vertical position $y_{\rm in}$ at a high repulsion magnitude $B = 5$ for different impact angles ϵ. At a sufficiently high impact angle, the particles can stick to each other and travel upwards or downwards, as pictured in (d). (d) Two particles travelling upwards together ($B = 5$, $\epsilon = \frac{\pi}{10}$ and $y_{\rm in} = 0.125$)

Supplementary Note 3: Linearized hydrodynamics in the dilute limit

The hydrodynamic equation for the velocity field, Eq. (1.17) in the main text is closed assuming wrapped Gaussian angular fluctuations. This equation admits a constant and homogeneous solution defined by: $\rho_\alpha = \rho_\beta = \rho_0$ and $\mathbf{v}_\alpha = v_0\hat{\mathbf{h}}_\alpha = -\mathbf{v}_\beta$, with the condition $4\mathcal{D}\rho_0 v_0 = (1 - v_0^4)$. In the long wavelength limit, the linear perturbations to this solution $\rho_\alpha = (\rho_0 + \delta\rho_\alpha)$, and $\mathbf{v}_\alpha = (v_0\hat{\mathbf{h}}_\alpha + \delta\mathbf{v}_\alpha)$ obey:

$$\partial_{\rm t}\delta\rho_\alpha(\mathbf{r},t) + v_0(\hat{\mathbf{h}}_\alpha\cdot\boldsymbol{\nabla})\delta\rho_\alpha + \rho_0\boldsymbol{\nabla}\cdot\delta\mathbf{v}_\alpha = 0, \tag{1.20}$$

and

$$\mathbf{W}_\alpha\cdot\delta\mathbf{v}_\alpha = -\left[\mathbf{A}\cdot\boldsymbol{\nabla}\delta\rho_\alpha + \left(\frac{\rho_0\mathcal{B}}{2}\boldsymbol{\nabla} + \mathcal{D}\rho_0 v_0\hat{\mathbf{h}}_\alpha\right)\delta\bar{\rho}\right] \tag{1.21}$$

where we have ignored the fast relaxation of the velocity field and discarded its time derivatives. The hydrodynamic coefficients are defined by: $\mathbf{W}_\alpha = [v_0\mathbf{M}_\alpha + \rho_0(\mathbf{H} + \bar{\rho}_0\mathcal{D}\mathbf{I})]$, $\mathcal{B} = a\mathcal{D}$, and

$$\mathbf{M}_\alpha = \rho_0 v_\alpha^3\begin{pmatrix} 2\partial_{\rm x} & \partial_{\rm y} \\ -2\partial_{\rm y} & \partial_{\rm x}\end{pmatrix},\ \mathbf{H} = v_0^3\begin{pmatrix} 2 & 0 \\ 0 & 1\end{pmatrix} \text{ and } \mathbf{A} = \frac{1}{2}\begin{pmatrix} 1+v_0^4 & 0 \\ 0 & 1-v_0^4\end{pmatrix}. \tag{1.22}$$

Eliminating the velocity field from the linearized equations, we find that the large-scale density fluctuations evolve according to:

$$\partial_{\rm t}\delta\rho_\alpha(\mathbf{r},t) + \boldsymbol{\nabla}\cdot(\mathbf{J}_\alpha + \tilde{\mathbf{J}}) = 0, \tag{1.23}$$

where the two currents are given by:

$$\mathbf{J}_\alpha = \left(v_0\hat{\mathbf{h}}_\alpha - \rho_0(\mathbf{W}_\alpha^{-1}\cdot\mathbf{A})\cdot\boldsymbol{\nabla}\right)\delta\rho_\alpha \tag{1.24}$$

$$\tilde{\mathbf{J}} = -\rho_0\mathbf{W}_\alpha^{-1}\cdot\left(\mathcal{D}\rho_0 v_0\hat{\mathbf{h}}_\alpha + \frac{\rho_0\mathcal{B}}{2}\boldsymbol{\nabla}\right)\delta\overline{\rho}. \tag{1.25}$$

The matrix $\mathbf{W}_\alpha$ is readily inverted going to Fourier space. Noting $\mathbf{q}$ the spatial wavevectors we recover the simple expressions provided in the main text:

$$\mathbf{J}_\alpha(\mathbf{q},t) = v_0\hat{\mathbf{h}}_\alpha\delta\rho_\alpha - (\mathbf{D}\cdot\mathbf{q})\delta\rho_\alpha, \tag{1.26}$$

$$\tilde{\mathbf{J}}(\mathbf{q},t) = -\tilde{v}\hat{\mathbf{h}}_\alpha\delta\overline{\rho} - (\tilde{\mathbf{D}}\cdot\mathbf{q})\delta\overline{\rho}, \tag{1.27}$$

where the anisotropic diffusivity are diagonal

$$\mathbf{D} = \frac{1}{2}\begin{pmatrix} \frac{1+v_0^4}{\Delta_\mathrm{x}} & 0 \\ 0 & \frac{1-v_0^4}{\Delta_\mathrm{y}} \end{pmatrix},\ \tilde{\mathbf{D}} = \frac{1}{2}\begin{pmatrix} \frac{\rho_0\mathcal{B}}{2\Delta_\mathrm{x}} - \frac{2\mathcal{D}\rho_0 v_0^4}{\Delta_\mathrm{x}^2} & 0 \\ 0 & \frac{\rho_0\mathcal{B}}{2\Delta_\mathrm{y}} + \frac{2\mathcal{D}\rho_0 v_0^4}{\Delta_\mathrm{x}\Delta_\mathrm{y}} \end{pmatrix} \tag{1.28}$$

with $\Delta_\mathrm{x} = 2v_0^3 + 2\mathcal{D}\rho_0$ and $\Delta_\mathrm{y} = v_0^3 + 2\mathcal{D}\rho_0$ and $\tilde{v} = \frac{\mathcal{D}\rho_0}{\Delta_\mathrm{x}}v_0$.

Supplementary Note 4: Long-range density correlations

The structural correlations are found adding a conserved δ-correlated noise $\boldsymbol{\xi}_\alpha$ to Supplementary Equation (1.23):

$$(i\omega\mathbb{I} + \mathbf{R}).\begin{pmatrix}\delta\rho_\alpha\\ \delta\rho_\beta\end{pmatrix} = -\begin{pmatrix} i\mathbf{q}\cdot\boldsymbol{\xi}_\alpha \\ i\mathbf{q}\cdot\boldsymbol{\xi}_\beta\end{pmatrix}, \tag{1.29}$$

where the linear response matrix $\mathbf{R}$ takes the rather compact form

$$\mathbf{R} = \begin{pmatrix} iq_\mathrm{x}(v_\alpha - \tilde{v}_\alpha) + (D_\mathrm{x}+\tilde{D}_\mathrm{x})q_\mathrm{x}^2 + (D_\mathrm{y}+\tilde{D}_\mathrm{y})q_\mathrm{y}^2 & -iq_\mathrm{x}\tilde{v}_\alpha + \tilde{D}_\mathrm{x}q_\mathrm{x}^2 + \tilde{D}_\mathrm{y}q_\mathrm{y}^2 \\ iq_\mathrm{x}\tilde{v}_\alpha + \tilde{D}_\mathrm{x}q_\mathrm{x}^2 + \tilde{D}_\mathrm{y}q_\mathrm{y}^2 & -iq_\mathrm{x}(v_\alpha - \tilde{v}_\alpha) + (D_\mathrm{x}+\tilde{D}_\mathrm{x})q_\mathrm{x}^2 + (D_\mathrm{y}+\tilde{D}_\mathrm{y})q_\mathrm{y}^2 \end{pmatrix} \tag{1.30}$$

when defining the hydrodynamics coefficients

$$\tilde{D}_\mathrm{x} = \frac{1}{2}\left(\frac{\rho_0\mathcal{B}}{2\Delta_\mathrm{x}} - \frac{2\mathcal{D}\rho_0 v_0^4}{\Delta_\mathrm{x}^2}\right) \quad ; \quad \tilde{D}_\mathrm{y} = \frac{1}{2}\left(\frac{\rho_0\mathcal{B}}{2\Delta_\mathrm{y}} + \frac{2\mathcal{D}\rho_0 v_0^4}{\Delta_\mathrm{x}\Delta_\mathrm{y}}\right)$$
$$D_\mathrm{x} = \frac{1}{2}\left(\frac{1+v_0^4}{\Delta_\mathrm{x}}\right) \quad ; \quad D_\mathrm{y} = \frac{1}{2}\left(\frac{1-v_0^4}{\Delta_\mathrm{y}}\right).$$

The density fluctuations are readily computed within this linear response framework.

$$\langle|\delta\rho_\alpha(\mathbf{q})|^2\rangle = C_0(\mathbf{q})\left(\frac{\left[q_\mathrm{x}^2(\tilde{D}_\mathrm{x}+D_\mathrm{x}) + q_\mathrm{y}^2(\tilde{D}_\mathrm{y}+D_\mathrm{y})\right]^2 + [q_\mathrm{x}(v_0-\tilde{v})]^2}{\left[q_\mathrm{x}^2D_\mathrm{x} + q_\mathrm{y}^2D_\mathrm{y}\right]\left[q_\mathrm{x}^2(2\tilde{D}_\mathrm{x}+D_\mathrm{x}) + q_\mathrm{y}^2(2\tilde{D}_\mathrm{y}+D_\mathrm{y})\right] + q_\mathrm{x}^2v_0(v_0-2\tilde{v})}\right) \tag{1.31}$$

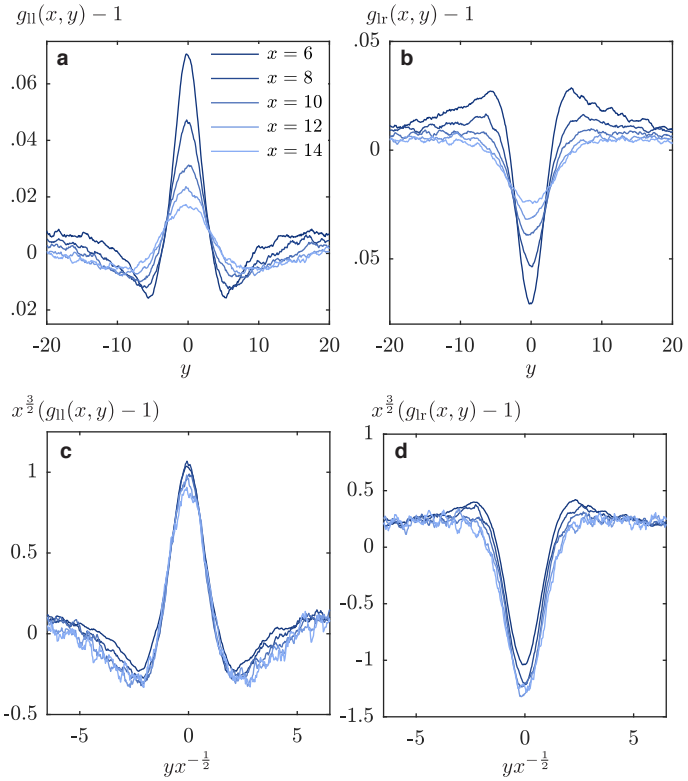

Figure 1.12 | Density correlation functions evaluated at a fixed values of x plotted versus the distance in the transverse direction y. Simulations performed deep in the homogeneous phase ($B = 5$ and $\pi\overline{\rho a^2} = 0.65$). (a) Bare pair correlation functions functions for particles of the same population $g_{\rm ll}(x,y)$ (left movers). (b) Bare pair correlation function for particles belonging to different populations $g_{\rm lr}(x,y)$. (c) and (d) Collapse of the pair correlations once rescaled by the universal $x^{-3/2}$ power law and plotted as a function of the rescaled distance $y/\sqrt{x}$. The good collapse of the rescaled curves supports the validity of the scaling deduced from the linearized fluctuating hydrodynamics.

and

$$\langle \delta\rho_\alpha(\mathbf{q})\delta\rho_\beta(-\mathbf{q})\rangle = C_0(\mathbf{q})\left(\frac{\left[q_{\rm x}^2\tilde{D}_{\rm x}+q_{\rm y}^2\tilde{D}_{\rm y}-iq_{\rm x}\tilde{v}_\alpha\right]\left[q_{\rm x}^2(\tilde{D}_{\rm x}+D_{\rm x})+q_{\rm y}^2(\tilde{D}_{\rm y}+D_{\rm y})-iq_{\rm x}(v_\alpha-\tilde{v}_\alpha)\right]}{\left[q_{\rm x}^2D_{\rm x}+q_{\rm y}^2D_{\rm y}\right]\left[q_{\rm x}^2(2\tilde{D}_{\rm x}+D_{\rm x})+q_{\rm y}^2(2\tilde{D}_{\rm y}+D_{\rm y})\right]+q_{\rm x}^2v_0(v_0-2\tilde{v})}\right) \tag{1.32}$$

with

$$C_0(\mathbf{q}) = \frac{q^2T}{q_{\rm x}^2(\tilde{D}_{\rm x}+D_{\rm x})+q_{\rm y}^2(\tilde{D}_{\rm y}+D_{\rm y})} \tag{1.33}$$

where, for simplicity and with no loss of generality, the added noise is chosen to be isotropic. An anisotropy would simply write $q_{\rm x}^2T_{\rm x}+q_{\rm y}^2T_{\rm y}$ and not change any of the results. One can readily recognize in the prefactor $C_0(\mathbf{q})$ the density autocorrelation function of an out-of-equilibrium anisotropic system with conserved dynamics and noise, as described in [36].

As we are interested in the long distance behavior of the density autocorrelation functions i.e. the limit $\mathbf{q} \to \mathbf{0}$, we focus on the simpler form they take at lowest order in q_x and q_y:

$$\langle |\delta\rho_\alpha(\mathbf{q})|^2 \rangle = C_0(\mathbf{q}) \left(\frac{q_\mathrm{y}^4 (\tilde{D}_\mathrm{y} + D_\mathrm{y})^2 + q_\mathrm{x}^2 (v_0 - \tilde{v})^2}{q_\mathrm{y}^4 D_\mathrm{y} (2\tilde{D}_\mathrm{y} + D_\mathrm{y}) + q_\mathrm{x}^2 v_0 (v_0 - 2\tilde{v})} \right) \tag{1.34}$$

$$\langle \delta\rho_\alpha(\mathbf{q}) \delta\rho_\beta(-\mathbf{q}) \rangle = C_0(\mathbf{q}) \left(\frac{\left[q_\mathrm{y}^2 \tilde{D}_\mathrm{y} - i q_\mathrm{x} \tilde{v}_\alpha \right] \left[q_\mathrm{y}^2 (\tilde{D}_\mathrm{y} + D_\mathrm{y}) - i q_\mathrm{x} (v_\alpha - \tilde{v}_\alpha) \right]}{q_\mathrm{y}^4 D_\mathrm{y} (2\tilde{D}_\mathrm{y} + D_\mathrm{y}) + q_\mathrm{x}^2 v_0 (v_0 - 2\tilde{v})} \right). \tag{1.35}$$

The long wavelength limit of these nonanalytic correlations is not uniquely defined as already pointed out in [76]. We therefore have to specify the way we take this limit. If we keep both wave vectors q_x and q_y of the same order as they go to zero, we obtain $\langle |\delta\rho_\alpha(\mathbf{q})|^2 \rangle \propto C_0(\mathbf{q})$, yielding an asymptotic behavior in real space $|g_{\alpha\beta}(x, 0) - 1| \sim x^{-2}$ [36], not consistent with our numerical findings. This is not surprising since in this given limit, all the specifities of our system, namely the interactions and the alignment field, are thrown out of the equations. However, the specific long-range limit $q_\mathrm{x} \sim q_\mathrm{y}^2$ simplifies the prefactor into $C_0(\mathbf{q}) \sim T/(\tilde{D}_\mathrm{y} + D_\mathrm{y})$ and preserves the main ingredients of our system. $\langle |\delta\rho_\alpha(\mathbf{q})|^2 \rangle$ then has the same analytic expression as that derived for oppositely driven colloids in [76] and the cross-correlation $\langle \delta\rho_\alpha(\mathbf{q}) \delta\rho_\beta(-\mathbf{q}) \rangle$ becomes a linear combination of the auto- and cross-correlation functions derived in [76]. They therefore both have the same asymptotic behavior in real space: $|g_{\alpha\beta}(x, 0) - 1| \sim x^{-3/2}$ which correctly accounts for our numerical findings as evidenced in Fig. 4b in the main text. In addition, Fourier transforming Supplementary Equations (1.34) and (1.35), we find that they are both homogeneous functions obeying $|1 - g_{\alpha\beta}(x \to \infty, y)| \sim x^{-\frac{3}{2}} \mathcal{C}(y x^{-1/2})$, again in agreement with our numerical simulations as shown in Supplementary Figure 1.12. This emphasizes the universality of the results obtained by linear perturbation of the kinetic theory.

Supplementary Note 5: Hydrodynamic theory in the large density limit

The hydrodynamic theory exploited in the previous sections was derived using a Boltzmann ansatz valid in the dilute limit. However the homogeneous mingled state also extends in the high density range. In order to further establish the robustness of the long-range structural correlation in this dynamical state, we here establish the hydrodynamic description of the interacting populations in the limit of very large densities. In order to do so we use a mean-field approach. We first write the continuity equation for the $2N$-point distribution function $\psi^{(2N)}(\mathbf{r}_{\alpha 1}, ..., \mathbf{r}_{\alpha N}, \theta_{\alpha 1}, ...\theta_{\alpha N}, \mathbf{r}_{\beta 1}, ..., \mathbf{r}_{\beta N}, \theta_{\beta 1}, ...\theta_{\beta N})$

$$\partial_\mathrm{t} \psi^{(2N)} + \sum_{i=\alpha,\beta} \boldsymbol{\nabla}_i . (\hat{\mathbf{p}}_i \psi^{(2N)}) + \sum_{i=\alpha,\beta} \partial_{\theta_i} \left(\dot{\theta}_i \psi^{(2N)} \right) = 0. \tag{1.36}$$

Integrating over all the particles but one, and using the equation of motion Supplementary Equation (1.19), we obtain a relation respectively between the one-point function, $\psi_\alpha(\mathbf{r}_\alpha, \theta_\alpha, t)$, and the two-point functions $\psi^{(2)}_{\alpha\alpha'}$ and $\psi^{(2)}_{\alpha\beta}$.

$$\partial_\mathrm{t} \psi_\alpha + \boldsymbol{\nabla} \cdot (\hat{\mathbf{p}} \psi_\alpha) + \partial_\theta \left[\partial_\theta \left(\hat{\mathbf{p}} \cdot \hat{\mathbf{h}}_\alpha \right) \psi_\alpha \right] = -\partial_\theta \left(\int d\mathbf{r}'_\alpha d\theta'_\alpha T_{\alpha\alpha'} \psi^{(2)}_{\alpha\alpha'} + \int d\mathbf{r}_\beta d\theta_\beta T_{\alpha\beta} \psi^{(2)}_{\alpha\beta} \right), \tag{1.37}$$

within a mean field hypothesis, a priori valid in the limit of infinite densities, we assume the factorization of the two-point functions:

$$\psi^{(2)}_{\alpha\beta} = \psi^{(1)}_{\alpha}\psi^{(1)}_{\beta}, \tag{1.38}$$

which yields

$$\partial_t\psi_\alpha + \boldsymbol{\nabla}\cdot(\hat{\mathbf{p}}\psi_\alpha) + \partial_\theta\left[\partial_\theta\left(\hat{\mathbf{p}}\cdot\hat{\mathbf{h}}_\alpha\right)\psi_\alpha\right] = -\partial_\theta\left(\psi_\alpha\left[\int d\mathbf{r}'_\alpha d\theta'_\alpha T_{\alpha\alpha'}\psi_{\alpha'} + \int d\mathbf{r}_\beta d\theta_\beta T_{\alpha\beta}\psi_\beta\right]\right). \tag{1.39}$$

Integrating this equation once with respect to θ yield the mass conservation equation. Multiplying Supplementary Equation (1.39) by $\hat{\mathbf{p}}$ before integrating over θ, we obtain a differential equation for the (non conserved) velocity field

$$\partial_t(\rho_\alpha\mathbf{v}_\alpha) + \boldsymbol{\nabla}\cdot\left[\rho_\alpha\left(\frac{\mathbb{I}}{2} + \mathbf{Q}_\alpha\right)\right] = \rho_\alpha\left(\frac{\mathbb{I}}{2} - \mathbf{Q}_\alpha\right)\cdot\left(\hat{\mathbf{h}}_\alpha - \mathcal{B}\boldsymbol{\nabla}\overline{\rho}\right) \tag{1.40}$$

where $\mathcal{B}$ is a hydrodynamic coefficient which increases with the magnitude of the repulsion between the motile particles. We shall note that Supplementary Equation (1.40) does not include any collision-induced diffusion term, unlike what was found in the dilute limit. This result is not surprising as collision-induced diffusivity arises from local density fluctuations that are discarded by our mean-field approximations. However, we can add a phenomenological angular diffusion to Supplementary Equation (1.40) on the basis of our numerical observations of the form $(\mathcal{D}\overline{\rho})\rho_\alpha\mathbf{v}_\alpha$ (see Supplementary Figure 1.10b). The resulting hydrodynamic equations have the very same form as Supplementary Equations (1.23) to (1.28). Not surprisingly, conducting the same fluctuating hydrodynamic analysis we find the same density correlations in the (stable) homogeneous state. Supplementary Equations (1.34) and (1.35) are merely modified by the expressions of the effective anisotropic diffusivities, not affecting the long range correlations in any way:

$$\tilde{D}_\mathrm{x} \to \frac{1}{2}\left(\rho_0\mathcal{B}\frac{1-v_0^4}{\Delta_\mathrm{x}} - \frac{2\mathcal{D}\rho_0 v_0^4}{\Delta_\mathrm{x}^2}\right) \text{ and } \tilde{D}_\mathrm{y} \to \frac{1}{2}\left(\rho_0\mathcal{B}\frac{1+v_0^4}{\Delta_\mathrm{y}} + \frac{2\mathcal{D}\rho_0 v_0^4}{\Delta_\mathrm{x}\Delta_\mathrm{y}}\right). \tag{1.41}$$

Part 2

Experimental study of unidirectionally polarized crowds

1 A model experiment

Crowd safety is the major motivation behind the study of pedestrian dynamics. Hazardous situations, such as flow through a constriction (Fig. 2.1a) or extreme density scenarios (Fig. 2.1b), have therefore focused most of the research community's efforts. With no prior knowledge of human flow dynamics, however, the complexity of these setups makes their study difficult. To draw a parallel between human flows and fluid dynamics, it would be even more difficult to understand turbulence with no knowledge of the Navier-Stokes equations. Likewise, investigating local interaction rules is comparable to investigating molecular dynamics. It is insightful at small scales, but long-winded to upscale to complex large-scale phenomena.

To better understand human flow dynamics, we investigated the equivalent of a fluid at rest, its response to linear perturbations and the subsequent laminar flows. We found this behaviour in the starting corrals of road races (Fig. 2.1c). In this setup, common to most large-scale races, thousands of participants are queuing in a unidirectional corridor. They are separated into several waves, depending on their expected running time, and walk towards the starting line under the race staff's guidance (see Fig. 2.1c). This experiment has the advantages of being predictable, large scale, and geometrically simple.

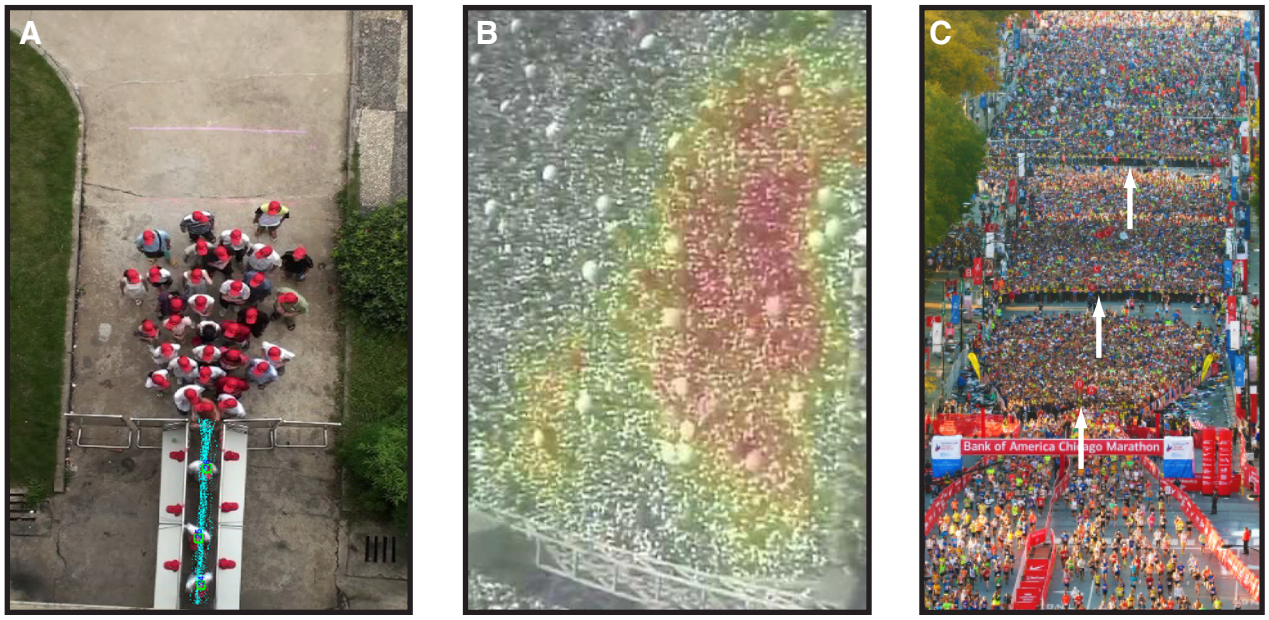

Figure 2.1 | Different experimental setups. (A) Controlled experiment, with traceble participants, to investigate crowd behaviour at a narrowing. Adapted from [90]. (B) Large field experiment at the 2006 Hajj. The number of participants is very large, but the underlying dynamics are complex. Adapted from [43]. (C) Image of the starting area of the 2017 Chicago Marathon, taken from an elevated observation point. The participants are confined in a unidirectional road and are separated into different waves by lines of race staff (indicated by the white arrows).

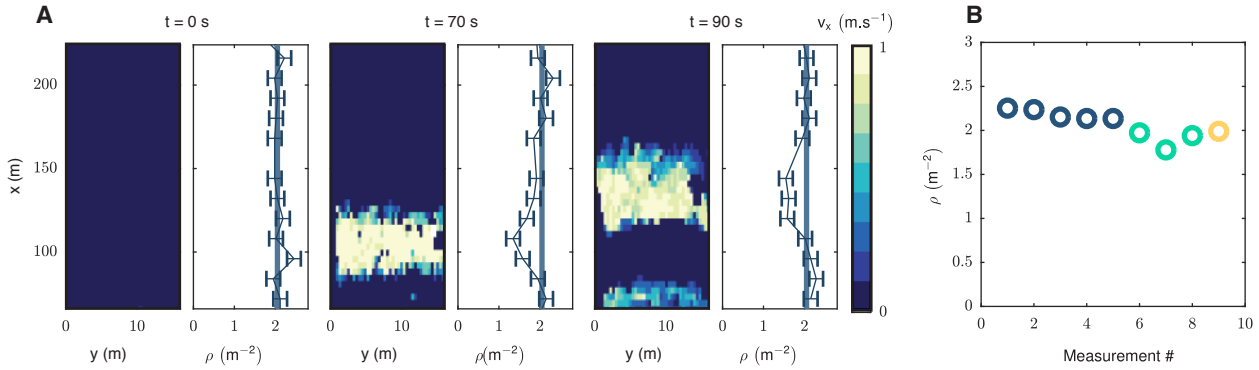

Figure 2.2 | Density measurements in queuing crowds. (A) Velocity and density fields at three successive times. At $t = 0\,\mathrm{s}$ the crowd is static and has a uniform density $\rho_0 \sim 2\,\mathrm{m}^{-2}$ (blue lines). At $t > 0$, as the staff members displaces the downstream boundary of the queuing crowd, a hybrid wave packet coupling velocity and density fluctuations propagates upstream. (B) For all events in which the density estimation was possible, the density in static crowds is roughly the same and equal to $\rho_0 = 2.2 \pm 0.05\,\mathrm{m}^{-2}$. The color code for each race is provided in Fig. 2.3c

2 Specificities of queuing crowds

Even in this simple setup, however, human crowds do not behave like a simple continuous medium. The ability of crowds to deform and flow through constrictions suggests a fluid description over a solid one. Their high compressibility rules out a incompressible liquid description, yet crowds do not behave like a gas: they do not occupy all available space.

To elucidate the specificities of queuing crowds we performed quantitative measurements on the starting corrals of four different road races: the 2016 and 2017 Bank of America Chicago Marathons, the 2017 Schneider Electric Paris Marathon, and the 2017 ATC Peachtree Road Race. Manually counting the participants, we found the density of static crowds to be independent of the distance from the starting line (Fig. 2.2a). Consequently, the will of the participants to take the start cannot be modeled as a constant force field, which for compressible fluids at rest would result in a density gradient. In addition we found this static density to be roughly 2 people per square meter in all the studied events (Fig. 2.2b)

Counting pedestrians is cumbersome. We therefore did not address the dynamics of the density field in greater details. We instead focused on the velocity field, which we measured by a conventional PIV analysis. Unlike regular fluids, human crowds do not conserve momentum. They constantly exchange it with the ground, and can change their mean velocity at will. As a result, velocity is not expected to be a hydrodynamic variable. In our experimental setup, however, coupled density-velocity waves propagate over system-spanning scales (Figs. 2.2c and 2.3a). These waves are triggered by the race-staff's incremental progress towards the starting line, closely reproduced by the following queuing crowd (Fig. 2.1c). Qualitatively, any velocity profile imposed by the race staff propagates upstream through the whole crowd without deforming (Fig. 2.3b). In other words, these waves are linear and non dispersive. More quantitatively, a spectral analysis evidences that the velocity fluctuations are underdamped (Fig. 2.3c), suggesting that the velocity would be a soft, or hydrodynamic, mode despite the lack of associated conversation laws. We resolve this apparent paradox building a hydrodynamic theory of pedestrian flows.

More details about the image acquisition and correction techniques, the measurement of the density and velocity fields, and about the spectral analysis are provided in the Methods 4.

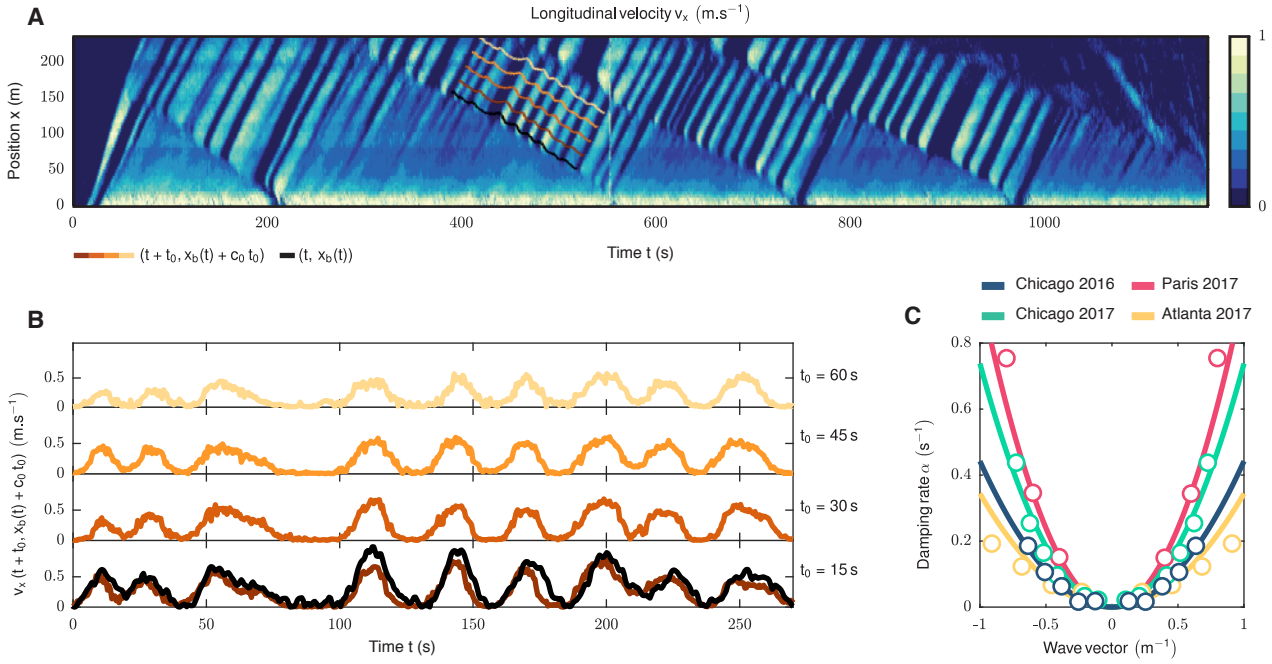

Figure 2.3 | Underdamped propagation of linear and non dispersive velocity waves. (A) Kymograph of the longitudinal velocity, averaged over the transverse direction (Chicago 2016). The position x indicates the distance from the starting line. A number of velocity waves are seen to propagate upstream at the same speed. (B) Black line: velocity of a chain of race-staff members $\dot{x}_b(t)$, measured by direct tracking. The corresponding positions $x_b(t)$ are reported as a black line on the kymograph in (A). As illustrated with the same color code on the the kymograph (A), the colored curves correspond to the longitudinal velocity field measured along the curves defined by the race staff position $x_b(t)$ after four different waiting times t_0: $v_x(t + t_0, x_b(t) + c_0 t_0)$. Independently of the shape of the $\dot{x}_b(t)$ signal, the velocity waves faithfully propagate the information of the boundary speed $\dot{x}_b(t)$ over system spanning scales, at constant speed. (C) Damping rate of the speed waves plotted for all wave vectors along the direction of propagation $\theta = \pi/4$. Circles: experimental data. Solid lines: best quadratic fits.

3 Hydrodynamic theory

A theory of unidirectional human flows has to capture all experimental observations mentionned above: uniform density at rest, propagation of linear and non dispersive velocity-density waves, and the softness of the velocity field. To reach this goal we built a hydrodynamic theory on experimental observations, within an active matter framework. Similarly to active fluids, human crowds are composed of polar particles. Their dynamics can in principle be described by a density field $\rho(\mathbf{r},t)$, a velocity field $\mathbf{v}(\mathbf{r},t)$ and a polarization field $\mathbf{p}(\mathbf{r},t)$. We recall that only density is a conserved quantity,

$$\partial_t \rho + \boldsymbol{\nabla}\cdot(\rho\mathbf{v}) = 0. \tag{2.1}$$

Linear and angular momentum are constantly exchanged with the ground, in a way we a priori do not know. We can generically express the rate of momentum change as

$$\partial_{\mathrm{t}}(\rho\mathbf{v}) + (\mathbf{v}\cdot\boldsymbol{\nabla})(\rho\mathbf{v}) = \boldsymbol{\nabla}\cdot\boldsymbol{\sigma} + \boldsymbol{\mathcal{F}}_v\left(\{\rho\},\{\mathbf{v}\},\{\mathbf{p}\}\right), \tag{2.2}$$

where $\boldsymbol{\sigma}$ is the stress tensor and $\boldsymbol{\mathcal{F}}_v$ the force exerted by the road on the crowd. This force is in principle a functional of the density, the velocity and the polarization fields. Similarly, we can express the rate of polarization change in a general form:

$$\partial_{\mathrm{t}}\mathbf{p} + (\mathbf{v}\cdot\boldsymbol{\nabla})\mathbf{p} + \boldsymbol{\Omega}\cdot\mathbf{p} = \boldsymbol{\mathcal{F}}_p\left(\{\rho\},\{\mathbf{v}\},\{\mathbf{p}\}\right). \tag{2.3}$$

The left-hand side of Eq. (2.3) is a kinematic term commonly referred to as the corotational derivative ($\boldsymbol{\Omega}$ is the vorticity tensor defined by: $\Omega_{ij} = \frac{1}{2}(\partial_i v_j - \partial_j v_i)$) [29] and $\boldsymbol{\mathcal{F}}_p$ conveys the change of orientation due to external forcings. The two equations governing the rate of linear and angular momentum change Eqs. (2.2) and (2.3) are very generic, and we can anticipate the form of the external forcings $\boldsymbol{\mathcal{F}}_v$ and $\boldsymbol{\mathcal{F}}_p$ from two key observations. First, unlike flocking systems, queuing crowds do not exhibit orientational symmetry. Instead, pedestrians spontaneously align with the direction of the road. Consequently, the polarization field is not a soft mode and we can express the associated forcing as the response to an external magnetic field

$$\boldsymbol{\mathcal{F}}_p = -\alpha_\perp \mathbf{p} + h\hat{\mathbf{x}} + \mathcal{O}(\boldsymbol{\nabla}). \tag{2.4}$$

Second, pedestrians rarely walk sideways but rather in the direction they are facing. In other words, the orientation of the velocity field quickly relaxes towards the one of the polarization field. This feature is very well captured by an external force of the form

$$\boldsymbol{\mathcal{F}}_v = -\boldsymbol{\Gamma}\cdot[\mathbf{v} - \nu_0(\rho)\mathbf{p}] + \mathcal{O}(\boldsymbol{\nabla}), \tag{2.5}$$

where ν_0 quantifies the strength of the self-propulsive force in the direction of the polarization and $\boldsymbol{\Gamma} \equiv \Gamma_\parallel \mathbf{pp} + \Gamma_\perp(\mathbb{I} - \mathbf{pp})$ is an anisotropic friction coefficient. If we set the transverse relaxation rate much larger than the longitudinal one $\Gamma_\perp \gg \Gamma_\parallel$, at time scales longer than $\Gamma_\perp^{-1}$ the velocity field is aligned with the polarization, and the speed flow relaxes in a finite time $\Gamma_\parallel^{-1}$ towards the amplitude $\nu_0(\rho)$. For time scales larger than the longitudinal relaxation time $\Gamma_\parallel^{-1}$ we recover the so-called fundamental relation $v = \nu_0(\rho)$.

From the expression of the forces at zeroth order in gradient Eqs (2.4) and (2.5), we can fully characterize the stationnary state corresponding to quiescent queuing crowds: they have zero velocity, are fully

polarized in the direction of the road and exhibit a uniform density, set by the so-called fundamental relation $\nu_0(\rho_0) = 0$. These features are in agreement with our experimental observations, where we found the density of queuing static crowds to be roughly the same in each experimental setup (Fig. 2.2b) and all participants face the starting line (Fig. 2.1c).

We now focus on small density, velocity and polarization perturbations around this static state: respectively $\rho = \rho_0 + \delta\rho$, $\mathbf{v} = \delta\mathbf{v}$ and $\mathbf{p} = \hat{\mathbf{x}} + \delta\mathbf{p}$. Before we linearize the full set of equations, Eqs (2.1) to (2.5), one comment is in order. As mentionned above, the participants in the starting corrals face the starting line and do not walk sideways. We therefore constrain the polarization field to be a unit vector and the velocity field to be aligned with it: $\mathbf{p} = (\cos\psi, \sin\psi)$ and $\mathbf{v} = (v\cos\psi, v\sin\psi)$. The crowd orientation ψ and the flow speed v are both zero in the static state, and otherwise define the linear perturbations of the polarization and velocity fields: $\delta\mathbf{p} = \psi\hat{\mathbf{y}}$ and $\delta\mathbf{v} = v\,\hat{\mathbf{x}}$. We note that the velocity field is now purely longitudinal, consistently with out experimental finding $v_x \gg v_y$ (Fig. 2.4a). We take advantage of these simplifications to linearize the conservation equations Eq. (2.1), (2.2) and (2.3). First, linearized mass conservation Eq. (2.1) reduces to

$$\partial_t\delta\rho + \rho_0\partial_x v = 0. \tag{2.6}$$

Second, we obtain the linearized form of the rate of momentum change Eq. (2.2) by phenomenologically including all the terms allowed by symetry in the external force $\boldsymbol{\mathcal{F}}_v$. After projection on the longitudinal direction, we obtain the rate of flow speed change

$$\rho_0\partial_t v = -\Gamma_\parallel\left[v - \nu_0'(\rho_0)\delta\rho\right] + (-\beta\partial_x\delta\rho + c_x\partial_x v) + \gamma_o\partial_y\psi + \mathcal{O}(\nabla^2). \tag{2.7}$$

The first term on the right hand side is the linearized force term, and $\nu_0'(\rho_0) \equiv \partial_\rho\nu_0(\rho_0)$. The second term on the right hand side originates from the anisotropic pressure tensor with a compressibility depending on the magnitude of the flow speed and density. The third term describes flows caused by gradients in the orientation of the pedestrians. Third, we obtain the rate of orientation change by applying the same method to Eqs (2.2) and (2.4) and projecting on the transverse direction

$$\partial_t\psi = -\alpha_\perp\psi + A_\psi\partial_x\psi + A_\rho\partial_y\delta\rho + A_v\partial_y v + \mathcal{O}(\nabla^2). \tag{2.8}$$

Consistently with our spectral analysis, the orientation of the crowd relaxes towards the direction of the road in a finite time $\alpha_\perp^{-1}$ (Fig. 2.4b). At time scales larger than $\alpha_\perp^{-1}$, we can consider the orientational fluctuations to be of order one in gradient $\psi = \mathcal{O}(\nabla)$. In this limit, the contribution of orientational fluctuations to the rate of momentum change Eq. (2.7) is of second order in gradient. Consequently, at long time and length scales, the speed flow is slaved to the density fluctuations:

$$v = \nu_0'(\rho_0)\delta\rho - \beta\partial_x\delta\rho + \mathcal{O}(\nabla^2). \tag{2.9}$$

By injecting this dependence into the linearized mass equation Eq (2.6), we show that both the speed flow and the density fluctuations follow a transport-diffusion equation

$$\partial_t v - c_0\partial_x v + D_x\partial_x^2 v = 0, \tag{2.10}$$

where the diffusivity $D_x = (\rho_0\beta/\Gamma_\parallel)$ is given by the crowd compressibility, and the transport speed $c_0 = -\rho_0\nu_0'(\rho_0)$ is set by the slope of the so-called fundamental diagram at density ρ_0. The sign of this slope dictates in which direction density and velocity fluctuations propagate. In the oberved

queuing crowds, coupled velocity and density waves consistently propagate upstream, implying the so-called fundamental diagram to have a negative slope at ρ_0. This feature is intuitive: from the static state participants only start walking when the density is reduced. Additionally, it is supported by the velocity-density relation Eq. (2.9) and the sign difference we observe between density and velocity fluctuations (Fig. 2.2c.). The final hydrodynamic equation Eq. (2.10) explains the softness of the velocity mode: velocity is slaved to the only conserved quantity, the density field.

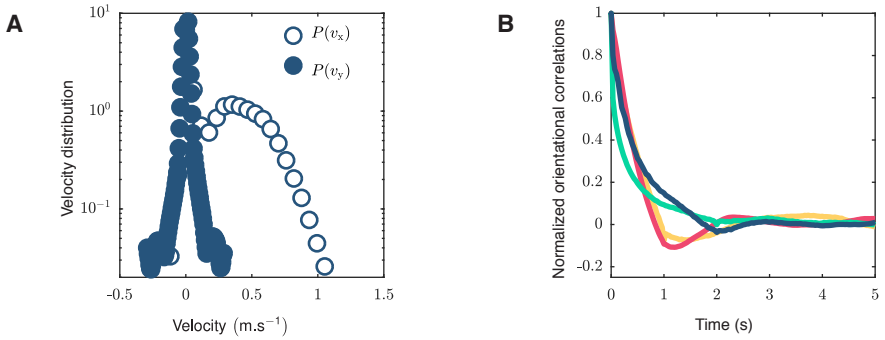

Figure 2.4 | (A) Probability distribution function of the longitudinal and transverse components of the velocity field (Chicago 2016). The longitudinal component dominates. (B) Normalized orientational correlations plotted versus time for all experiments ($\theta = \pi/4$, $q = 0.5\,\mathrm{m}^{-1}$). Same color code as Fig 2.3c.

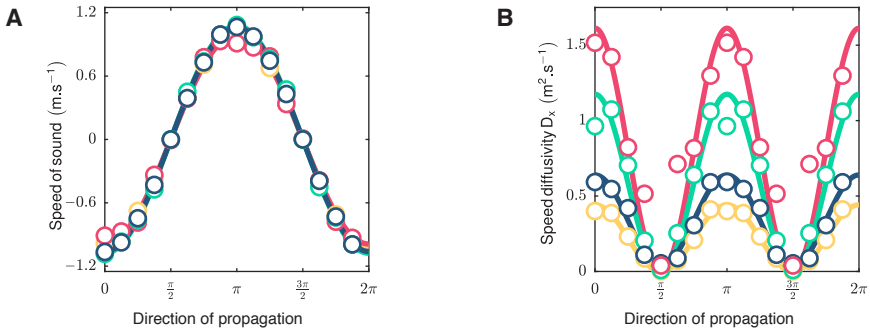

Figure 2.5 | Meassurements of the hydrodynamic constants from spectral analysis (details are provided in Methods 4). (A) Variations of the speed of sound with the direction of the wave vector θ for all experiments. Circles: experimental data. Solid line: cosine fit. The excellent fit shows that the dispersion relation is given by $\omega = cq_x$. (B)Variations of the speed diffusivity D_x with the direction of propagation. Circles: experimental data. Solid lines: squared cosine fits. Same color code as Fig 2.3c.

The hydrodynamic description presented above is in perfect agreement with our experimental observations: queuing crowds at rest have their density set by the so-called fundamental relation, linear perturbations propagate upstream at a constant speed and the softness of the velocity fluctuations is explained by a fast relaxation towards the density. In addition, the theory presented above predicts propagating and overdamped orientational fluctuations, as well as diffusively damped propagation of flow speed fluctuations in the longitudinal direction. We recover both properties in the spectral analysis of all four studied events (Figs. 2.4b and 2.5), and measuring the speed of sound c_0 and the diffusivity D_x in one event is sufficient to quantitatively predict their value in any other. We therefore expect our model to be predictive for the behaviour of any other large-scale queuing crowd.

4 Discussion and perspectives

We identified three natural perspectives for this work. Firstly, the short-timescales dynamics of the velocity and polarization fluctuations. The quantitatively predictive power of the hydrodynamic equation Eq. (2.10) is by definition restricted to long time scales and large waves length, in which all fast dynamics are discarded. Investigating shorter time-scales would be a direct way to further validate or not our theoretical descriptions of queuing crowds. As mentionned in the Supplementary Information 4, this requires more quantitative data and is left for future work. Secondly, the non-linear dynamics of queuing crowds. In our experimental setup, only the linear modes were probed. Investigating non-linear perturbations, e.g., induced by faster (possibly running) boundary displacements, is critical to understand crowd dynamics in extreme conditions. At last, complex geometries. The geometry of our experimental setup is the simplest imaginable. Investigating more complex setups, such as the crowd's dynamics in the funnel (Fig. 2.1c), is essential to understand and forecast complex evacuation scenarii in large-scale events.

Methods

Method 1: Crowd description and image acquisition

All queuing crowds correspond to road-race participants waiting for the race start in corrals. They are guided towrds the starting line by chains of staff members. In total we filmed four events: the 2016 Bank of America Chicago Marathon, the 2017 Bank of America Chicago Marathon, the 2017 Schneider Electric Paris Marathon and the 2017 AJC Peachtree Road Race. For short we will refer to these events by the city name and year of occurrence, e.g., the 2016 Bank of America Chicago Marathon will be called Chicago 2016. Every event gathered more than $40,000$ participants, see Table 2.1.

Race	Number of participants
Chicago 2016	$44,000$
Chicago 2017	$44,000$
Paris 2017	$42,000$
Atlanta 2017	$55,000$

Table 2.1 | Number of runners participating to the four races.

We selected these events to observe large-scale crowds from elevated observation spots. For each event, we booked a hotel room overlooking the starting area of the race and filmed it with telephoto lenses (Sigma 150-600mm F5-6.3 DG OS HSM | S) mounted on Nikon D500 cameras. The frame rate for every movie is 30 fps and the resolution 3840 x 2160 pixels (4K movies). Images of the setup corresponding to the 2016 Bank of America Chicago Marathon are shown in Figs. 2.6a and b, and the specifics of the observation conditions are provided in Table 2.2

Race	Hotel	Floor number	Distance from the event
Chicago 2016	Fairmont Chicago Millennium Park	17	530 meters
Chicago 2017	Fairmont Chicago Millennium Park	19	530 meters
Paris 2017	Paris Marriott Champs Elysees Hotel	6	75 meters
Atlanta 2017	The Westin Buckhead Atlanta	15	210 meters

Table 2.2 | Specifics of the observation points for each event.

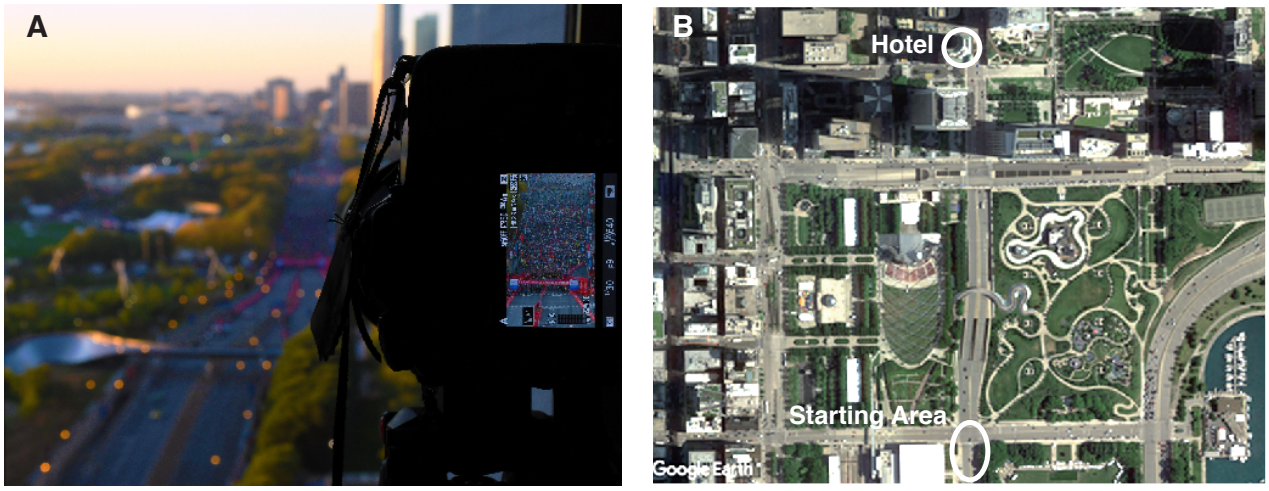

Figure 2.6 | (**A**) View of the queuing crowd from the observation point, with a Nikon D500 camera. (**B**) The locations of the starting line of the marathon, and of the observation points, are indicated on a Satellite image of the parks area in Chicago (Google Earth Pro).

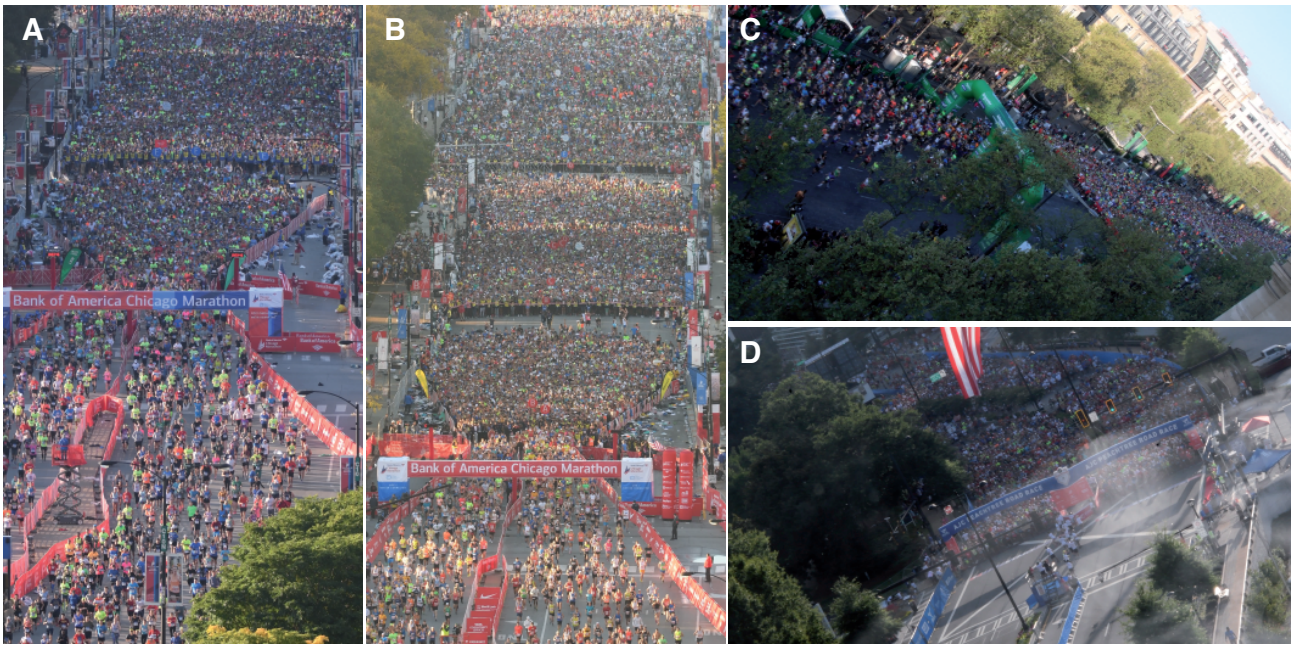

Figure 2.7 | Images captured from the observation points for the four experiments. (**A**) Chicago 2016. (**B**) Chicago 2017. (**C**) Paris 2017. (**D**) Atlanta 2017.

Method 2: Correction of perspective distortion

The raw images obtained with our experimental setup (Fig. 2.7) suffer from perspective distortions: every pixel on the image represents a different metric size. We correct for this effect using planar homography [38]. In the following, we describe this image correction technique using the images obtained for Chicago 2016 as a benchmark.

Planar homography

When we take a picture, we assign a pixel position to every visible point in the frame. If we call (X, Y, Z) (measured in meters) the coordinates of such a point in the reference frame of the road, it is mapped to (u, v) (measured in pixel units) in the reference frame of the camera sensor. We express this mapping as $(u, v) = F(X, Y, Z)$, where the function F depends both the optical transforms made by the camera and the change of reference frame. If we can invert this function, we can map every pixel from the original image to its real world coordinates, and obtain an image in which every pixel has the same size. Noting that our images were captured with a long focal length, we neglect the lens optical distortion and assume our camera can be modeled as a pinhole camera [37]. Given this assumption, the mapping takes the linear form [38]:

$$\begin{pmatrix} u \\ v \\ 1 \end{pmatrix} = \mathbf{C} \cdot \begin{pmatrix} X \\ Y \\ Z \\ 1 \end{pmatrix}, \tag{2.11}$$

where the so-called camera matrix $\mathbf{C}$ depends on the intrinsic parameters of the camera and on the precise location of the camera in space, none of which are necessarily known. To obtain real world coordinates from pixel coordinates, we need to invert Eq. (2.11). This is a priori impossible due to the 3×4 dimensionality of the camera matrix. If, however, we neglect the spatial extent of the real world scene in the z-direction, and assume that every point we see on the image belongs to the $Z = 0$ plane the mapping reduces to

$$\begin{pmatrix} u \\ v \\ 1 \end{pmatrix} = \mathbf{H} \cdot \begin{pmatrix} X \\ Y \\ 1 \end{pmatrix}, \tag{2.12}$$

where $\mathbf{H} = (h_{ij})$, usually called the homography matrix, is a priori invertible [19]. To obtain the real world coordinates (X, Y) of every pixel (u, v), we therefore need to estimate the 9 coefficients (h_{ij}). We do so by selecting a set of N points for which we know both pixel *and* real-world coordinates. Rewriting Eq. (2.12) in a the more convenient form

$$u = \frac{h_{11}X + h_{12}Y + h_{13}}{h_{31}X + h_{32}Y + h_{33}}, \; v = \frac{h_{21}X + h_{22}Y + h_{23}}{h_{31}X + h_{32}Y + h_{33}}, \tag{2.13}$$

we find that the homography coefficients (h_{ij}) are solutions of the system

$$\begin{pmatrix} X_1 & Y_1 & 1 & 0 & 0 & 0 & -u_1X_1 & -u_1Y_1 & -u_1 \\ 0 & 0 & 0 & X_1 & Y_1 & 1 & -v_1X_1 & -v_1Y_1 & -v_1 \\ . & . & . & . & . & . & . & . & . \\ . & . & . & . & . & . & . & . & . \\ X_N & Y_N & 1 & 0 & 0 & 0 & -u_NX_N & -u_NY_N & -u_N \\ 0 & 0 & 0 & X_N & Y_N & 1 & -v_NX_N & -v_NY_N & -v_N \end{pmatrix}_{(2N,9)} \cdot \begin{pmatrix} h_{11} \\ h_{12} \\ h_{13} \\ h_{21} \\ h_{22} \\ h_{23} \\ h_{31} \\ h_{32} \\ h_{33} \end{pmatrix}_{(9,1)} = \mathbf{0}_{(2N,1)}. \quad (2.14)$$

The homography vector $\mathbf{h}$, the vector on the l.h.s. of Eq. (2.14), belongs to the kernel of the $(\mathbf{A}^t \cdot \mathbf{A})$ matrix:

$$(\mathbf{A}^t \cdot \mathbf{A}) \cdot \mathbf{h} = \mathbf{0}, \quad (2.15)$$

where $\mathbf{A}$ is the $2N \times 9$ matrix on the left hand side of Eq. (2.14). To close this system, we note that multiplying $\mathbf{H}$ by any scalar leaves Eq. (2.13) unchanged, which has two consequences. Firstly, any eigenvector associated to the null eigenvalue of $(\mathbf{A}^t \cdot \mathbf{A})$ can be defined as the homography vector. Second, the homography matrix has $(9-1) = 8$ degrees of freedom. A set of 4 points, i.e. 8 equations, therefore suffices to determine all the homography coefficients.

Image-correction protocol

In practice we use the following procedure. We select a reference image in the marathon, clear of pedestrians, and choose a set of $N > 4$ points on the road distributed over the whole waiting area (Fig. 2.8b). We find their location on a satellite view (from Google Earth Pro) of the same area (Fig. 2.8a). We then collect their pixel coordinates both on the satellite view (X_i, Y_i) and on the raw image (u_i, v_i). We construct the matrix $(\mathbf{A}^t \cdot \mathbf{A})$ as defined in Eq. (2.14), numerically compute its eigenvalues and eigenvectors, and define the homography vector $\mathbf{h}$ as the unit eigenvector associated to the smallest eigenvalue. We then rescale all the raw images from this homography vector using the *projective2d* and *imwarp* MATLAB functions. As a result, all pixels on the rescaled images have the same size (Fig. 2.8c). Finally, we estimate the metric size of a pixel on the rescaled image (dx, dy) by measuring the distances between two sets of two selected points using the *ruler* tool of Google Earth Pro. The pixel sizes for all races are shown in Table 2.3 and the chosen points for the Chicago 2016 experiment, and the transformed reference images are shown in Fig. 2.8.

Race	dx (m)	dy (m)
Chicago 2016	0.123	0.013
Chicago 2017	0.159	0.016
Paris 2017	0.135	0.010
Atlanta 2017	0.051	0.013

Table 2.3 | Pixels sizes for each experiment.

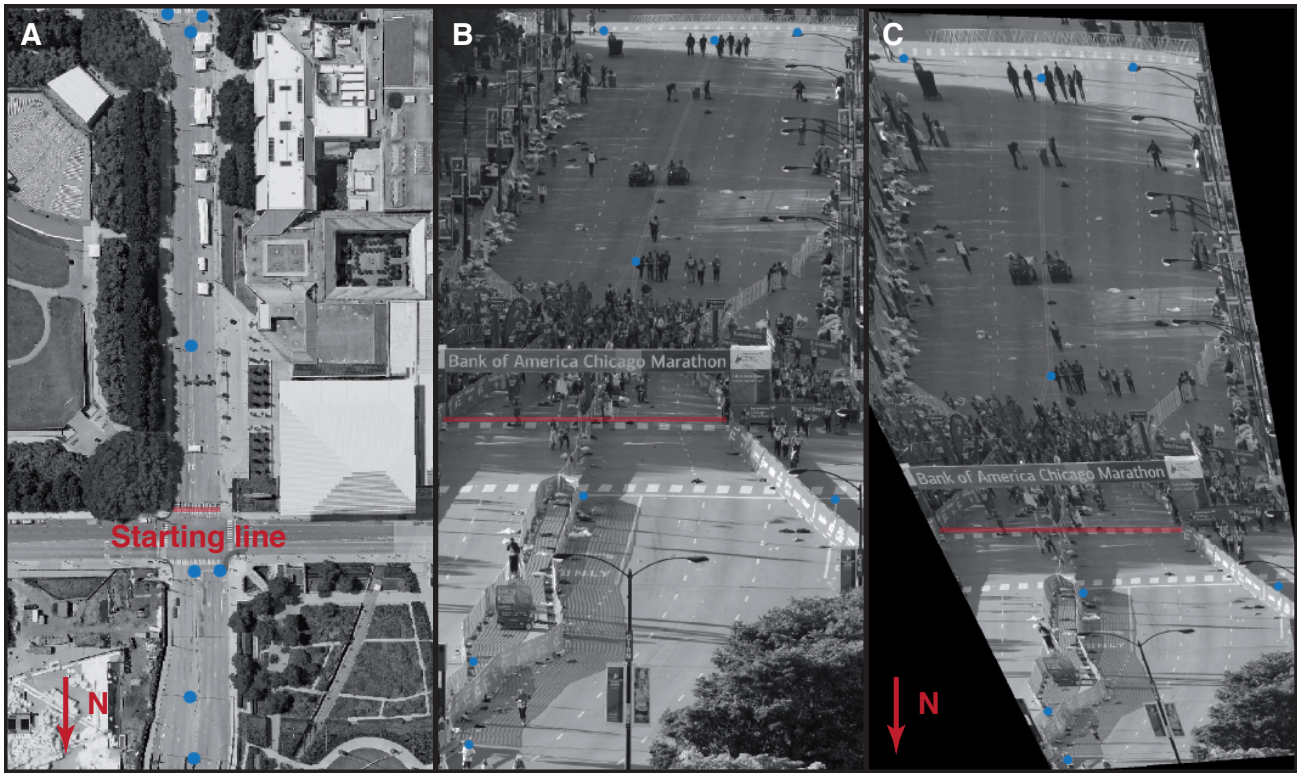

Figure 2.8 | Image calibration. The blue dots indicate the calibration points: (**A**) on a satellite image, (**B**) on the original picture, (**C**) on the rescaled picture. Red line: starting line. In (**A**) and (**C**) the red arrows point North.

Error on position measurements: imperfect homography

Although the rescaled calibration points seem to be at the right location (see Fig. 2.8b and c), the rescaling is not perfect. To estimate the relative error in the distance calculations due to the rescaling protocol, we calculate the distances between the original calibration points (Fig. 2.8a) and compare them to the distances between the *rescaled* calibration points (Fig. 2.8c). We found a maximal relative error in all races of about 5% in the direction of the flow and of about 10% in the direction transverse to the flow, see Table. 2.4.

Race	$\max(\epsilon_x)$	$\max(\epsilon_y)$
Chicago 2016	5%	10%
Chicago 2017	3%	9%
Paris 2017	4%	8%
Atlanta 2017	3%	5%

Table 2.4 | Position errors for all races. ϵ_x and ϵ_y are the relative distance errors in the x and y directions.

Error on position measurements: the zero-height approximation

To correct for perspective distortions we made the assumption that all visible pixels on the images were in the same plane as the road, which is true for the calibration points on the reference images (Fig. 2.8). When pedestrians are in the image, however, only their feet are on the road. The rest of their body is rescaled as if it was painted on the road (Fig. 2.9a). Here we estimate the consequences of this approximation on the accuracy of the absolute and relative position measurements.

Let us call h the height of an individual in the field of view, L its distance from the camera, and H the height of the observation spot. The length of the individual on the recorded image is $l = h\,L/(H-h)$. The people further from the camera appear larger on the image. This error, however does not translates into distance measurements. If we call Δx the distance between two people of same height and $\Delta x'$ the projection of this distance on the image (see Fig. 2.9), the scaling ratio $\Delta x'/\Delta x$ is independent of the distance from the camera

$$\Delta x' = \Delta x \left(1 + \frac{h}{H-h}\right). \tag{2.16}$$

The same relation holds for the projected distance between pedestrians on any direction of space. Consequently, every spatial quantity has to be scaled by a factor $(1 - h/H)$. We set the pedestrian height to $h = 1.75$ m and calculated the height of the observation point H from the floor number in Table. 2.2, assuming the floors were about 4 meters tall. We will discuss how Eq. (2.16) impacts the velocity measurements we conduct in the following sections.

Method 3: Measurement of the density field

We measured the density field manually. Despite the active development of people-detection algorithms in the computer vision community [103], to the best of our knowledge no algorithm can reliably and automatically count the number of people from the type of images we captured [103, 49]. A major difficulty lies in the occlusion of the pedestrians by each other. To circumvent this issue, we did not count the number of people on still images, but on animated GIFs of two second loops. Counts performed on still images only provide a lower bound of the real number of pedestrians on a given picture, but using the dynamics of the individuals makes it possible to detect more individuals than on the static images.

To estimate the density profile in queuing crowds, we manually counted the participants in a narrow band, starting at the entrance of the start funnel. The selected bands are 2.6 meters wide and 185 meters long, and each of them gathered approximately a thousand people. As the counting process is extremely time consuming, we only performed 3 of such measurements. In each of them, the density was found to be constant within static crowds and to locally decrease with increasing flow speed (main text Figure 1c).

Local measurements in $5.2 \times 12\,\mathrm{m}^2$ observation widows were performed in the Chicago 2016, Chicago 2017 and Atlanta 2017 events. All measurements correspond to more than a hundred runners in the middle of static queuing crowds. We were not capable to count pedestrians for the Paris 2017 event due to lower image quality. We found the static density to hardy fluctuate from one group of runners to another, and from one race to another. The average density is of the order of 2 people per squared meter, as summarized in Table 2.5.

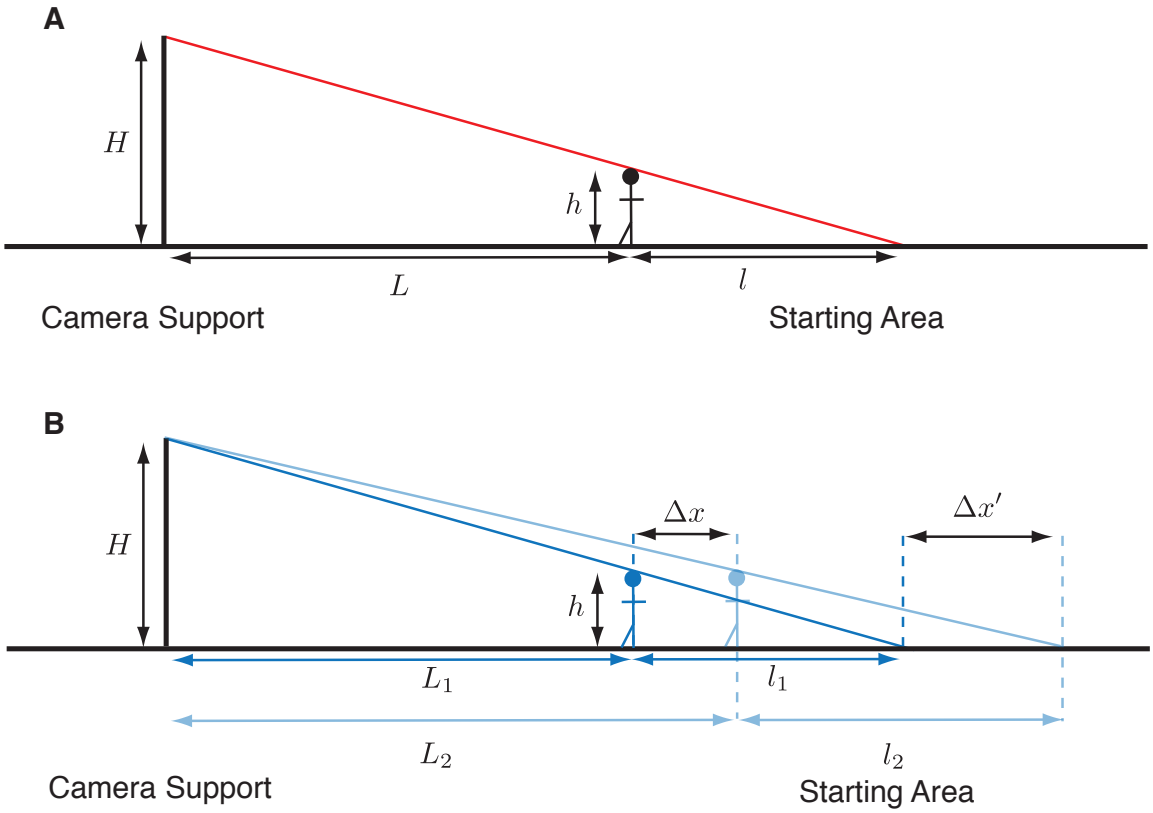

Figure 2.9 | Error estimation. (**A**) Error on position measurements. (**B**) Error on displacement measurements.

Race	# of measurements	ρ_0 (m^{-2})
Chicago 2016	5	2.2 ± 0.05
Chicago 2017	3	1.9 ± 0.1
Atlanta 2017	1	2

Table 2.5 | Density estimates in the static crowds. The errors are computed from the min and max values.

Method 4: Definition of the spatial and temporal windows

We restrained our study to a part of the velocity field $\mathbf{v}(\mathbf{r}, t)$, defined by spatial and temporal windows. In each race we chose a spatial window with a constant road section, to avoid constriction effects, and excluding occlusions from external elements. For instance, we removed the area hidden by trees in Paris 2017 and the area covered by traffic lights or by the flag of the United States of America in Atlanta 2017 (which took place on the Fourth of July). The areas kept for the study are shown in Fig. 2.10.

Similarly, we discarded the images corresponding to corrals empty of people, and to periods of time during which the crowds were at rest: either when the whole crowd stood still or, in 2017 Atlanta, during the filling of the corrals. These choices were made to reduce noise or the effect of undesired phenomena, e.g., lone staff members walking in any direction on an empty road. The considered temporal windows are shown in Fig. 2.11.

Method 5: Measurement of the velocity field

To measure the flow velocity, we do not detect and track individuals. Instead, as one would in conventional fluids, we study the crowd as a continuum media and use a Particle Image Velocimetry (PIV) toolbox to obtain a velocity *field*, see e.g. [4]. In this section we describe the basic principles of PIV, explain how we choose the different parameters and give the set of parameters we used in all our experiments.

Particle Image Velocimetry

Particle Image Velocimetry is an image correlation based technique to estimate the velocity field of a flowing liquid [1]. Usually the fluid is filmed after having been seeded with visible particles, which form spatial patterns on the images. If the size of the particles is carefully chosen, these patterns are transported by the fluid with almost no deformation. An image correlation algorithm is then used to identify the displacement of these patterns between two successive images, and multiplying these displacements by the frame rate gives the velocity field of the flow. In the case of queuing crowds, we do not need to add particles to the fluid: the features coming from the pedestrians themselves already form visible patterns on the images. We used the *PIVLab* toolbox, in which we modified the image correlation algorithm so that the correlation would be averaged over the three color channels of the camera.

In practice, we use the following procedure. We divide the image of the experimental setup into N boxes of $(L \times L)$ pixels of coordinates $(\mathbf{x}_1, \ldots, \mathbf{x}_N)$. Every image at a time t, $\mathcal{I}(t)$, is a snapshot of the same setup at a different time. The location of the boxes are constant in time, but the patterns in the boxes change as time goes on. At every time t, the image correlation algorithm estimates where the patterns defined by the N boxes on image $\mathcal{I}(t)$ are on image $\mathcal{I}(t + \Delta t)$, with Δt the PIV time step. This estimation gives N positions on image $\mathcal{I}(t + \Delta)$, $(\mathbf{x}'_1(t), \ldots, \mathbf{x}'_N(t))$, and the velocity field is calculated at every box location as $\mathbf{v}(\mathbf{x}_i, t) = (\mathbf{x}'_i(t) - \mathbf{x}_i)/\Delta t$.

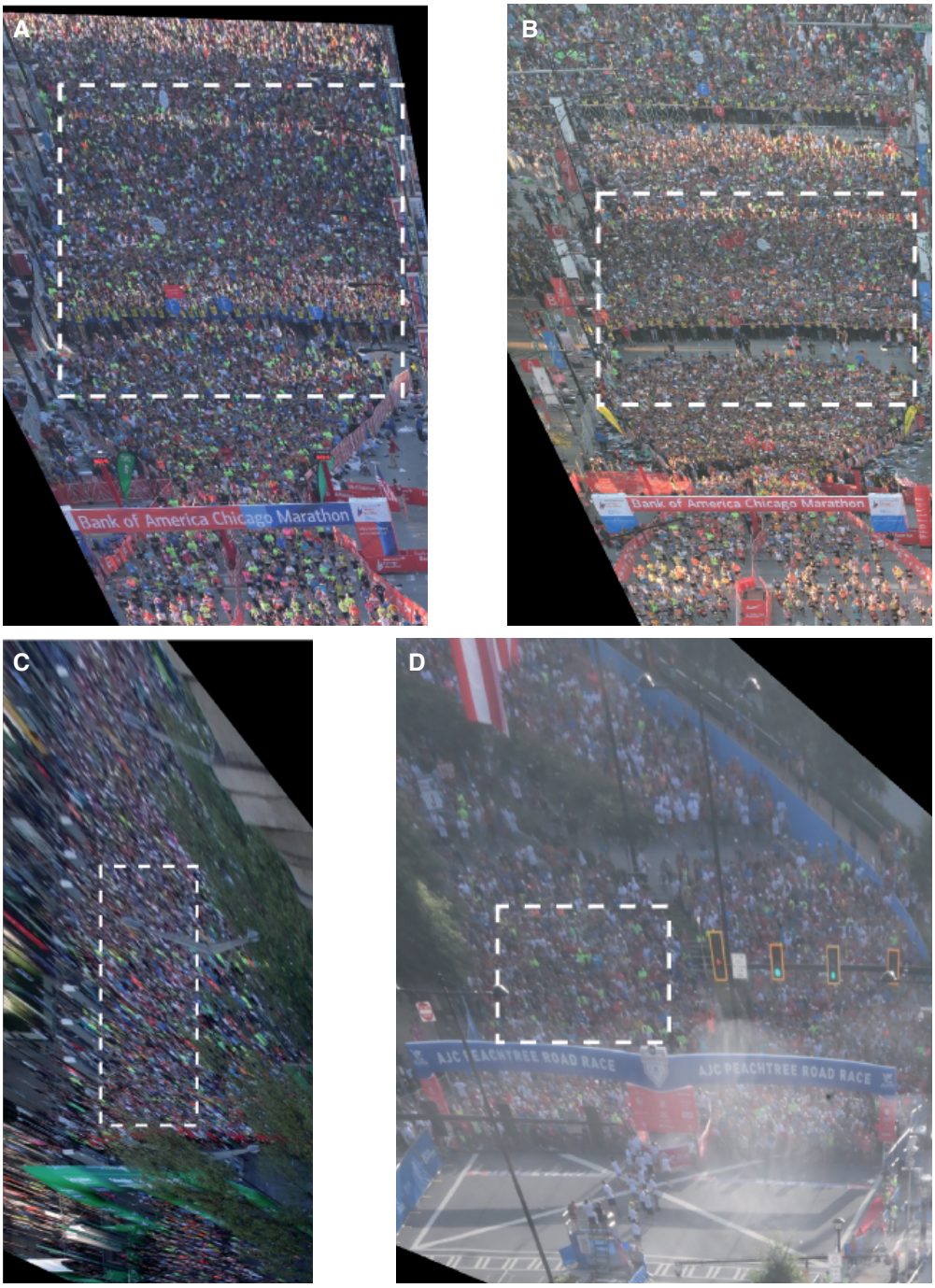

Figure 2.10 | Observation windows (white boxes) shown on the rescaled images for all experiments: (**A**) Chicago 2016. (**B**) Chicago 2017. (**C**) Paris 2017. (**D**) Atlanta 2017.

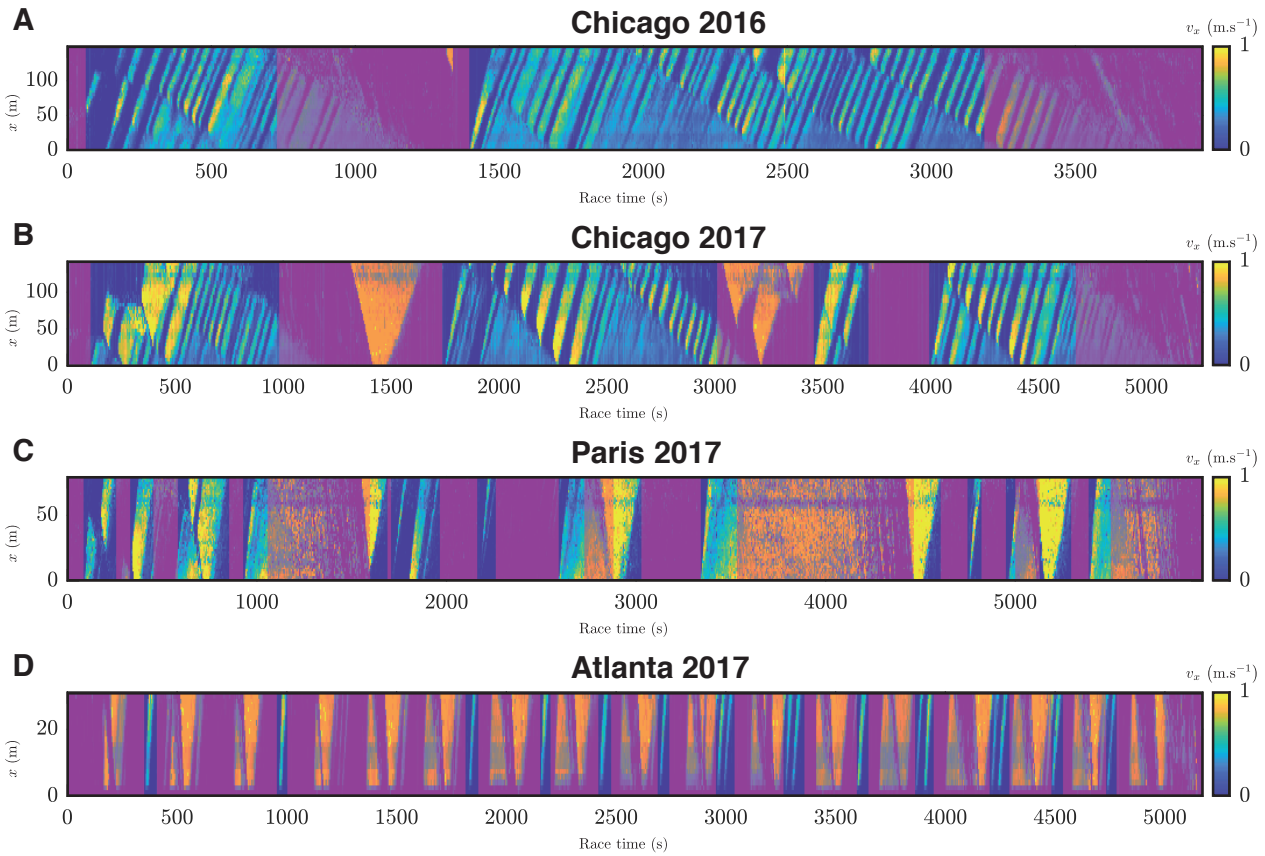

Figure 2.11 | Discarded times (purple boxes) shown on the velocity kymographs for all races. (**A**) Chicago 2016. (**B**) Chicago 2017. (**C**) Paris 2017. (**D**) Atlanta 2017.

According to Eq. (2.16), the measured displacement field is proportional to the true displacement field, and the correction factor is independent of the location of the box in space. Consequently, the estimation of the velocity field described above only has to be uniformly corrected by a factor of $(1 - h/H)$. The main errors on the local velocity measurements originates from the correlation algorithm and mostly depends on the image quality. The impact of the image rescaling is dominated by the dispersion of the individual height on the picture resulting in a dispersion of less than a percent.

Estimation of the PIV parameters

The PIV time step Δt is different from the inverse frame rate dt, and together with the box size L consist of the two PIV parameters. To the best of our knowledge, there is no universal way to set these parameters. Choosing their values is a necessary trade-off between four competing effects. First, we want the box size L to be smaller than the typical length scale of the spatial features of the velocity field. Second, the PIV time step Δt has to be smaller than the deformation time of the spatial patterns in every box. We do not want the patterns in every box to have time to deform between consecutive images. Third, we want the PIV time step Δt to be large enough to have a good resolution on the velocity field. Since the metric resolution of the displacement field is typically given by the pixel size (dx, dy), the resolution of the velocity field is $(\Delta v_x, \Delta v_y) = (dx/\Delta t, dy/\Delta t)$. Maximizing this resolution would then have us take Δt as large as possible. At last, we want the box size L to be much larger than any measured displacement $(\Delta X, \Delta Y)$. Otherwise, the image correlation algorithm is not capable of estimating the displacement field.

Manual measurements gave us a reference velocity for the walking crowd in both directions $\mathbf{v}_0 = (v_{0x}, v_{0y})$ with $v_{0x} = 0.3\text{m.s}^{-1}$ and $v_{0y} = 0.05\text{m.s}^{-1}$, and the kymographs of the speed field showed patterns of a minimal size of about 20 meters. We used these quantities to set the PIV parameters Δt and L. The chosen PIV parameters for every race, together with the error estimates, are shown in Table 2.6.

Race	Δt (s)	L (pixels)	Δv_x (m.s^{-1})	Δv_y (m.s^{-1})
Chicago 2016	2	96	0.06	0.007
Chicago 2017	2	96	0.08	0.008
Paris 2017	1	96	0.14	0.005
Atlanta 2017	1	128	0.05	0.007

Table 2.6 | PIV parameters and error estimates for every event.

Method 6: Velocity correlations

This section is divided into two parts. We first briefly recall two useful spectral formulas, and then provide details about the actual measurements performed on crowd velocity fields.

Inferring material parameters from fluctuation spectra

Here we recall the formulas for the spectra and correlations of a velocity field v obeying a Langevin differential equation of the same generic form as the hydrodynamic equation, Eq.(3), presented in the main text:

$$\partial_t v + v_0 \partial_x v = -\alpha_0 v + D\partial^2_{xx} v + \xi(x,t), \tag{2.17}$$

where $\xi(x,t)$ is a Gaussian white noise of zero mean accounting form all possible sources of *uncorrelated* disturbances to the mean velocity: $\langle \xi(x,t)\xi(x',t')\rangle \propto \delta(x-x')\delta(t-t')$. At every pulsation ω the spectrum of the velocity field $C_v(\omega,q)$ takes the form of a Lorentzian function.

$$C_v(\omega,q) \propto \frac{1}{(\omega+v_0 q)^2 + (\alpha_0 + Dq^2)^2}. \tag{2.18}$$

The time correlation function $C_v(t,q)$ is the inverse time Fourier transform of the velocity spectrum and takes the simple form

$$C_v(t,q) \propto e^{-(\alpha_0+Dq^2)|t|} e^{-i(v_0 q)t}. \tag{2.19}$$

Consequently, we can infer Eq. (2.17) by measuring either the spectra or the time correlations of the velocity fluctuations. In the context of active flows this procedure was successfully used to measure the material parameters of active colloidal fluids in [32].

Measurement of the spectral properties

With Eqs. (2.17), (2.18) and (2.19) in mind, we now study the spectral properties of flow speed and orientation fluctuations ($v(\mathbf{r},t)$, $\hat{\mathbf{v}}(\mathbf{r},t)$). In contrast with the toy model Eq. (2.17) presented above, these two fluctuating fields are two-dimensional in space $\mathbf{r} = (x,y)$. The wave vector is then also two dimensional, and for simplicity we express it in polar coordinates $\mathbf{q} = (q_x, q_y) = qe^{i\theta}$. The wave angle θ then defines the spatial direction of the Fourier transform. In our reference frame, $\theta = 0$ denotes the upstream direction of the road ($q = q_x, q_y = 0$) and $\theta = \pi/2$ the direction transverse to the road. In practice, the velocity field is Fourier transformed in space at every time step using the *fft2* MATLAB algorithm. For wave vectors making a finite angle with the road direction the value of the Fourier components is linearly interpolated. For a given wave vector, the Fourier transform in time is performed using the *fft* MATLAB routine.

We examine the spectral properties of the velocity fluctuations by looking at every wave angle independently. Let us, for now, focus on the $\theta = 0$ direction. The flow speed and orientation spectra, $C_v(\omega,q,\theta=0)$ and $C_{\hat{\mathbf{v}}}(\omega,q,\theta=0)$, are shown on Fig. 2.12. The flow speed spectral intensity is peaked on a straight line, indicating a linear dispersion relation. At low pulsations ω, the horizontal lines visible on the the flow speed spectrum (Fig. 2.12.a) are consistent with the periodicity of the race staff's displacements (main text Fig. 2a). Being only interested in the part of the spectrum corresponding to propagating waves, we filtered out this periodic component specific to the race organization by lowering the amplitude of the spectrum in the low frequencies $|\omega| < \omega_m = 0.2\,\mathrm{s}^{-1}$ by a factor of $m = 10$. At low

wave vectors, we made sure that this procedure does not interfere with the peak detection protocol. From now on, the spectrum we consider is the one obtained after this filtering operation. For the velocity orientation, Fig. 2.12b, the spectral intensity is not peaked on a straight line. Instead, it is widely distributed around the origin. This observation indicates a strong damping and the absence of propagation of the orientation fluctuations. The wide distribution of the power spectrum prevents us from filtering out the low frequencies, as it would remove part of the signal we are interested in.

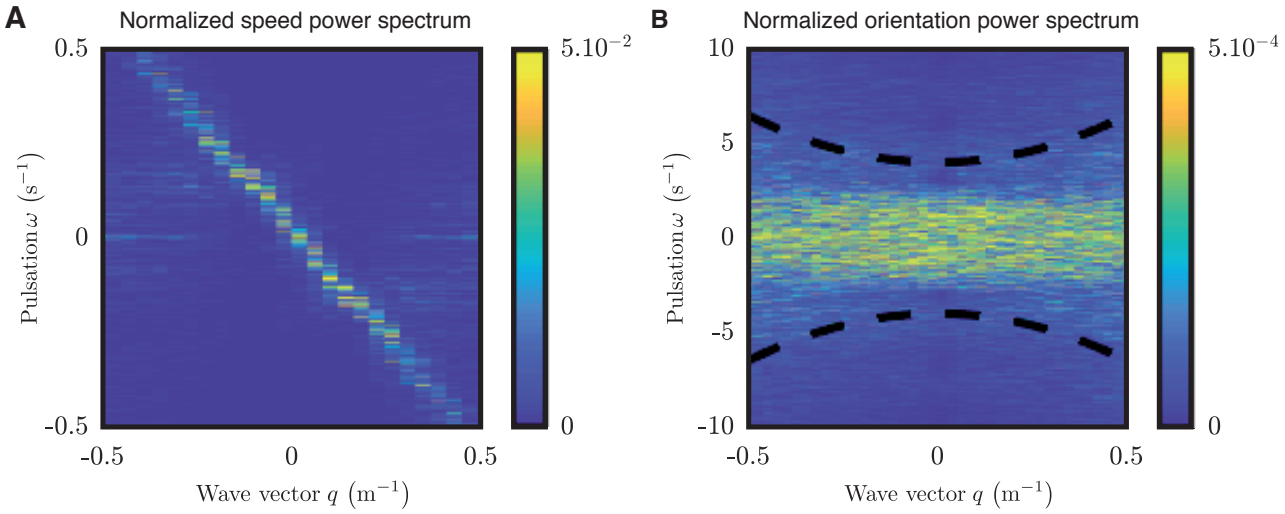

Figure 2.12 | Power spectra in the direction of the road normalized at every wave vector q. (**A**) Normalized speed power spectrum. (**B**) Normalized orientation power spectrum. Dashed-lines: visual guide for the spectral width increase as a quadratic function (main text Fig. 3h).

The material parameters were measured from real-time measurements, taking the inverse Fourier transform in time of the power spectra. As shown in the main text, Fig. 3d, the speed modes decorrelate in time as an exponentially decaying cosine function. Both periodicity and damping rate are dependent of the wave vector q. Conversely, the orientational modes do not show any sign of oscillation but a strong damping (main text, Fig. 3g), in agreement with the above spectral observations. Fitting $C_v(q, t, \theta = 0)$ with a exponentially decaying cosine function on the [0, 20] seconds time interval, and $C_{\hat{\mathbf{v}}}(q, t, \theta = 0)$ with a decaying exponential on the [0, 2] seconds time interval, we obtain the transport and damping properties of the velocity amplitude and orientation (main text, Figs. 3c, 3f and 3j).

Keeping in mind that crowds are here described as continua, the highest value of the wave vector we used is $q_m = 0.5\,\mathrm{m}^{-1}$ and corresponds to wavelengths of 12 m, which is much larger than the typical distance between the individuals in all our experiments.

Article

Dynamic response and hydrodynamics of polarized crowds

Bain, N. and Bartolo, D. Accepted for publication in Science (2018).

Modeling crowd motion is central to situations as diverse as risk prevention in mass events and visual effects rendering in the motion picture industry. The difficulty to perform quantitative measurements in model experiments has limited our ability to model pedestrian flows. We use tens of thousands of road-race participants in starting corrals to elucidate the flowing behavior of polarized crowds by probing its response to boundary motion. We establish that speed information propagates over system-spanning scales through polarized crowds, while orientational fluctuations are locally suppressed. Building on these observations, we lay out a hydrodynamic theory of polarized crowds and demonstrate its predictive power. We expect this description of human groups as active continua to provide quantitative guidelines for crowd management.

Introduction

Mesmerizing impressions of virtually all patterns observed in bird flocks, fish schools, insect swarms and even human crowds are effectively rendered in silico, by simple algorithms [77, 45]. Going beyond visual impressions and predicting the collective dynamics of groups of living creatures in response to physical, social or biological imperatives, however, remains a formidable challenge. Predictive models of collective motion have been developed following two opposite strategies. One strategy identifies local interaction rules between individuals [96]. This method has been successful, to some extent, for some animal groups including bird flocks [13, 14, 73], fish schools [31, 58], sheep herds [33], and insect swarms [2]. Determining the movement of human crowds, however, remains unsettled. Neither field measurements [43, 66, 83, 51, 7], nor laboratory experiments [63, 71, 78] have converged towards a robust set of interaction rules [23]. A different strategy for predicting collective motion ignores the individual interaction rules, instead describing the large scale motions in creature groups as spontaneous flows of active materials [59, 48, 68, 67]. Existing active hydrodynamic theories successfully account for a host of emergent patterns found in assemblies of microscopic motile bodies such as swimming bacteria [101, 100], cell tissues [25, 79, 3] and synthetic self-propelled particles [104, 62, 32]. The success of the hydrodynamic approach has been limited to microscopic bodies, and observations of

large-scale creature groups have not been quantitatively described hydrodynamically.

Results

In order to establish an active hydrodynamic description of spontaneous motion of humans, we made experimental observations of individuals in a crowd targeting the same direction. We demonstrate that information propagates over system-spanning scales in the form of hybrid waves combining density and speed fluctuations in this polarized crowd. Guided by the spectral properties of the velocity waves, we build on conservation laws and symmetry principles to construct a predictive theory of pedestrian flows without resorting to any behavioral assumption.

Experimental measurements

A good opportunity to study a polarized crowd in a controlled setting comes from large-scale running races. We made observations of thousands of runners progressing towards the start of the Bank of America Chicago Marathon (Fig. 2.13A). Starting areas of road races have a number of advantages, starting with the simple geometry as for the participants as they are gathered in a 200 m long and 20 m wide start corral (Fig. 2.13A). The starting areas also offer the possibility to repeat observations either of the same race across several years, or other races around the world. Finally, these massive polarized crowds respond to a standard excitation as runners are consistently guided towards the starting line by staff members performing repeated sequences of walks and stops (Fig. 2.13A, B).

We treated the crowd as a continuum, ignoring any specific behavior or interactions at the individual level. We characterized their large-scale motion by measuring their local density $\rho(\mathbf{r}, t)$ and velocity field, $\mathbf{v}(\mathbf{r}, t)$, in response to repeated translations of the boundary formed by the staff members (Fig. 2.13B).

At rest, we measured the density of queuing crowds to be systematically homogeneous over each entire observation window (Fig. 2.13C). The average density of $\rho_0 = 2.2 \pm 0.05$ m^{-2} was remarkably identical in all corrals and varied little from one race to another (see Methods 4). Boundary motion, however, triggers density and velocity perturbations that propagate with little attenuation over the whole extent of the corrals (Fig. 2.13C). We systematically observed this coupled dynamics in response to more than two hundred walk-and-stop excitations triggered by the race staff, in four different races. We gathered a total of $\sim 150,000$ individuals. The kymograph (Fig. 2.14A) indicates that, regardless of the width of the initial perturbation, longitudinal-velocity waves propagate upstream at a constant speed (Fig. 2.14B). We found that the wave speed $c_0 = 1.2 \pm 0.3$ m.s^{-1} is a robust characteristic of information transfer in polarized crowds for all two hundreds measurements. We also found that the shape of both the density and velocity waves were identical to the imposed displacements of the boundary (Fig. 2.14C). This faithful response to a variety of different signals (in shape and amplitude) is the signature of the propagation of non-dispersive linear waves. The density and velocity waves we observed are the result of the linear response of crowds, and are therefore intrinsically different from the nonlinear stop-and-go waves that have been extensively studied in pedestrian and car-traffic models, see e.g. [43, 44, 85, 94].

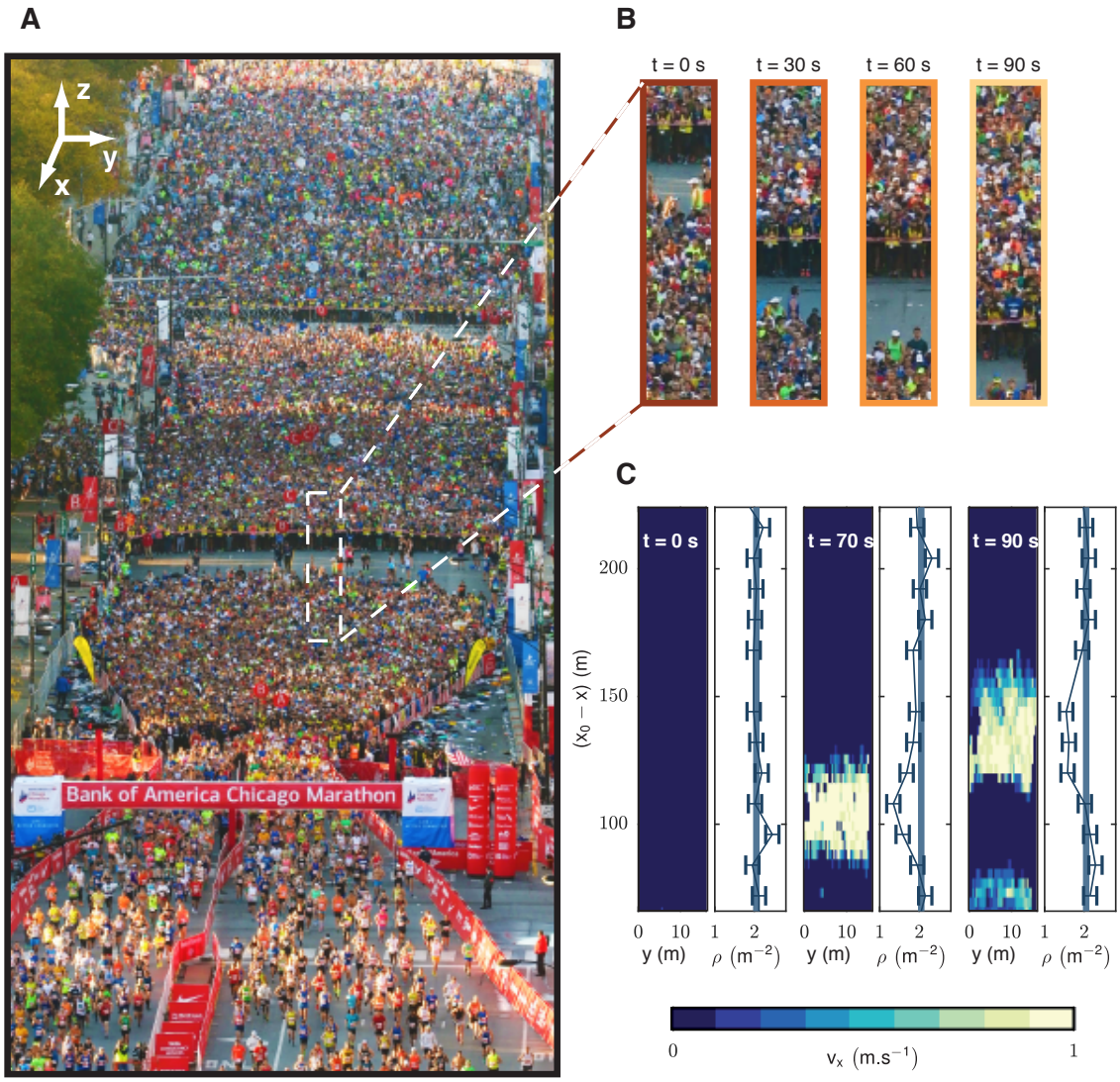

Figure 2.13 | **Hybrid-wave propagation in queuing crowds.** (**A**) Picture of the starting corrals of the Bank of America Chicago Marathon (2017) taken from an elevated observation point, see Methods 4. Thousands of runners progress towards the starting line under the guidance of race staff members. (**B**) The chain formed by the race staff advances with repeating sequences of walks and stops. (**C**) Velocity and density fields at three successive times. At $t = 0$ s the crowd is static and has a uniform density $\rho_0 \sim 2\,\mathrm{m}^{-1}$ (blue lines). At $t > 0$, as the staff members displaces the downstream boundary of the queuing crowd, a hybrid wave packet coupling velocity and density fluctuations propagates upstream. $x_0 - x$ indicates the distance from the starting line located at x_0.

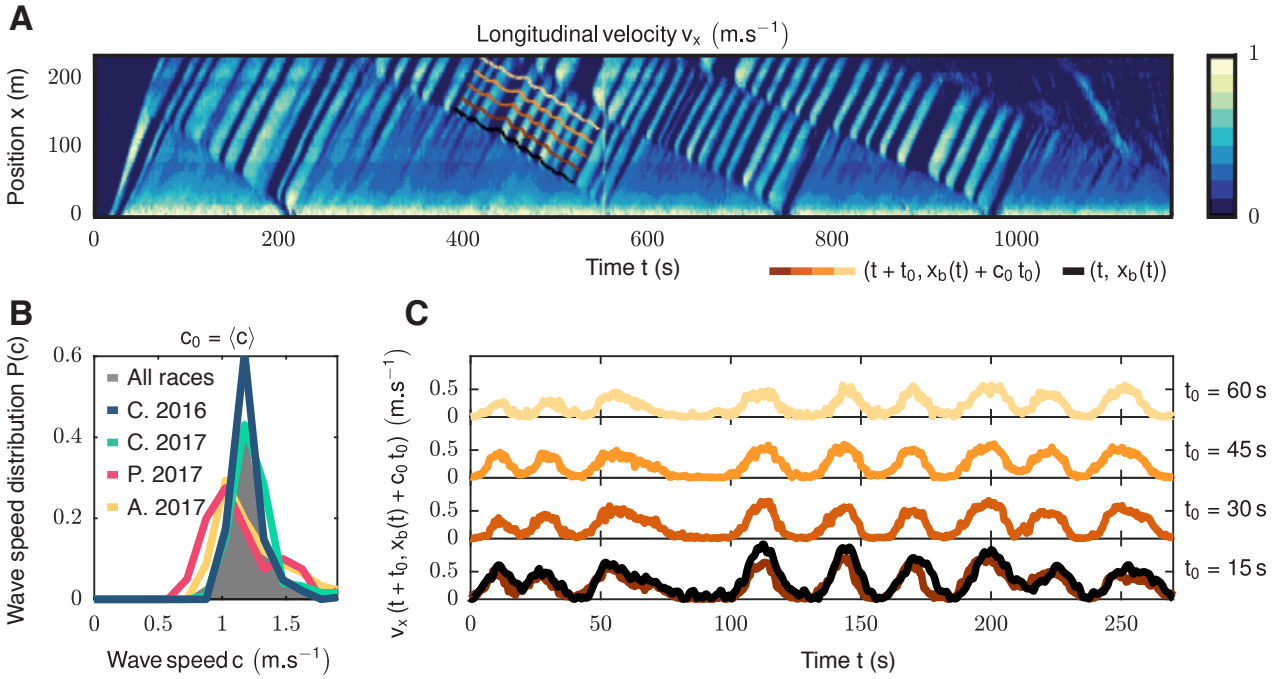

Figure 2.14 | **Underdamped propagation of linear and non dispersive velocity waves.** (**A**) Kymograph of the longitudinal velocity, averaged over the transverse direction (Chicago 2016). $x_0 - x$ indicates the distance from the starting line. A number of velocity waves are seen to propagate upstream at the same speed. (**B**) Probability distribution function of wave speed, measured for all the studied events. The typical wave speed hardly differs from one event to the other. The overall speed distribution is narrowly peaked around, $\langle c \rangle = c_0 = 1.2 \pm 0.3$ m.s^{-1}. (**C**) Black line: velocity of a chain of race-staff members $\dot{x}_b(t)$, measured by direct tracking. The corresponding positions $x_b(t)$ are reported as a black line on the kymograph in (**A**). As illustrated with the same color code on the the kymograph (**A**), the colored curves correspond to the longitudinal velocity field measured along the curves defined by the race staff position $x_b(t)$ after four different waiting times t_0: $v_x(t + t_0, x_b(t) + c_0 t_0)$. Independently of the shape of the $\dot{x}_b(t)$ signal, the velocity waves faithfully propagate the information of the boundary speed $\dot{x}_b(t)$ over system spanning scales, at constant speed.

Spectral properties

The velocity fluctuations in the crowds we observed were mainly longitudinal (Fig. 2.15A). This contrasts with other examples of polarized ensembles of self-propelled bodies (flocks), in which velocity fluctuations were mainly transverse [92, 32]. We therefore describe separately the fluctuations in the speed (where $v \sim v_x$ in our case) and in the orientation, $\hat{\mathbf{v}}$, of the crowd flow. We determine the power spectrum ($C_v(\omega, q, \theta)$) of the speed, where ω indicates the pulsation, q the modulus of the wave vector, and θ its orientation (4). We found C_v is peaked on a straight line that defines the dispersion relation of non-dispersive speed waves, $\omega = c(\theta)q$. We fitted the angular variations ($c(\theta)$) by $c(\theta) \propto \cos\theta$, giving the dispersion relation $\omega = c_0 q_x$ with the same propagation speed c_0 as from the kymograph (Fig. 2.14B). This confirmed that no speed information propagated in the transverse direction to the crowd orientation (Fig. 2.15C). In order to check whether this strong anisotropy is caused by the homogeneous boundary perturbation, we analyzed separately the dynamics of freely walking crowds in the absence of guiding staff. They respond to localized and spontaneous congestions forming in the starting funnel. The corresponding power spectrum (Fig. 2.15B, inset) is identical to that of the runners in the crowd, establishing that polarized crowds solely support longitudinal modes. Their damping dynamics is measured from the time decay of $C_v(t, q, \theta)$ (4,Figs. 2.15D, 2.15E). For all wave vectors, we defined a single damping time scale α^{-1} from a best fit of the form $C_v(t, q, \theta) \sim exp[-\alpha(q, \theta)t]cos[c(\theta)t]$. In all cases, we found diffusively damped speed waves attenuated at a rate that scales as $\alpha(q, \theta) = D(\theta)q^2$ (Fig. 2.15F). Inspecting the angular variations of $D(\theta)$ (Fig. 2.15G) we consistently found that damping primarily occurs along the x direction as $\alpha = (D_x \cos^2\theta)q^2 = D_x q_x^2$, where the diffusivity D_x is a robust material parameter: $D_x = 1 \pm 0.5$ m^2.s^{-1} in all observed crowds. This type of slow dynamics is usually typical of hydrodynamic variables characterized by long lived fluctuations in the long wave-length limit [16, 59]. This observation is seemingly at odds with the conservation laws obeyed by pedestrian crowds. Solid friction constantly exchanges momentum between the pedestrians and the ground. Momentum is not a conserved quantity, unlike in conventional liquids. Therefore, the speed is expected to be a fast variable.

Before solving this apparent contradiction, let us address the small orientational fluctuations of pedestrian flows. The correlations of $\hat{\mathbf{v}}$, $C_{\hat{\mathbf{v}}}(t, q, \theta)$, decay exponentially in less that two seconds for all wave lengths, and do not display any sign of oscillations (Fig. 2.15G).The corresponding damping rate $\alpha_{\hat{\mathbf{v}}}(q, \theta)$, varies as $\alpha_{\hat{\mathbf{v}}}(q, \theta) = \alpha_\perp + \mathcal{O}(q)$ (Fig. 2.15H). Unlike the flow speed, orientational information does not propagate in queuing crowds. Instead it relaxes in a finite time $\alpha_\perp^{-1}$, which hardly depends on the direction of the wave vector (Fig. 2.15I). This behavior contrasts with that observed in bird flocks [15, 14], and in all active systems where the emergence of directed motion arises from a spontaneous symmetry breaking [15, 14]. In the race corrals, all participants are aware of the race direction and align their body accordingly. Rotational symmetry is explicitly broken and no Goldstone mode exists. The $\alpha_\perp$ contribution to the damping rate stems from this explicit symmetry breaking. The variations of $\alpha_{\hat{\mathbf{v}}}$ with q around $\alpha_\perp$, however, are consistent with a quadratic increase of the form $\alpha_\perp + D(\theta)q^2$ (4, Fig. 2.15H). Such variations suggest that interactions between pedestrians penalize deformations of the flow field as would viscosity in a Newtonian fluid, or orientational elasticity in polar active fluids [92].

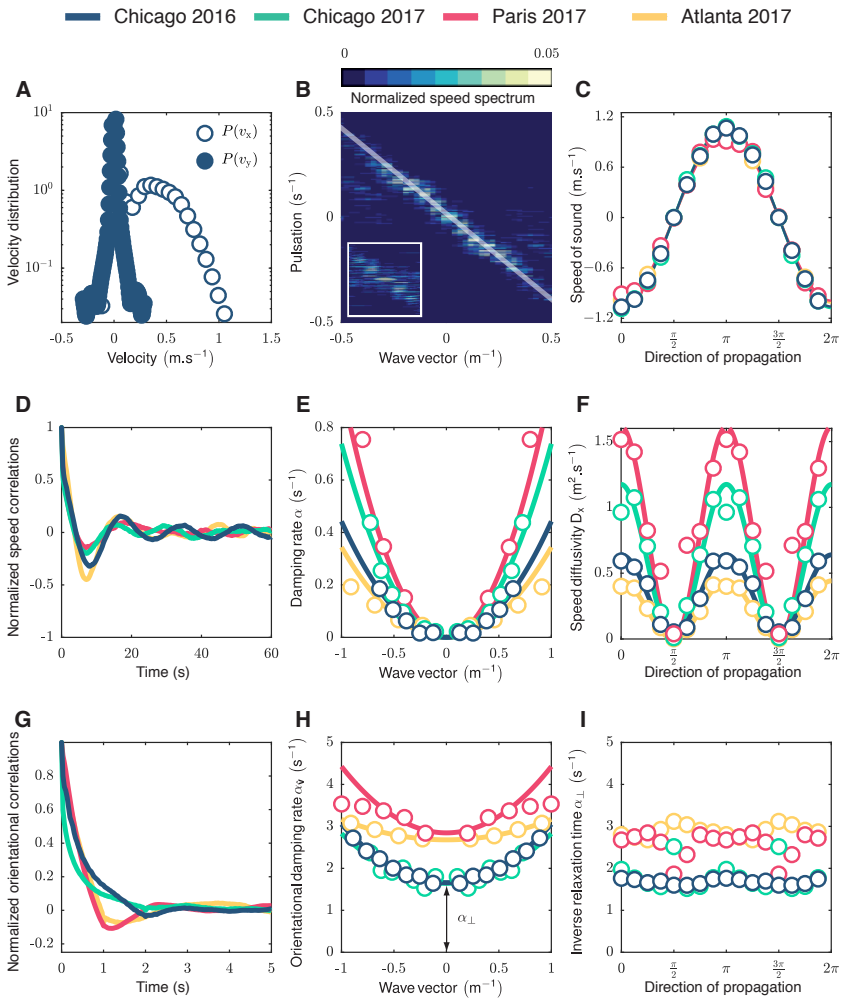

Figure 2.15 | **Spectral properties of speed waves in queuing crowds.** (**A**) Probability distribution function of the longitudinal and transverse components of the velocity field (Chicago 2016). The longitudinal component dominates. (**B**) Power spectrum of the flow speed, plotted for $\theta = \pi/4$. The spectrum is normalized at every wave vector ($\int C_v(\omega, q, \theta)\mathrm{d}q = 1$). Inset: normalized speed spectrum for a crowd in free flow conditions. Data from the Chicago 2016 experiment. (**C**) Variations of the speed of sound with the direction of the wave vector θ for all experiments. Circles: experimental data. Solid line: cosine fit. The excellent fit shows that the dispersion relation is given by $\omega = cq_x$. (**D**) Normalized speed correlations plotted versus time for all experiments ($\theta = \pi/4$, wave vector $q = 0.5\,\mathrm{m}^{-1}$). (**E**) Damping rate of the speed waves, α, plotted for all wave vectors along $\theta = \pi/4$. Circles: experimental data. Solid lines: best quadratic fits. (**F**) Variations of the speed diffusivity D_x with the direction of propagation. Circles: experimental data. Solid lines: squared cosine fits. (**G**) Normalized orientational correlations plotted versus time for all experiments ($\theta = \pi/4$, $q = 0.5\,\mathrm{m}^{-1}$). (**H**) Damping rate of the orientational fluctuations $\alpha_{\hat{\mathbf{v}}}$ plotted as a function of the wave vector ($\theta = \pi/4$). Circles: experimental data. Solid lines: best quadratic fits $\sim \alpha_\perp + D_{\hat{\mathbf{v}}} q^2$, with $D_{\hat{\mathbf{v}}} = 1.2 \pm 0.5\,\mathrm{m}^2\mathrm{s}^{-1}$. (**I**) Inverse relaxation time $\alpha_\perp$ plotted as a function of the direction of the wave vector θ. No significant angular variation is observed.

Hydrodynamic theory

The consistency between data collected from four different crowd gathering events hints towards a unified hydrodynamic description of density and speed excitations. We elucidate the dynamical response quantified in Fig. 2.14 and Fig. 2.15 from this perspective, without resorting to any behavioral assumption (4). Mass conservation gives the first hydrodynamic equation:

$$\partial_t \rho + \boldsymbol{\nabla} \cdot (\rho \mathbf{v}) = 0. \tag{2.20}$$

Momentum conservation, at lowest order in gradients, reduces to the balance between the local rate of change of momentum and the friction experienced by the crowd on the ground, $D_t[\rho(\mathbf{r},t)\mathbf{v}(\mathbf{r},t)] = \mathbf{F}(\rho,\mathbf{v},\mathbf{p}) + \mathcal{O}(\boldsymbol{\nabla})$ where D_t stands for the material derivative, and the body force $\mathbf{F}$ is a total friction force that depends in principle on the local crowd density, velocity and orientation (4). Pedestrians are polar bodies, and we classically quantify the level of local alignment between the individuals by a polarization field $\mathbf{p}(\mathbf{r},t)$ [59]. In (4) we build on a systematic theoretical framework to simplify this hydrodynamic description. In short, we take advantage of three robust key observations. First, given the measured densities, the crowd is far from a jammed regime [7, 71]. We therefore ignore elastic stresses arising from contact interactions. Second, the local direction of the flow, $\hat{\mathbf{v}}$, quickly relaxes towards the local orientation $\hat{\mathbf{p}}$. Simply put, queuing pedestrians do no walk sideways. Third, the crowd is strongly polarized, all individuals align towards the $\hat{\mathbf{x}}$ direction. In the hydrodynamic limit, we can therefore safely assume $\hat{\mathbf{p}} = \hat{\mathbf{v}} = \hat{\mathbf{x}}$. This simplification does not allow the description of orientational fluctuations which we explain in (4). It conveys, however, a clear picture of the propagation of underdamped density and speed excitations. To proceed, we need to prescribe the functional form of $\mathbf{F}$, which is a priori unknown but can be phenomenologically constructed in the spirit of a Landau expansion. At lowest order in gradients, the frictional body force is given by

$$\boldsymbol{\mathcal{F}}\left(\{\rho\},\{v\}\right) = -\Gamma_{\parallel}\left[v - \nu_0(\rho)\right]\hat{\mathbf{x}} + \mathcal{O}(\boldsymbol{\nabla}), \tag{2.21}$$

and represents the self-propulsion mechanism of the polarized crowd. The density dependent speed $\nu_0(\rho)$ quantifies the active frictional force driving the flow along $\hat{\mathbf{x}}$, and $\Gamma_{\parallel}$ is a friction coefficient that constrains the longitudinal velocity fluctuations to relax in a finite time. In the hydrodynamic limit, momentum conservation and Eq. (2.21) therefore reduce to the fundamental relation $v(\mathbf{r},t) = \nu_0(\rho(\mathbf{r},t)) + \mathcal{O}(\nabla)$ (4). This relation explains two of our main experimental findings. It shows that the fast variable v inherits the slow dynamics of the conserved density field, and readily implies that the density of static queuing crowds self-adjusts to a constant value $\rho_0 = \nu_0^{-1}(0)$ (Fig. 2.13C). In the limit of linear-response theory around the quiescent polarized state, the speed and density fluctuations, $\delta\rho$, are linearly related by $v(\mathbf{r},t) = \nu_0'(\rho_0)\delta\rho - (\beta/\Gamma_{\parallel})\partial_x\delta\rho$, where $\nu_0'(\rho_0) = \partial_\rho\nu_0(\rho_0) < 0$ and β is the crowd longitudinal compressibility (4). Together with mass conservation, this constitutive relation defines the analog of the Navier-Stokes equations for polarized crowds:

$$\partial_t v + \rho_0\nu_0'(\rho_0)\,\partial_x v - \frac{\rho_0\beta}{\Gamma_{\parallel}}\,\partial_x^2 v = 0. \tag{2.22}$$

Eqs. (2.20) and (2.22) effectively predict the dynamical response we observed in our experiments. The linear stability analysis of Eqs. (2.20) and (2.22) readily shows that polarized crowds support unidirectional and non-dispersive speed wave propagating downstream at a speed $c_0 = -\rho_0\nu_0'(\rho_0)$. Eqs. (2.20) and (2.22) also predict that their damping rate varies as q_x , in agreement with our experimental measurements (Figs. 2.15e and 2.15f). Unexpectedly, unlike in conventional fluids, the (weak) attenuation

of the speed waves does not originate from viscous stresses but instead from the competition between substrate friction and compressive stresses in the crowd. In agreement with our observations, these hybrid waves coupling density and speed fluctuations of opposite amplitude are the sole propagating modes supported by polarized crowds. In the hydrodynamic limit, the response of polarized crowds is strongly unidirectional and speed information neither propagates nor diffuses along the transverse direction (4).
From a more practical perspective, we can infer the full set of hydrodynamic parameters ofEq. (2.22) from the spectral properties of v. We can show the predictive power of our hydrodynamic model as by calibrating the celerity of the speed waves and the damping rate on a single race in Paris is sufficient to quantitatively predict the dynamics of queuing crowds observed in Chicago and Atlanta months later. In addition, our description of crowds as active continua provides effective guidelines for the management of crowds. For instance, we show that stimulations from side boundaries are inefficient, and that optimal information transfer is achieved when guiding a crowd from its forefront. We show that reorienting the direction of motion of a polarized crowd at once is impossible when relying only on locally accessible signals. Orientational cues must be provided to the entire assembly to change its direction of motion. We also predict the time it takes to set in motion, or to stop, a crowd of a given extent by providing information at its boundary.

Perspectives

Beyond these predictions, we hope the description of crowds as continua to be useful to elucidate their response to large amplitude perturbations, and their transitions from flowing liquids to amorphous solids, two situations where crowd dynamics become hazardous.

Hydrodynamic theory of polarized crowds

We introduce a hydrodynamic description of crowd flows which accounts for the underdamped propagation of longitudinal waves, and explain how to infer the material parameters of a crowd from its response to boundary motion. Unlike the previous sections, the following discussion requires a minimal background in hydrodynamic theories.

Conservation laws, symmetries and phenomenological construction

In conventional fluids, like water, the hydrodynamic variables are associated to two conserved quantities: mass and momentum [16]. In assemblies of queuing pedestrians the number density is the sole conserved variable. As they walk pedestrians continuously exchange momentum with the ground. As momentum is not conserved, velocity should not be a hydrodynamic field, i.e. a field slowly varying in time and space.

Our experiments reveal, however, that the longitudinal component of the crowd flow is a slow mode: its excitations relax over an arbitrarily large time scale provided that they correspond to sufficiently large wave lengths. More quantitatively we find that fluctuations of wave vector q are attenuated over a time that scales as q^2. Elucidating the atypical slow dynamics of these excitations is crucial to explain and predict crowd flows.

The two standard explanations for the existence of additional slow modes are criticality, and, or, the spontaneous breaking of a continuous symmetry (Goldstone modes) [16]. The normal diffusive scaling $\alpha \sim Dq^2$ does not hint towards criticality as a possible origin of this slow dynamics [13]. Furthermore, the crowd velocity is not associated to any spontaneously broken symmetry, and hence cannot be a associated to slow Goldstone modes. We therefore need to investigate the specifics of crowd motion to elucidate the unanticipated slow dynamics of longitudinal flows.

Let us first identify the minimal set of degrees of freedom required to describe the large scale dynamics of pedestrian groups. In addition to the crowd density and velocity fields ($\rho(\mathbf{r},t)$, and $\mathbf{v}(\mathbf{r},t)$), we also introduce the local polarization of the crowd $\mathbf{p}(\mathbf{r},t)$. Pedestrians are polar particles, and $\mathbf{p}(\mathbf{r},t)$ is the average direction they are facing at position $\mathbf{r}$ and time t.

The dynamics of the three fields cannot be constructed from entropy production principles as crowds operate very far from thermal equilibrium [16, 59]. Following the same approach as that introduced by Toner and Tu in the context of flocking motion [92], we write the most general dynamics for the three fields. The first equation corresponds to mass conservation:

$$\partial_t \rho + \boldsymbol{\nabla} \cdot (\rho \mathbf{v}) = 0. \tag{2.23}$$

The second equation corresponds to momentum conservation:

$$\partial_t (\rho \mathbf{v}) + \mathbf{v} \cdot \boldsymbol{\nabla} (\rho \mathbf{v}) = \boldsymbol{\nabla} \cdot \boldsymbol{\sigma} + \boldsymbol{\mathcal{F}}_v \left(\{\rho\}, \{\mathbf{v}\}, \{\mathbf{p}\} \right), \tag{2.24}$$

where the left hand side of Eq. (2.24) is the convective derivative of the momentum field, $\boldsymbol{\sigma}$ is the stress tensor and $\boldsymbol{\mathcal{F}}_v$ is a frictional body force indicating that momentum is exchanged with the ground that acts as a momentum sink (or source).

The functional form of $\boldsymbol{\mathcal{F}}_v$ is phenomenologically constructed from two central observations. Given the crowd density, the individuals cannot interact via long-range interactions. Therefore, in the spirit of a Landau expansion, at lowest order in gradients:

$$\boldsymbol{\mathcal{F}}_v\left(\{\rho\},\{\mathbf{v}\},\{\mathbf{p}\}\right) = -\boldsymbol{\Gamma}\cdot\left[\mathbf{v}-\nu_0(\rho)\mathbf{p}\right] + \mathcal{O}(\boldsymbol{\nabla}), \tag{2.25}$$

where $\boldsymbol{\Gamma} \equiv \Gamma_{\parallel}\mathbf{pp} + \Gamma_{\perp}\left(\mathbb{I}-\mathbf{pp}\right)$ is an anisotropic friction coefficient, and ν_0 quantifies the strength of the self-propulsive force in the direction of the polarization. For sake of clarity, we write the form of the gradient terms only in the linearized version of Eq. (2.25) in the next section. Our experimental observations put strong constraints on both $\boldsymbol{\Gamma}$ and $\nu_0(\rho)$. Firstly, we observe that crowds in corrals are almost perfectly polarized, $|\mathbf{p}| \sim 1$ yet in the absence of boundary perturbation, they remain at rest ($v = 0$). Unlike hydrodynamic models of flocking, the local velocity cannot be identified with polarization, in other words ν_0 is not a constant. Eqs. (2.24) and (2.25) are compatible with a homogeneous steady state at rest only if the function $\nu_0(\rho)$ vanishes at finite density ρ_0. From a different perspective, strongly polarized queuing crowds self-organize so that their density is homogeneous and equal to ρ_0, which is again consistent with our observations. The density in the corrals was indeed free to adjust as the pedestrians where not bounded from all sides, yet we measured the same density in all corals in steady state. Secondly, for time scales larger that a few seconds, all our experimental videos indicate that the crowd does not drift transversally. The pedestrians do not walk sideways, instead they proceed in the direction of their orientation $\hat{\mathbf{p}}$. This second observation constrains the friction tensor, telling us that $\Gamma_{\perp} \gg \Gamma_{\parallel}$. In the limit of very large transverse friction, Eqs. (2.24) and (2.25) reduce to a dynamical equation of the flow speed $v(\mathbf{r},t)$ and on a constraint on the flow orientation: $\hat{\mathbf{v}} = \hat{\mathbf{p}}$.

Let us now write the third and last equation of motion corresponding to the polarization dynamics. There is no generic form for this equation. In order to gain more intuition, however, we write it in the same form as the orientational hydrodynamics of polar mesophases [59]:

$$\partial_{\mathrm{t}}\mathbf{p} + (\mathbf{v}\cdot\boldsymbol{\nabla})\mathbf{p} + \boldsymbol{\Omega}\cdot\mathbf{p} = \boldsymbol{\mathcal{F}}_p + h\hat{\mathbf{x}}. \tag{2.26}$$

Given the overdamped nature of the transverse fluctuations (Fig. 3), we ignore the spinning inertia of the pedestrians [15, 102, 14]. The left hand side of Eq. (2.26) is a kinematic term commonly referred to as the corotational derivative ($\boldsymbol{\Omega}$ is the vorticity tensor defined by: $\Omega_{ij} = \frac{1}{2}(\partial_i v_j - \partial_j v_i)$). $\boldsymbol{\mathcal{F}}_p$ is a generalized torque that does not necessarily derive from an effective free energy. For instance, $\boldsymbol{\mathcal{F}}_p$ typically includes terms of the form $\mathbf{E}\cdot\mathbf{p}$, which translates the alignment of the particles with the principal orientations of the local strain $E_{ij} = \frac{1}{2}(\partial_i v_j + \partial_j v_i)$. Given the number of possible terms allowed by symmetry, even within a long wave-length approximation, a generic expression for $\boldsymbol{\mathcal{F}}_p$ would not bring additional insight. We will give its explicit form only in the limit of small amplitude fluctuations around a fully aligned state in the next section. Finally, the last term of Eq. (2.26) is analogous to a magnetic field constraining $\mathbf{p}$ to align along its direction $\hat{\mathbf{x}}$. This last term has a clear physical meaning: it translates the alignment of the pedestrians with the direction of the race, which is known by each participant.

Linearized hydrodynamics around queuing states

We now address the dynamical fluctuations around a quiescent queuing state $\rho = \rho_0$, $\mathbf{p} = \hat{\mathbf{p}}_0 = \hat{\mathbf{x}}$ and $\mathbf{v} = \mathbf{0}$.

Several simplifications can be made a priori. Given our experimental observations, we neglect the fluctuations in the magnitude of the polarization and only consider its orientational fluctuations writing $\mathbf{p} = (\cos\psi(\mathbf{r},t), \sin\psi(\mathbf{r},t))$. In addition, the friction force $\boldsymbol{\mathcal{F}}_v$ defined in Eqs. (2.24) and (2.25) causes the fast relaxation of $\hat{\mathbf{v}}$ towards the local orientation $\hat{\mathbf{p}}$. We focus here on the long time, long wave-length limit. We therefore discard the *fast* relaxational dynamics of $\mathbf{v}$ and assume $\mathbf{v}(\mathbf{r},t) = v(\mathbf{r},t)\hat{\mathbf{p}}(\mathbf{r},t)$. The direction of the flow is slaved to that of the polarization, but the flow speed can fluctuate.

In all that follows we restrain ourselves to a linear- response framework, considering only leading order terms in $\psi(\mathbf{r},t)$, $v(\mathbf{r},t)$ and in the density fluctuations $\delta\rho(\mathbf{r},t)$. Their equations of motion are given by Eq. (2.23), by the projection on the x axis of Eq. (2.24) and on the y axis of Eq. (2.26). To make these equations explicit we now need writing a generic expression for all generalized forces, performing a systematic gradient expansion up to the second order.

Let us focus first on the momentum conservation, Eq. (2.24). All terms correspond to the friction force and gradients of a generalized stress tensor, including anisotropic pressure, bulk viscosity, shear viscosity and odd stress terms, see e.g. [84], their lengthy generic expression is not insightful. For the sake of simplicity, we project Eq. (2.24) on the x axis and obtain at lowest orders in gradients:

$$\begin{aligned}\rho_0\partial_t v = \quad & -\Gamma_{\parallel}\left(v - \nu_0'(\rho_0)\delta\rho\right) + \left(-\beta\partial_x\delta\rho + c_x\partial_x v\right) \\ & + \left(\eta_x\partial_x^2 + \eta_y\partial_y^2\right)v + \gamma_{xy}\partial_{xy}\psi + \gamma_{\circ}\partial_y\psi + \left(B_x\partial_x^2 + B_y\partial_y^2\right)\delta\rho.\end{aligned} \tag{2.27}$$

The first term on the right hand side is the linearized force term, and $\nu_0'(\rho_0) \equiv \partial_\rho\nu_0(\rho_0)$. The second term on the right hand side originates from the anisotropic pressure tensor with a compressibility depending on the magnitude of the flow speed and density. The third term is a standard viscous term found in any fluid, and includes both shear and bulk viscosity contributions. The fourth and fifth terms describes flows caused by gradients in the orientation of the pedestrians. Finally the last term, is a dissipative term that originates from flows caused by density gradients. In the absence of a microscopic theory of crowd motion, all parameters are phenomenological constants.

To complete our hydrodynamic description we need an equation for the orientational variable ψ that requires expanding $\boldsymbol{\mathcal{F}}_p$ at second order in gradients. Using the same approach as above we obtain:

$$\partial_t\psi = -\alpha_\perp\psi + \left(A_\psi\partial_x\psi + A_\rho\partial_y\delta\rho + A_v\partial_y v + \xi\partial_{xy}\delta\rho + \zeta\partial_{xy}v\right) + \left(\kappa_x\partial_x^2\psi + \kappa_y\partial_y^2\psi\right) \tag{2.28}$$

In the presence of an external alignment field, the orientational dynamics is fast and relaxes to zero in a time scale $\alpha_\perp^{-1}$. The last term also has a simple interpretation, as it translates the orientational elasticity of the crowd. When κ_x, or κ_y are positive, the crowd has a finite bend and splay elasticity [59]. The other hydrodynamic parameters have nontrivial interpretations which are not central to our discussion.

Hydrodynamic limit

In the linear expansion around a quiescent queuing state Eqs. (2.27) and (2.8), flow speed and orientational fluctuations are fast variables and the only bona fide hydrodynamic variable is the density. Taking the long wavelengths and long time scales limit, orientational fluctuations relax to 0,

$$\psi = \mathcal{O}(\nabla), \tag{2.29}$$

and flow speed inherits the slow dynamics of the density fluctuations:

$$v = \nu_0'(\rho_0)\delta\rho - \beta\partial_x\delta\rho + \mathcal{O}(\nabla^2). \tag{2.30}$$

Coupling Eq. (2.30) with mass conservation Eq. (2.23), we obtain a single hydrodynamic equation for queuing crowds

$$\partial_t v + \rho_0\nu_0'(\rho_0)\,\partial_x v - \frac{\rho_0\beta}{\Gamma_\parallel}\,\partial_x^2 v = 0, \tag{2.31}$$

verified by both flow speed and density fluctuations. This theory predicts that velocity fluctuations propagate either upstream or downstream depending on the sign of ν_0', and diffuse only in the longitudinal direction (see main text, Figure 3). The speed of sound $c_0 = -\rho_0\nu_0'(\rho_0)$ is set by the slope of the so-called fundamental relation, and the diffusivity $D_x = (\rho_0\beta/\Gamma_\parallel)$ by the crowd compressibility. Theses prediction are in excellent agreement with our experimental findings which impose ν_0 to be a decreasing function of the density: the denser the crowd the slower. At last, also in consistency with our experimental observations, Eq. (2.30) constrains speed and density fluctuations to be of opposite sign: when the crowd moves forward, its density has to be smaller than the density of the static queuing crowd ρ_0 (see Fig. 1 in the main text).

In summary, the hydrodynamic theory defined by Eq. (2.31) correctly accounts for the observation of a single sound mode propagating at a constant speed away from the starting line. We expect this behavior to be generic to all queuing crowds.

Orientational dynamics

The orientational dynamics is fast, and may therefore be more sensitive to the very details of the interactions between the individuals forming the crowd. Our experiments however reveal two robust features common to the four events: (i) At long wavelengths, the damping of the orientational fluctuations hardly depends on the orientation of the wave vector. (ii) At shorter wave lengths, the damping rate grows quadratically with the wave vector. Both features are, again, correctly captured by Eqs. (2.23), (2.24) and (2.26). When linearized around a quiescent queuing state, these three equations reduce to the linear system

$$\partial_t \begin{pmatrix} \delta\rho \\ \rho_0 v \\ \psi \end{pmatrix} = (\mathbf{T} + \mathbf{D}) \cdot \begin{pmatrix} \delta\rho \\ v \\ \psi \end{pmatrix}, \tag{2.32}$$

where $\mathbf{T}$ gathers the transport terms:

$$\mathbf{T} = \begin{pmatrix} 0 & -i\rho_0 q_x & 0 \\ -i\beta q_x & ic_x q_x & i\gamma_0 q_y \\ iA_\rho q_y & iA_v q_y & iA_\psi q_x \end{pmatrix}, \tag{2.33}$$

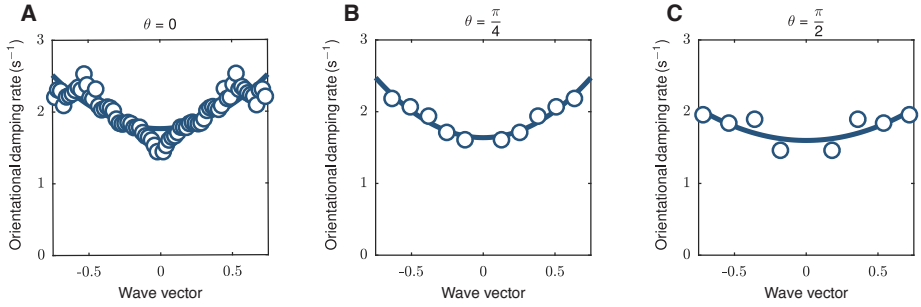

Figure 2.16 | (Chicago 2016) Orientational damping rate as a function of the wave vector, in directions of propagation (**A**) $\theta = 0$, (**B**) $\theta = \pi/4$, and (**C**) $\theta = \pi/2$. In every propagation direction, the orientational damping grows quadratically with the wave vector.

and $\mathbf{D}$ the damping terms:

$$\mathbf{D} = \begin{pmatrix} 0 & 0 & 0 \\ \Gamma_\parallel \nu_0'(\rho_0) - B_x q_x^2 - B_y q_y^2 & -\Gamma_\parallel - \eta_x q_x^2 - \eta_y q_y^2 & -\gamma_{xy} q_x q_y \\ -\xi q_x q_y & -\zeta q_x q_y & -\alpha_\perp - \kappa_x q_x^2 - \kappa_y q_y^2 \end{pmatrix}. \tag{2.34}$$

There is no simple analytic formula for the eigenvalues of $\boldsymbol{T} + \boldsymbol{D}$. We can, however, gain some physical insight focusing on the longitudinal and transverse directions.

In the longitudinal direction ($\theta = 0$), the orientational fluctuations decouple from the other variables and boevys the linear equation:

$$\partial_t \psi + \alpha_\perp \psi + A_\psi \partial_x \psi + \kappa_x \partial_x^2 \psi = 0. \tag{2.35}$$

Orientational waves are obviously overdamped at a rate $\lambda(\theta = 0) = \alpha_\perp + \kappa_x q^2$. The rotational friction and the orientational elasticity of the crowd (κ_x) conspire to suppress orientational fluctuations.

In the transverse direction ($\theta = \pi/2$), orientational fluctuations only decouple from density and speed modes in the small q limit. The associated damping rate is also quadratic in q:

$$\lambda_\psi\left(\theta = \frac{\pi}{2}\right) = \alpha_\perp + \left(\kappa_y - \frac{A_v \gamma_0}{\alpha_\perp - \Gamma_\parallel}\right) q^2. \tag{2.36}$$

As in the longitudinal case, orientational elasticity (κ_y term) contributes to damping the orientational fluctuations. The $A_v\gamma_0/(\alpha_\perp - \Gamma_\parallel)$ term does not have a simple interpretation, as it combines contributions from both the frictional stresses and force and from the convective terms in the orientational dynamics. We note that in certain situations, this additional term can reverse the sign of $\lambda(\theta = \pi/2)$ thereby resulting into a bending instability of the crowd orientation.

The $\alpha_\perp + \alpha' q^2$ scaling was numerically confirmed for all orientations. These results are yet again in excellent agreement with our experimental findings as shown in (Fig. 2.16) and main text (Figs. 3h, 3i and 3j). The experimental measurements for Chicago 2016 suggest that the diffusive contribution of the orientational damping varies as $D_{\hat{\mathbf{v}}}(\theta) \sim D^x_{\hat{\mathbf{v}}} q_x^2 + D^y_{\hat{\mathbf{v}}} q_y^2$ (Fig. 2.17). The measurements on the other

events are, however, too noisy to conclude. A confirmation of these variations would further simplify the complete hydrodynamic description of the crowd as they imply that all terms involving derivatives of the form ∂_{xy} are associated to vanishingly small material parameters.

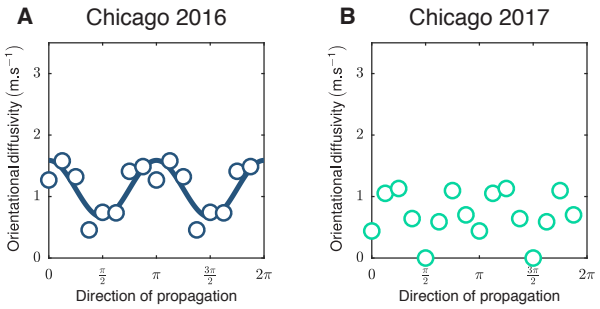

Figure 2.17 | Orientational diffusivity as a function of the direction of propagation. (**A**) Chicago 2016. (**B**) Chicago 2017.

References

[1] Ronald J Adrian and Jerry Westerweel. *Particle image velocimetry*. Number 30. Cambridge University Press, 2011 (cit. on p. 66).

[2] Alessandro Attanasi, Andrea Cavagna, Lorenzo Del Castello, Irene Giardina, Stefania Melillo, Leonardo Parisi, Oliver Pohl, Bruno Rossaro, Edward Shen, Edmondo Silvestri, et al. Collective behaviour without collective order in wild swarms of midges. *PLoS computational biology*, 10(7):e1003697, 2014 (cit. on p. 73).

[3] Shiladitya Banerjee, Kazage J. C. Utuje, and M. Cristina Marchetti. Propagating stress waves during epithelial expansion. *Phys. Rev. Lett.*, 114:228101, Jun 2015 (cit. on p. 73).

[4] Muhammad Baqui and Rainald Löhner. Real-time crowd safety and comfort management from cctv images. In *Real-Time Image and Video Processing 2017*, volume 10223, page 1022304. International Society for Optics and Photonics, 2017 (cit. on p. 66).

[5] Nicola Bellomo and Abdelghani Bellouquid. On multiscale models of pedestrian crowds from mesoscopic to macroscopic. *Commun. Math. Sci*, 13(7):1649–1664, 2015 (cit. on p. 20).

[6] Arianna Bottinelli, David Sumpter, and Jesse Silverberg. Jammed humans in high-density crowd disasters. In *APS Meeting Abstracts*, 2017 (cit. on p. 9).

[7] Arianna Bottinelli, David T. J. Sumpter, and Jesse L. Silverberg. Emergent structural mechanisms for high-density collective motion inspired by human crowds. *Phys. Rev. Lett.*, 117:228301, Nov 2016 (cit. on pp. 73 and 79).

[8] Antoine Bricard, Jean-Baptiste Caussin, Debasish Das, Charles Savoie, Vijayakumar Chikkadi, Kyohei Shitara, Oleksandr Chepizhko, Fernando Peruani, David Saintillan, and Denis Bartolo. Emergent vortices in populations of colloidal rollers. *Nat. Commun.*, 6:7470, jun 2015 (cit. on p. 42).

[9] Antoine Bricard, Jean-Baptiste Caussin, Nicolas Desreumaux, Olivier Dauchot, and Denis Bartolo. Emergence of macroscopic directed motion in populations of motile colloids. *Nature*, 503(7474):95–8, nov 2013 (cit. on pp. 34 and 42).

[10] Daniel S. Calovi, Ugo Lopez, Paul Schuhmacher, Hugues Chaté, Clément Sire, and Guy Theraulaz. Collective response to perturbations in a data-driven fish school model. *Journal of The Royal Society Interface*, 12(104), 2015 (cit. on p. 34).

[11] Michael E Cates and Julien Tailleur. Motility-Induced Phase Separation. *Annual Review of Condensed Matter Physics*, 6(1):219–244, 2015 (cit. on pp. 27 and 33).

[12] Jean-Baptiste Caussin and Denis Bartolo. Tailoring the interactions between self-propelled bodies. *The European Physical Journal E*, 37(6):55, 2014 (cit. on p. 34).

[13] Andrea Cavagna and Irene Giardina. Bird flocks as condensed matter. *Annu. Rev. Condens. Matter Phys.*, 5(1):183–207, 2014 (cit. on pp. 34, 73, and 81).

[14] Andrea Cavagna, Irene Giardina, and Tomás S Grigera. The physics of flocking: Correlation as a compass from experiments to theory. *Physics Reports*, 2017 (cit. on pp. 73, 77, and 82).

[15] Andrea Cavagna, Irene Giardina, Tomas S Grigera, Asja Jelic, Dov Levine, Sriram Ramaswamy, and Massimiliano Viale. Silent flocks: constraints on signal propagation across biological groups. *Physical review letters*, 114(21):218101, 2015 (cit. on pp. 77 and 82).

[16] Paul M Chaikin and Tom C Lubensky. *Principles of condensed matter physics*. Cambridge university press, 2000 (cit. on pp. 40, 77, and 81).

[17] Ujjal Chattaraj, Armin Seyfried, and Partha Chakroborty. Comparison of pedestrian fundamental diagram across cultures. *Advances in complex systems*, 12(03):393–405, 2009 (cit. on p. 12).

[18] Chong Chen, Song Liu, Xia-qing Shi, Hugues Chaté, and Yilin Wu. Weak synchronization and large-scale collective oscillation in dense bacterial suspensions. *Nature*, 542(7640):210–214, Feb 2017 (cit. on p. 34).

[19] Robert T Collins. A space-sweep approach to true multi-image matching. In *Computer Vision and Pattern Recognition, 1996. Proceedings CVPR'96, 1996 IEEE Computer Society Conference on*, pages 358–363. IEEE, 1996 (cit. on p. 61).

[20] Iain D Couzin and Nigel R Franks. Self-organized lane formation and optimized traffic flow in army ants. *Proceedings of the Royal Society of London B: Biological Sciences*, 270(1511):139–146, 2003 (cit. on pp. 14 and 25).

[21] Iain D Couzin, Jens Krause, Nigel R Franks, and Simon A Levin. Effective leadership and decision-making in animal groups on the move. *Nature*, 433(7025):513–516, feb 2005 (cit. on p. 27).

[22] Iain D. Couzin, Jens Krause, Richard James, Graeme D. Ruxton, and Nigel R. Franks. Collective memory and spatial sorting in animal groups. *Journal of Theoretical Biology*, 218(1):1 – 11, 2002 (cit. on p. 34).

[23] Emiliano Cristiani, Benedetto Piccoli, and Andrea Tosin. *Multiscale modeling of pedestrian dynamics*, volume 12. Springer, 2014 (cit. on pp. 15 and 73).

[24] Pierre Degond, Cécile Appert-Rolland, Mehdi Moussaid, Julien Pettré, and Guy Theraulaz. A hierarchy of heuristic-based models of crowd dynamics. *Journal of Statistical Physics*, 152(6):1033–1068, 2013 (cit. on p. 20).

[25] G. Duclos, C. Blanch-Mercader, V. Yashunsky, G. Salbreux, J. F. Joanny, J. Prost, and P. Silberzan. Spontaneous shear flow in confined cellular nematics. *Nature Physics*, 2018 (cit. on p. 73).

[26] Dorine C Duives, Winnie Daamen, and Serge P Hoogendoorn. State-of-the-art crowd motion simulation models. *Transportation research part C: emerging technologies*, 37:193–209, 2013 (cit. on p. 15).

[27] J. Dzubiella, G. P. Hoffmann, and H. Löwen. Lane formation in colloidal mixtures driven by an external field. *Phys. Rev. E*, 65:021402, Jan 2002 (cit. on pp. 33 and 34).

[28] Morris R Flynn, Aslan R Kasimov, J-C Nave, Rodolfo R Rosales, and Benjamin Seibold. Self-sustained nonlinear waves in traffic flow. *Physical Review E*, 79(5):056113, 2009 (cit. on p. 21).

[29] Dieter Forster, Tom C Lubensky, Paul C Martin, Jack Swift, and PS Pershan. Hydrodynamics of liquid crystals. *Physical Review Letters*, 26(17):1016, 1971 (cit. on p. 55).

[30] John J Fruin. The causes and prevention of crowd disasters. *Engineering for crowd safety*, 1(10):99–108, 1993 (cit. on pp. 9 and 10).

[31] Jacques Gautrais, Francesco Ginelli, Richard Fournier, Stéphane Blanco, Marc Soria, Hugues Chaté, and Guy Theraulaz. Deciphering interactions in moving animal groups. *Plos computational biology*, 8(9):e1002678, 2012 (cit. on p. 73).

[32] Delphine Geyer, Alexandre Morin, and Denis Bartolo. Sounds and hydrodynamics of polar active fluids. *Nature materials*, page 1, 2018 (cit. on pp. 70, 73, and 77).

[33] Francesco Ginelli, Fernando Peruani, Marie-Helène Pillot, Hugues Chaté, Guy Theraulaz, and Richard Bon. Intermittent collective dynamics emerge from conflicting imperatives in sheep herds. *Proceedings of the National Academy of Sciences*, 112(41):12729–12734, 2015 (cit. on p. 73).

[34] T Glanz and H Löwen. The nature of the laning transition in two dimensions. *Journal of Physics: Condensed Matter*, 24(46):464114, 2012 (cit. on pp. 26, 33, and 34).

[35] Guillaume Grégoire and Hugues Chaté. Onset of collective and cohesive motion. *Phys. Rev. Lett.*, 92:025702, Jan 2004 (cit. on p. 34).

[36] G. Grinstein, D.-H. Lee, and Subir Sachdev. Conservation laws, anisotropy, and "self-organized criticality" in noisy nonequilibrium systems. *Phys. Rev. Lett.*, 64:1927–1930, Apr 1990 (cit. on pp. 41, 47, and 48).

[37] Janne Heikkila and Olli Silven. Calibration procedure for short focal length off-the-shelf ccd cameras. In *Pattern Recognition, 1996., Proceedings of the 13th International Conference on*, volume 1, pages 166–170. IEEE, 1996 (cit. on p. 61).

[38] Janne Heikkila and Olli Silven. A four-step camera calibration procedure with implicit image correction. In *Computer Vision and Pattern Recognition, 1997. Proceedings., 1997 IEEE Computer Society Conference on*, pages 1106–1112. IEEE, 1997 (cit. on p. 61).

[39] Dirk Helbing, Lubos Buzna, Anders Johansson, and Torsten Werner. Self-organized pedestrian crowd dynamics: Experiments, simulations, and design solutions. *Transportation science*, 39(1):1–24, 2005 (cit. on p. 15).

[40] Dirk Helbing, Illés Farkas, and Tamas Vicsek. Simulating dynamical features of escape panic. *Nature*, 407(6803):487, 2000 (cit. on p. 17).

[41] Dirk Helbing, Illés J. Farkas, and Tamás Vicsek. Freezing by heating in a driven mesoscopic system. *Phys. Rev. Lett.*, 84:1240–1243, Feb 2000 (cit. on pp. 14, 17, and 33).

[42] Dirk Helbing and AF Johansson. On the controversy around daganzo's requiem for and aw-rascle's resurrection of second-order traffic flow models. *The European Physical Journal B*, 69(4):549–562, 2009 (cit. on p. 21).

[43] Dirk Helbing, Anders Johansson, and Habib Zein Al-Abideen. Dynamics of crowd disasters: An empirical study. *Phys. Rev. E*, 75:046109, Apr 2007 (cit. on pp. 9, 10, 12, 13, 15, 18, 19, 52, 73, and 74).

[44] Dirk Helbing, Anders Johansson, Joachim Mathiesen, Mogens H. Jensen, and Alex Hansen. Analytical approach to continuous and intermittent bottleneck flows. *Phys. Rev. Lett.*, 97:168001, Oct 2006 (cit. on pp. 21 and 74).

[45] Dirk Helbing and Péter Molnár. Social force model for pedestrian dynamics. *Phys. Rev. E*, 51:4282–4286, May 1995 (cit. on pp. 17, 33, and 73).

[46] S Hoogendoorn and W Daamen. *Self-Organization in Pedestrian Flow*, pages 373–382. Springer Berlin Heidelberg, Berlin, Heidelberg, 2005 (cit. on p. 33).

[47] RL Hughes. The flow of large crowds of pedestrians. *Mathematics and Computers in Simulation*, 53(4-6):367–370, 2000 (cit. on p. 21).

[48] Roger L Hughes. The flow of human crowds. *Annual review of fluid mechanics*, 35(1):169–182, 2003 (cit. on p. 73).

[49] Haroon Idrees, Imran Saleemi, Cody Seibert, and Mubarak Shah. Multi-source multi-scale counting in extremely dense crowd images. In *Computer Vision and Pattern Recognition (CVPR), 2013 IEEE Conference on*, pages 2547–2554. IEEE, 2013 (cit. on p. 64).

[50] Asja Jelić, Cécile Appert-Rolland, Samuel Lemercier, and Julien Pettré. Properties of pedestrians walking in line: Fundamental diagrams. *Physical Review E*, 85(3):036111, 2012 (cit. on pp. 12, 13, and 15).

[51] Ioannis Karamouzas, Brian Skinner, and Stephen J. Guy. Universal power law governing pedestrian interactions. *Phys. Rev. Lett.*, 113:238701, Dec 2014 (cit. on pp. 7, 8, 18, and 73).

[52] Katherine Klymko, Phillip L. Geissler, and Stephen Whitelam. Microscopic origin and macroscopic implications of lane formation in mixtures of oppositely driven particles. *Phys. Rev. E*, 94:022608, Aug 2016 (cit. on p. 36).

[53] Richard Knoblauch, Martin Pietrucha, and Marsha Nitzburg. Field studies of pedestrian walking speed and start-up time. *Transportation Research Record: Journal of the Transportation Research Board*, (1538):27–38, 1996 (cit. on p. 7).

[54] Matthias Kohl, Alexei V Ivlev, Philip Brandt, Gregor E Morfill, and Hartmut Löwen. Microscopic theory for anisotropic pair correlations in driven binary mixtures. *Journal of Physics: Condensed Matter*, 24(46):464115, 2012 (cit. on pp. 33, 38, and 41).

[55] Tobias Kretz, Anna Grünebohm, Maike Kaufman, Florian Mazur, and Michael Schreckenberg. Experimental study of pedestrian counterflow in a corridor. *Journal of Statistical Mechanics: Theory and Experiment*, 2006(10):P10001, 2006 (cit. on pp. 14, 25, and 33).

[56] Samuel Lemercier, Asja Jelic, Richard Kulpa, Jiale Hua, Jérôme Fehrenbach, Pierre Degond, Cécile Appert-Rolland, Stéphane Donikian, and Julien Pettré. Realistic following behaviors for crowd simulation. In *Computer Graphics Forum*, volume 31, pages 489–498. Wiley Online Library, 2012 (cit. on pp. 12, 13, and 15).

[57] Mirjam E Leunissen, Christina G Christova, Antti-Pekka Hynninen, C Patrick Royall, Andrew I Campbell, Arnout Imhof, Marjolein Dijkstra, Rene van Roij, and Alfons van Blaaderen. Ionic colloidal crystals of oppositely charged particles. *Nature*, 437(7056):235–240, sep 2005 (cit. on pp. 14, 25, and 33).

[58] Ugo Lopez, Jacques Gautrais, Iain D Couzin, and Guy Theraulaz. From behavioural analyses to models of collective motion in fish schools. *Interface focus*, 2(6):693–707, 2012 (cit. on pp. 27 and 73).

[59] M. C. Marchetti, J. F. Joanny, S. Ramaswamy, T. B. Liverpool, J. Prost, Madan Rao, and R. Aditi Simha. Hydrodynamics of soft active matter. *Rev. Mod. Phys.*, 85:1143–1189, Jul 2013 (cit. on pp. 33, 34, 41, 73, 77, 79, 81, 82, and 83).

[60] Stanley Milgram, Hans Toch, and John Drury. *Collective behavior: Crowds and social movements.* 1969 (cit. on p. 33).

[61] Masamitsu Mōri and Hiroshi Tsukaguchi. A new method for evaluation of level of service in pedestrian facilities. *Transportation Research Part A: General*, 21(3):223–234, 1987 (cit. on pp. 9 and 10).

[62] Alexandre Morin and Denis Bartolo. Flowing active liquids in a pipe: Hysteretic response of polar flocks to external fields. *Phys. Rev. X*, 8:021037, May 2018 (cit. on p. 73).

[63] Mehdi Moussaid, Elsa G Guillot, Mathieu Moreau, Jérôme Fehrenbach, Olivier Chabiron, Samuel Lemercier, Julien Pettré, Cecile Appert-Rolland, Pierre Degond, and Guy Theraulaz. Traffic instabilities in self-organized pedestrian crowds. *PLoS computational biology*, 8(3):e1002442, 2012 (cit. on pp. 33 and 73).

[64] Mehdi Moussaïd, Dirk Helbing, Simon Garnier, Anders Johansson, Maud Combe, and Guy Theraulaz. Experimental study of the behavioural mechanisms underlying self-organization in human crowds. *Proceedings of the Royal Society of London B: Biological Sciences*, pages rspb–2009, 2009 (cit. on pp. 18 and 19).

[65] Mehdi Moussaïd, Niriaska Perozo, Simon Garnier, Dirk Helbing, and Guy Theraulaz. The walking behaviour of pedestrian social groups and its impact on crowd dynamics. *PLOS ONE*, 5(4):1–7, 2010 (cit. on p. 33).

[66] Mehdi Moussaïd, Dirk Helbing, and Guy Theraulaz. How simple rules determine pedestrian behavior and crowd disasters. *Proceedings of the National Academy of Sciences*, 108(17):6884–6888, 2011 (cit. on pp. 18, 19, 33, and 73).

[67] Rui Ni and Nicholas T Ouellette. On the tensile strength of insect swarms. *Physical biology*, 13(4):045002, 2016 (cit. on p. 73).

[68] Rui Ni, James G. Puckett, Eric R. Dufresne, and Nicholas T. Ouellette. Intrinsic fluctuations and driven response of insect swarms. *Phys. Rev. Lett.*, 115:118104, Sep 2015 (cit. on p. 73).

[69] Maureen O'Hara. Bubbles: Some perspectives (and loose talk) from history. *The Review of Financial Studies*, 21(1):11–17, 2008 (cit. on p. 7).

[70] SJ Older. Movement of pedestrians on footways in shopping streets. *Traffic engineering & control*, 10(4), 1968 (cit. on pp. 19 and 33).

[71] José M. Pastor, Angel Garcimartín, Paula A. Gago, Juan P. Peralta, César Martín-Gómez, Luis M. Ferrer, Diego Maza, Daniel R. Parisi, Luis A. Pugnaloni, and Iker Zuriguel. Experimental proof of faster-is-slower in systems of frictional particles flowing through constrictions. *Phys. Rev. E*, 92:062817, Dec 2015 (cit. on pp. 14, 16, 17, 73, and 79).

[72] Harold J Payne. Freflo: A macroscopic simulation model of freeway traffic. *Transportation Research Record*, (722), 1979 (cit. on p. 20).

[73] Daniel JG Pearce, Adam M Miller, George Rowlands, and Matthew S Turner. Role of projection in the control of bird flocks. *Proceedings of the National Academy of Sciences*, 111(29):10422–10426, 2014 (cit. on p. 73).

[74] A. Peshkov, E. Bertin, F. Ginelli, and H. Chaté. Boltzmann-ginzburg-landau approach for continuous descriptions of generic vicsek-like models. *Eur. Phys. J. Spec. Top.*, 223(7):1315–1344, 2014 (cit. on p. 40).

[75] Abishai Polus, Joseph L Schofer, and Ariela Ushpiz. Pedestrian flow and level of service. *Journal of transportation engineering*, 109(1):46–56, 1983 (cit. on pp. 9 and 10).

[76] Alexis Poncet, Olivier Bénichou, Vincent Démery, and Gleb Oshanin. Universal long ranged correlations in driven binary mixtures. *Phys. Rev. Lett.*, 118:118002, Mar 2017 (cit. on pp. 26, 31, 34, 38, 41, and 48).

[77] Craig W Reynolds. Flocks, herds and schools: A distributed behavioral model. In *ACM SIGGRAPH computer graphics*, volume 21, pages 25–34. ACM, 1987 (cit. on p. 73).

[78] Kevin W Rio, Gregory C Dachner, and William H Warren. Local interactions underlying collective motion in human crowds. *Proc. R. Soc. B*, 285(1878):20180611, 2018 (cit. on pp. 11, 18, 27, and 73).

[79] Thuan Beng Saw, Amin Doostmohammadi, Vincent Nier, Leyla Kocgozlu, Sumesh Thampi, Yusuke Toyama, Philippe Marcq, Chwee Teck Lim, Julia M Yeomans, and Benoit Ladoux. Topological defects in epithelia govern cell death and extrusion. *Nature*, 544(7649):212, 2017 (cit. on p. 73).

[80] Andreas Schadschneider, Debashish Chowdhury, and Katsuhiro Nishinari. *Stochastic transport in complex systems: from molecules to vehicles*. Elsevier, 2010 (cit. on pp. 15 and 18).

[81] Hamid Seyed-Allaei, Lutz Schimansky-Geier, and Mohammad Reza Ejtehadi. Gaussian theory for spatially distributed self-propelled particles. *Phys. Rev. E*, 94:062603, Dec 2016 (cit. on p. 42).

[82] Armin Seyfried, Bernhard Steffen, Wolfram Klingsch, and Maik Boltes. The fundamental diagram of pedestrian movement revisited. *Journal of Statistical Mechanics: Theory and Experiment*, 2005(10):P10002, 2005 (cit. on pp. 9, 10, 12, and 13).

[83] Jesse L Silverberg, Matthew Bierbaum, James P Sethna, and Itai Cohen. Collective motion of humans in mosh and circle pits at heavy metal concerts. *Physical review letters*, 110(22):228701, 2013 (cit. on pp. 9 and 73).

[84] Anton Souslov, Benjamin C van Zuiden, Denis Bartolo, and Vincenzo Vitelli. Topological sound in active-liquid metamaterials. *Nature Physics*, 13(11):1091, 2017 (cit. on p. 83).

[85] Yuki Sugiyama, Minoru Fukui, Macoto Kikuchi, Katsuya Hasebe, Akihiro Nakayama, Katsuhiro Nishinari, Shin-ichi Tadaki, and Satoshi Yukawa. Traffic jams without bottlenecks—experimental evidence for the physical mechanism of the formation of a jam. *New journal of physics*, 10(3):033001, 2008 (cit. on p. 74).

[86] Yutaka Sumino, Ken H. Nagai, Yuji Shitaka, Dan Tanaka, Kenichi Yoshikawa, Hugues Chate, and Kazuhiro Oiwa. Large-scale vortex lattice emerging from collectively moving microtubules. *Nature*, 483(7390):448–452, MAR 22 2012 (cit. on p. 34).

[87] KR Sütterlin, A Wysocki, AV Ivlev, C Räth, HM Thomas, M Rubin-Zuzic, WJ Goedheer, VE Fortov, AM Lipaev, VI Molotkov, et al. Dynamics of lane formation in driven binary complex plasmas. *Physical review letters*, 102(8):085003, 2009 (cit. on pp. 14 and 25).

[88] Peter Temin and Hans-Joachim Voth. Riding the south sea bubble. *American Economic Review*, 94(5):1654–1668, 2004 (cit. on p. 7).

[89] Florian Thüroff, Christoph A. Weber, and Erwin Frey. Numerical treatment of the boltzmann equation for self-propelled particle systems. *Phys. Rev. X*, 4:041030, Nov 2014 (cit. on p. 40).

[90] Wei Tian, Weiguo Song, Jian Ma, Zhiming Fang, Armin Seyfried, and Jack Liddle. Experimental study of pedestrian behaviors in a corridor based on digital image processing. *Fire Safety Journal*, 47:8–15, 2012 (cit. on p. 52).

[91] John Toner and Yuhai Tu. Long-range order in a two-dimensional dynamical XY model: How birds fly together. *Phys. Rev. Lett.*, 75:4326–4329, Dec 1995 (cit. on pp. 27, 33, and 40).

[92] John Toner and Yuhai Tu. Flocks, herds, and schools: A quantitative theory of flocking. *Physical review E*, 58(4):4828, 1998 (cit. on pp. 21, 77, and 81).

[93] John Toner, Yuhai Tu, and Sriram Ramaswamy. Hydrodynamics and phases of flocks. *Annals of Physics*, 318(1):170–244, 2005 (cit. on p. 33).

[94] Antoine Tordeux, Guillaume Costeseque, Michael Herty, and Armin Seyfried. From traffic and pedestrian follow-the-leader models with reaction time to first order convection-diffusion flow models. *SIAM Journal on Applied Mathematics*, 78(1):63–79, 2018 (cit. on p. 74).

[95] Tamás Vicsek, András Czirók, Eshel Ben-Jacob, Inon Cohen, and Ofer Shochet. Novel type of phase transition in a system of self-driven particles. *Physical review letters*, 75(6):1226, 1995 (cit. on p. 11).

[96] Tamás Vicsek and Anna Zafeiris. Collective motion. *Physics Reports*, 517(3-4):71–140, 2012 (cit. on pp. 34 and 73).

[97] Teun Vissers, Adam Wysocki, Martin Rex, Hartmut Lowen, C Patrick Royall, Arnout Imhof, and Alfons van Blaaderen. Lane formation in driven mixtures of oppositely charged colloids. *Soft Matter*, 7(6):2352–2356, 2011 (cit. on pp. 25 and 33).

[98] Christoph A. Weber, Christopher Bock, and Erwin Frey. Defect-mediated phase transitions in active soft matter. *Phys. Rev. Lett.*, 112:168301, Apr 2014 (cit. on p. 34).

[99] Ulrich Weidmann. Transporttechnik der fußgänger: transporttechnische eigenschaften des fußgängerverkehrs, literaturauswertung. *IVT Schriftenreihe*, 90, 1993 (cit. on pp. 9 and 10).

[100] Henricus H Wensink, Jörn Dunkel, Sebastian Heidenreich, Knut Drescher, Raymond E Goldstein, Hartmut Löwen, and Julia M Yeomans. Meso-scale turbulence in living fluids. *Proceedings of the National Academy of Sciences*, 109(36):14308–14313, 2012 (cit. on p. 73).

[101] Hugo Wioland, Francis G Woodhouse, Jörn Dunkel, John O Kessler, and Raymond E Goldstein. Confinement stabilizes a bacterial suspension into a spiral vortex. *Physical review letters*, 110(26):268102, 2013 (cit. on p. 73).

[102] Xingbo Yang and M Cristina Marchetti. Hydrodynamics of turning flocks. *Physical review letters*, 115(25):258101, 2015 (cit. on p. 82).

[103] Beibei Zhan, Dorothy N Monekosso, Paolo Remagnino, Sergio A Velastin, and Li-Qun Xu. Crowd analysis: a survey. *Machine Vision and Applications*, 19(5-6):345–357, 2008 (cit. on p. 64).

[104] Andreas Zöttl and Holger Stark. Emergent behavior in active colloids. *Journal of Physics: Condensed Matter*, 28(25):253001, 2016 (cit. on pp. 33 and 73).

[105] Iker Zuriguel, Alvaro Janda, Angel Garcimartín, Celia Lozano, Roberto Arévalo, and Diego Maza. Silo clogging reduction by the presence of an obstacle. *Physical review letters*, 107(27):278001, 2011 (cit. on p. 15).

Abstract

Modeling crowd motion is central to situations as diverse as risk prevention in mass events and visual effects rendering in the motion picture industry. The difficulty to perform quantitative measurements in model experiments, and the lack of reference experimental system, have however strongly limited our ability to model and control pedestrian flows. The aim of this thesis is to strenghten our understanding of human crowds, following two disctinct approaches.

First, we designed a numerical model to study the lane formation process among bidirectional flows of motile particles. We first evidenced the existence of two distinct phases: one fully laned and one homogeneously mixed, separated by a critical phase transition, unique to active systems. We then showed with a hydrodynamic approach that the mixed phase is algebraically correlated in the direction of the flow. We elucidated the origin of these strong correlations and proved that they were a universal feature of any system of oppositely moving particles, active of passive.

Second, we conducted a substantial experimental campaign to establish a model experiment of human crowds. For that purpose we performed systematic measurements on crowds composed of tens of thousands of road-race participants in start corrals, a geometrically simple setup. We established that speed information propagates through polarized crowds over system spanning scales, while orientational information is lost in a few seconds. Building on these observations, we laid out an hydrodynamic theory of polarized crowds and demonstrated its predictive power.

Résumé

Modéliser le mouvement des foules humaines est essentiel pour des situations aussi diverses que la prévention de risque dans les lieux publics, la planification d'évènements ou la création d'animations visuelles réalistes. Cependant, la difficulté de mener des expériences quantitatives limite notre compréhension de la dynamique des piétons, et le manque de mesures de référence rend impossible une comparaison poussée des modèles existants. Cette thèse tente d'augmenter notre compréhension des foules humaines par deux approches distinctes.

Dans un premier temps, nous avons conduit une étude numérique et théorique pour étudier formation de lignes au sein de flux bidirectionnels d'agents motiles. Nous avons montré qu'une transition de phase critique du second ordre séparait un état mélangé d'un état constitué de lignes géantes le long desquelles se déplacent les agents visants une même direction. Cette séparation est caractéristique des systèmes actifs. Une approche hydrodynamique nous a ensuite permis de prouver que les phases mélangées sont aussi algébriquement corrélées dans la direction longitudinale. Nous avons expliqué et montré que ces fortes correlations sont génériques de tous systèmes de flux bidirectionnels, qu'ils soient constitués de particules forcées ou de particules actives.

Dans un second temps, nous avons mené une campagne expérimentale de grande envergure afin d'établir une expérience de référence des foules humaines. Nous avons pour cela choisi un système modèle, la zone d'attente de marathons. Dans ces foules de dizaines de millers d'individus, nous avons quantitativement établi que les fluctuations de vitesse se propagent sur de grandes échelles, alors que les variations d'orientation s'évanouissent en quelques secondes. Grâce à ces mesures, nous avons construit une théorie prédictive hydrodynamique des foules polarisées.